Miniaturized Phase-Shifters for Ka-Band Phased Array Antennas

by

MohammadSadegh Faraji-Dana

A thesis
presented to the University of Waterloo
in fulfillment of the
thesis requirement for the degree of
Master of Applied Science
in
Electrical and Computer Engineering

Waterloo, Ontario, Canada, 2014

I hereby declare that I am the sole author of this thesis. This is a true copy of the thesis, including any required final revisions, as accepted by my examiners.

I understand that my thesis may be made electronically available to the public.

Abstract

Realizing robust and stable two-way links between the mobile users and the satellite is an extremely challenging RF/Microwave engineering problem. Low cost and low profile phased array is considered as the best solution for this problem. High performance low cost and miniaturized variable phase shifter is a key enabling technology for such complex smart phased array antenna system.

This thesis aims at the investigation of the existing solutions to realize miniaturized, low-cost and at the same time integrable phase shifters for commercial phased array antenna systems. Among few existing approaches, analog phase shifting devices based on voltage-tunable materials offers a promising solution.

Liquid Crystal (LC) and Barium Strontium Titanate (BST) are the two voltage tunable materials, which, beside their own primary applications, have found their way into Microwave and mm-Wave tunable device technologies. In this study the utilization of LC and BST in analog phase shifters has been rigorously investigated, the advantages and drawbacks of each when applied in different realizations have been discussed and further development and improvements in designs have been suggested. To achieve more compact designs for Ka-band phase shifters, a comprehensive design methodology for tunable filter-type phase shifter is proposed in this dissertation.

The most commonly used phase shifting architectures for the phased array antennas are RF, LO, IF and base-band phase shifting. It should be mentioned that LO, IF and base-band phase shifting are not suitable for phased arrays with large number of elements due to the formidable cost and complexity, particularly for Tx phased array systems which require one phase shifter per antenna element to meet the radiation mask. Therefore, this thesis is concentrated on RF (Microwave/mm-Wave) phase shifting, which is the most common for large phased array antenna systems.

Since one of the most important requirement in the design of Ka-Band phase shifters for phased array systems is the high level of miniaturization, dictated by antenna element spacing constraint, the thesis also addresses the highly compact structure of such phase shifters. In particular, a novel phase shifting concept based on very high dielectric constant materials has been explored. It is shown that by using this new concept, a highly miniaturized variable phase shifter with more than 360° phase tuning range is attainable.

Acknowledgments

First, I would like to thank God for all of his blessings.

I would like to express my sincere gratitude to my supervisor, Professor Safavi-Naeini for his continuous support, kindness, patience and profound knowledge. His constructive guidance helped me a lot during the research and writing of this thesis.

I wish to express my deepest and warmest gratitude to my family, my parents and sister, who have encouraged me in all the stages of my life. Their existence has been the sole motivation and incentive to rise and continue after each failure.

I am really thankful to my seminar committee members, Professor H. Majedi and Professor R. Mansour.

Last but not least, my greatest appreciation goes to all of my friends particularly Mr. Semnani and Mr. RayisZadeh. I learned a lot from them in this period.

Dedication

To my parents

Table of Contents

List of Tables viii

List of Figures ix

1 Introduction 1

1.1 Objectives 1

1.2 Motivations 5

1.3 Thesis Overview 7

2 Liquid Crystal (LC) Phase Shifters 8

2.1 Introduction 8

2.2 Basic Physics of Liquid Crystals for RF Applications 9

2.3 Literature Review of LC based phase shifters 12

2.3.1 IMSL Liquid Crystal Phase Shifters 12

2.3.2 Periodically Loaded Transmission Line 15

2.4 Liquid Crystal band-pass filter-type phase shifters 17

2.4.1 Dual mode ring resonator side-coupled filter 17

2.4.2 Analytical formulation and design methodology of band-pass filter-type LC based phase shifters 20

2.4.3 Analysis of the effect of different parameters on the maximum phase shift 29

3 BST Phase Shifters **35**
3.1 Introduction 35
3.2 Basic Physics of BST 36
3.3 Literature Review of BST based phase shifters 40
3.3.1 Periodically Loaded Transmission Line phase shifters 40
3.3.2 Tunable left-handed (LH) Transmission Line 48
3.4 Filter-type BST based phase shifters 50

4 High Dielectric Material Phase Shifters **54**
4.1 Introduction 54
4.2 Short literature review of HDC phase shifters 54
4.3 Proposed HDC phase shifters 56
4.3.1 Air, High Dielectric, Air-Gap, Metal phase shifter 56
4.3.2 High Dielectric loaded CPW line phase shifter 60

5 Concluding Remarks **68**
5.1 Summary 68
5.2 Future Works 69

APPENDICES **70**

A The effect of filter-type phase shifters on phased array performance **71**
A.1 Distortion due to the phase-frequency non-linearity of filter-type phase shifters 75

References **77**

List of Tables

2.1 Commercially available liquid crystals and/or optimized LC mixture at 30 GHz and 25 C° 12

2.2 Measured and Simulated characteristics of realized phase shifter at 34.32 GHz 18

2.3 Dimension of the parameters shown in Figure 2.12 21

3.1 Design Parameters of the phase shifter shown in Figure 3.10 47

4.1 The parameters for the phase shifter shown in Figure 4.7 61

4.2 Summary of Measurments at 30 GHz 67

A.1 Maximum gain variation over the frequency for Chebyshev, Elliptical, and All-Pass phase shifters for various beam scanning angles 76

List of Figures

1.1 An array of antenna elements 2

1.2 Simplified block-diagram for a phased array antenna 4

2.1 Mesophase behavior of LC molecules with temperature 9

2.2 An inverted microstrip line a)$\varepsilon_{r\perp}$ b) $\varepsilon_{r\parallel}$ 10

2.3 Typical continuous tuning of ε_r and $\tan\delta$ versus bias voltage 11

2.4 Performance diagram for various LC mixtures 13

2.5 Phase shift versus DC voltage at 20GHz 13

2.6 Cross section of CPW line segment (left) and loaded capacitor (right) . . . 15

2.7 Top view of the structure 15

2.8 Extracted differential phase shift 16

2.9 Dual Mode ring resonator side-coupled via open-circuited quarter wavelength lines 17

2.10 Layout of the designed ring resonator phase shifter 18

2.11 Simulated S-parameters of the designed ring resonator phase shifter shown in Figure 2.10 19

2.12 Schematic of the tunable structure in which liquid crystal is utilized 20

2.13 Filter pass-bands for the lowest, middle, and highest center frequencies . . 23

2.14 Block diagram of the iterative method for achieving 360° phase shift 24

2.15 S parameters of the sample Chebyshev 2GHz 5 poles filter with 10dB return loss and $f_0 = 29.75$ GHz (a) magnitude (b) phase response 25

2.16 (a) magnitude of S_{21}, (b) magnitude of S_{11}, and (c) phase response S_{21} for the shifted filter at shifted center frequencies f_0,$f^{high}_{0\ shifted}$, $f^{low}_{0\ shifted}$ 27

2.17 Phase response of filters in shifted center frequencies f_0,$f^{high}_{0\ shifted}$, $f^{low}_{0\ shifted}$. 28

2.18 Maximum phase shift vs. the order of the Chebyshev filter 29

2.19 Maximum phase shift per wavelength vs. the order of the Chebyshev filter 30

2.20 Maximum Phase-Shift for different order of Chebyshev filters (N) vs. bandwidth when no restriction exists on tunability 30

2.21 Maximum Phase-Shift for different order of Chebyshev filters vs. bandwidth by applying the restriction on the maximum tunability 31

2.22 Maximum Phase-Shift for different order of Chebyshev filters vs. Q_u 32

2.23 Maximum phase shift vs. Q_u for different values of bandwidth 33

2.24 Maximum phase shift vs return loss for different order of filter 34

3.1 Unit cell of barium titanate in its para-electric phase (left) ferroelectric phase (right) 37

3.2 Hysteresis loop for BST thin film 38

3.3 The structure of ferroelectric microstrip phase shifter 38

3.4 Capacitor Voltage characteristics measured at 22GHz 40

3.5 Equivalent circuit of a loaded transmission line unit cell 41

3.6 a) The maximum phase shift vs loading factor b) frequency variation of $\Delta\Phi_{max}$ when $x = 1.4$ 43

3.7 Layout of the fabricated phase shifter 44

3.8 Layout of periodically loaded transmission line phase shifter consisting of 8 unit cells 45

3.9 The magnitude of S_{21} as a function of frequency 46

3.10 Simulated phases shifter in HFSS with dimensions 47

3.11 a) Phase of the structure (degree) vs dielectric constant of BST material b) S parameters of the simulated structure in the frequency range of $29 - 30.5$ GHz for $\varepsilon_{r,BST} = 300$ 48

3.12 The equivalent circuit for Left-handed transmission line, basic (unbalanced) and balanced designs 50

3.13 Phase response of the designed 2nd order all-pass filter 52

4.1 Side view of the waveguide used as a phase shifter, loaded with an air-dielectric sandwich structure 55

4.2 a) Effective dielectric constant and b) the relative phase shift versus air gap for the air-dielectric sandwich structure for BLT $\varepsilon_r = 85$ 55

4.3 Proposed air, dielectric, air-gap, metal phase shifter 56

4.4 Norm of electric field for the simulated phase shifter structure in COMSOL software with $5\mu m$ air-gap 59

4.5 Modal analysis and simulation result of the propagation constant variation versus the air-gap size 59

4.6 Phase shift versus the air-gap size for the proposed phase shifter shown in Figure 4.3 60

4.7 The proposed high dielectric loaded CPW line phase shifter 61

4.8 Integration path in the complex α plane 64

4.9 The mapping which has been performed for region II 65

4.10 Propagation Constant versus h_3 calculated using the two methods at 30 GHz 66

4.11 Maximum phase shift versus the dielectric constant at 30GHz, for the phase shifter shown in Figure 4.7 67

A.1 a) Quantized current coefficients of antenna elements, b) gain radiation pattern of Tx planar array 72

A.2 Gain radiation patterns of the Tx phased array for beam position 30° . . . 72

A.3 The phase shifts of the three types of phase shifters versus frequency, a) Chebyshev, b) Elliptical c) All-Pass filter 73

A.4 Gain radiation pattern at $f = 29.5$, 29.75, and 30GHz for a) Chebyshev b) Elliptical C) All-Pass phase shifter when the scanning angle is 30° 74

A.5 Beam positioning error at f= 29.5, 29.75, and 30 GHz for the case of Elliptical phase shifter when the scanning angle is 30° 75

A.6 Maximum Gain versus frequency for beam scanning angles of 10°, 20°, and 30° when using a) Chebyshev, b) Elliptical, and c) All-Pass phase shifters . 76

Chapter 1

Introduction

1.1 Objectives

An antenna array is defined as an ensemble of *identical* antenna elements with the *same orientation* in space excited by a well-designed feed circuit (amplitude and phase) containing active and/or passive elements [1]. Figure 1.1 shows a schematic for an array of antenna elements.

The excitation coefficient for each antenna element is $I_m = |I_m|e^{j\phi_m}$.

According to antenna theory, the far-field radiated electric field for each of the antenna elements located at the *origin*, is represented as:

$$\mathbf{E}_{m,at\ origin}(\theta,\phi) = jk\eta I_{in}\vec{l}_e(\theta,\phi)\frac{e^{-jkr}}{4\pi r}, \qquad m = 1, 2, \ldots, N \tag{1.1}$$

where $\vec{l}_e(\theta,\phi)$ is the vector effective length of the antenna element. When the antenna element $\#m$ is moved by the vector $\vec{r}_m$ to the *new position* (where $|\vec{r}_m| << |\vec{r}|$) the far-field radiated electric field, using paraxial approximation is derived as:

$$\mathbf{E}_m(\theta,\phi) = jk\eta I_{in}\vec{l}_e(\theta,\phi)\frac{e^{-jkr}}{4\pi r}e^{jk\vec{r}_m.\hat{r}} = \mathbf{E}_{e,at\ origin}(\theta,\phi)e^{jk\vec{r}_m.\hat{r}}, \qquad m = 1, 2, \ldots, N \tag{1.2}$$

where $\hat{r} = \sin\theta\ \cos\phi\ \hat{x} + \sin\theta\ \sin\phi\ \hat{y} + \cos\theta\ \hat{z}$ in "Cartesian coordinate system".

Using equation (1.2), the total far-field radiated electric field for an array of elements

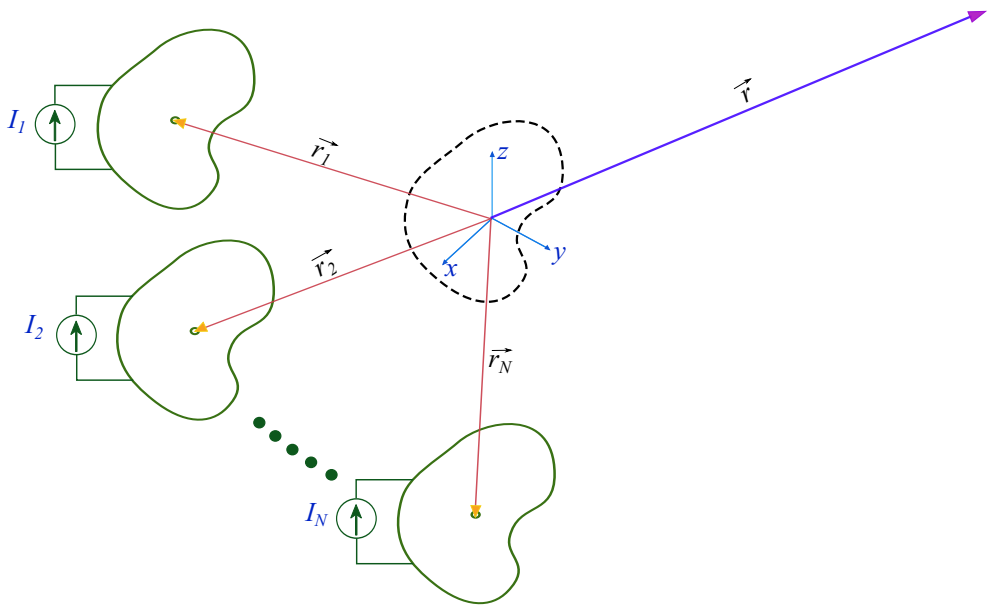

Figure 1.1: An array of antenna elements

is calculated as:

$$\mathbf{E}(\vec{r}) = \sum_{m=1}^{N} \mathbf{E}_m = \underbrace{\mathbf{E}_e(\vec{r})\,|_{I_{in}=1}}_{Element\ Factor} \underbrace{\sum_{m=1}^{N} I_m e^{jk\vec{r}_m.\hat{r}}}_{Array\ Factor} \tag{1.3}$$

As it is observed in equation (1.3), the total far-field radiated electric filed of an array is decomposed to an element factor $\vec{E}_e(\vec{r})\,|_{I_{in}=1}$ multiplied by an array factor ($\sum I_m e^{jk\vec{r}_m.\hat{r}}$); in other words, the array factor plays the role of a spatial filter for the element factor.

For a planar antenna array consisting of N elements located in $x-y$ plane, equation (1.3) is written as:

$$\mathbf{E}(\vec{r}) = \mathbf{E}_e(\vec{r})\,|_{I_{in}=1} \sum_{m=1}^{N} |I_m| e^{jk(x_i\ \sin\theta\ \cos\phi + y_i\ \sin\theta\ \sin\phi) + j\phi_i} \tag{1.4}$$

where $\vec{r_i} = x_i\hat{x} + y_i\hat{y}$ are the element positions on $x-y$ plane.

For creating the maximum radiated electric field at an arbitrary θ_0, ϕ_0 direction in space, the phase of each antenna element should be adjusted in such a way that

$$k(x_i \ \sin\theta_0 \ \cos\phi_0 + y_i \ \sin\theta_0 \ \sin\phi_0) + \phi_i = 2n\pi \qquad n = 0, \pm 1, \pm 2, \ldots \tag{1.5}$$

Antenna arrays which have the capability of tuning the phase of the elements (ϕ_i) so that the radiation pattern is reinforced in a particular direction and suppressed in undesired directions [2] are called "Phased Array Antennas". It should be mentioned that $|I_m|$s will determine the *radiation pattern*, *side-lobes* and the *maximum gain* of the array when all of the elements have the same input phase.

Rapid tuning of the input phase of antenna elements results in a fast electronic main beam scanning compared to the old mechanical scanning, which usually takes much more time. Phased array antennas by having a planar low profile and low weight structure have a high priority with respect to the traditional parabolic dish antennas for *satellite communications*. These unique characteristics have brought about many applications for phased array antennas.

Radar systems were initially the first application that phased array antennas found their way in. Traditionally, phased array antennas were used for military applications. [3]. Beyond that, phased array antennas have been used for radio astronomy applications. Another *important* application of phased array can be in automobile industry for automotive collision avoidance or adaptive cruise control systems [4, 5, 6]. The importance of this application is clear when considering that every minute someone loses his/her life due to a car accident [7]. Utilizing the phased array technology in emerging 60GHz wireless technology [8] will result in an increased data rate and improvement of channel capacity with more efficient power consumption [9, 10, 11, 12]. Phased array are highly used to extend the coverage in a particular area by enhancing the desired signal and diminishing the unwanted interferences. Satellite TV is an example for this kind of application. In addition, emerging biomedical applications such as cancer detection in early stages can also benefit from the phased array technology [13, 14, 15].

Despite the wide range of applications for phased array antenna systems, this technology has not been prevalent in the commercial arena yet. The total cost of phased array antenna is currently the main obstacle for exploiting them in large-scale commercial applications. The main cost of phased array antenna systems is attributed to the cost of their phase shifters, this cost sometimes reach to half of the total cost of the phased array system. Some efforts have been made to minimize the total cost of phased array system by reducing the number of phase shifters, or categorizing the antenna elements into a number of sub-arrays, each using a single phase shifter [16]. However, these approaches lead to unwanted side

lobes, or grating lobes, which limit the system performance[17]. The other impediments that restricted the phased array technology in military and aerospace fields is their size, weight, power consumption and overall complexity. By addressing these issues and reducing the cost, it is expected to observe the ubiquitous employment of phased arrays in the commercial industry [2].

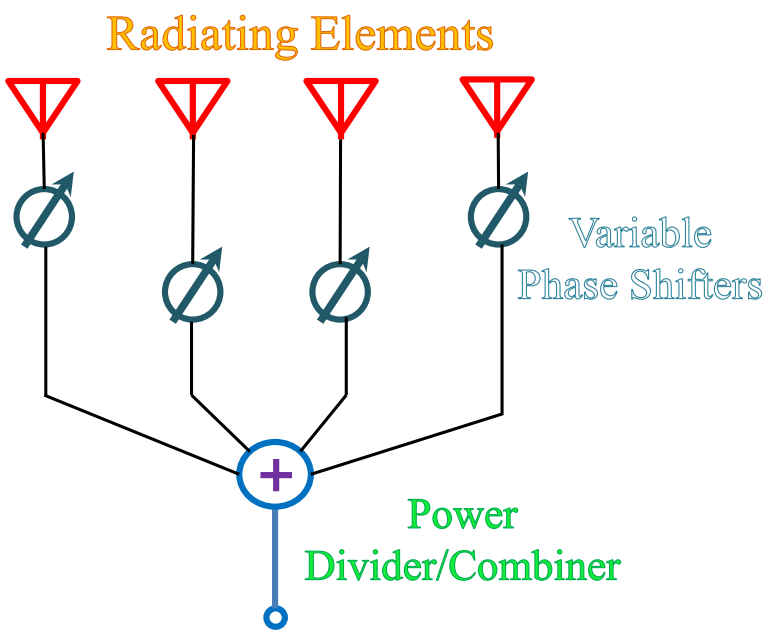

Figure 1.2: Simplified block-diagram for a phased array antenna

After this short introduction, it should be mentioned that in this thesis our main focus is on two-way commercial Ka-band phased array antennas for satellite communications, which can be installed on the roof of a car, bus or train without the need to make any fundamental change in the structure of the vehicle. This kind of phased array antenna, to be utilized in satellite communications, should be directive enough, requiring about 5000 elements in the transmitter or receiver sides.

One of the important challenges involved in two-way Ka-band phased array systems is to meet the radiation mask requirements (no grating lobes) forced by the satellite communication standards in the transmitting mode of land-mobile terminals. The *antenna element spacing* in the transmitter phased array system should be a fraction of wavelength

to avoid the grating lobes; that is the reason why the phase shifters applied in the transmitting phased array should be as miniaturized as possible. In the receiving mode there is no need to meet the radiation mask and grating lobes are tolerated in the reception radiation pattern; therefore, there is not usually a strict limitation on antenna element spacing in the receiving mode.

1.2 Motivations

Phase shifters are the key components for phased array antennas, specially for millimeter applications. As stated in the previous section, our goal in this thesis is to investigate the challenges involved in the design of phase shifters for a two-way commercial Ka-band phased array antenna system. The challenges are different in the reception or transmission array. As an example in the receiving array, there is not usually a severe constraint on the *size* of phase shifters, since there is a wider antenna element spacing or maybe a single phase shifter can be used for a sub-array of antenna elements. In this thesis, our main focus is on the transmitter side of the Ka-band phased array system which operates in the frequency range of $29.5 - 30$ GHz (BW=500 MHz). The other constraints that should be taken into account in our analysis are:

- Insertion loss and its variation
- Input matching impedance
- Phase shifting resolution
- Switching response time
- Bandwidth (BW)
- Cost
- Packaging and Integration
- Maximum possible phase shift
- Linearity and Phase error

Generally, there are two types of phase shifters, namely *Digital* and *Analog* phase shifters. Due to the quantization errors of Digital phase shifters, it may not be possible to obtain sufficient phased array beam pointing resolution. Hence, for extra-fine beam steering, analog phase shifters are preferred because, in principle, they can provide infinite resolution.

Among the above-mentioned constraints our focus will be on an *analog*, *low cost*, *miniaturized* phase shifter to be *integrable* with a Ka-band phased array structure. It is desirable to have a phase shifter with small insertion loss (good input matching); however, more important than that, is preserving a constant insertion loss (and input impedance) over the phase shifting range; otherwise variable gain amplifiers (VGAs) are required to maintain the signal amplitude level. The required phase shifter should possess an acceptable response time for satellite communications and be as linear as possible. The phase error in its entire bandwidth should be negligible as well.

In general, ferrites are widely used in lower frequency phase shifting [18, 19, 20, 21]. However, their usage in higher frequencies are limited due to being bulky (not planar) and their cost and complexity. Ferrite phase shifters are also slow to respond and cannot be used for applications where rapid beam scanning is required. Semiconductor devices are the other choice which are much faster; however, they have high losses and limited power-handling capability. The other option for phase shifting in this range of frequency is Micro-Electro-Mechanical Systems(MEMS). RF MEMS phase shifters are often based on MEMS switches and classified in the category of digital phases shifters; moreover they are usually complex, expensive for commercial applications and their integration (packaging) with phased array structure is difficult and problematic [22], so this class of phase shifters will not be investigated in this thesis as well.

Liquid Crystals (LC) and ferroelectric materials, particularly Barium Strontium Titanates $Ba_xSr_{1-x}TiO_3$ (BSTs), are voltage tunable materials that their dielectric constants are varying by the change in the applied voltage. This class of tunable material based phase shifters are also an effective solution in the realization of phase shifters in Ka frequency band.

Due to our limitation in the size of phase shifter for Ka-band phased array antenna, high dielectric materials with small loss (high quality factor) in Microwave and mm-Wave frequency such as BLT ceramics are another feasible solution[23].

1.3 Thesis Overview

Following this section, Chapter 2 will be begun by an introduction to the physics of liquid crystal (LC) materials. Through the literature review, liquid crystal based phase shifters proposed by others will be presented. The band-pass filter-type phase shifters based on liquid crystal materials and their design strategy will be discussed afterwords. Analyzing the effect of bandwidth, quality factor, the order of the filter and tunability of liquid crystal material on the maximum phase shift will conclude this chapter.

Chapter 3 will be started by an introduction to different kinds of ferroelectric materials and their characteristics. A short summary of BST based phase shifters in the literature illustrates the pros and cons of ferroelectric materials, particularly BST, with respect to liquid crystals. A phase shifter structure based on BST parameters will be presented and corresponding simulation results will be demonstrated in this chapter as well. The modelling of All-pass filter type phase shifters using BST and their ability to achieve more than 360° phase shift is the final topic of this chapter.

High dielectric materials and their characteristics will be introduced in Chapter 4. Utilizing high dielectric materials, two phase shifting schemes will be presented. Analytic formulation followed by the simulation and measurement results will justify and confirm the validity of the proposed structures (designs).

The summary of the thesis, conclusion and future research will be also discussed in Chapter 5. An investigation of the nonlinear effect of phase frequency response in filter-type phase shifters on the performance of the phased array antenna system is explained in Appendix A.

Chapter 2

Liquid Crystal (LC) Phase Shifters

2.1 Introduction

In this chapter, a study of Liquid Crystal (LC) phase shifters and their applications in Ka frequency band will be carried out. First, basic physics of Liquid Crystal materials and their properties and characteristics which make them one of the solutions in realizing Ka-band phase shifters are reviewed. After, a survey on different ideas for the realization of liquid crystal phase shifters will be done. Finally, the general basis and the pros and cons of each idea will be explored and the realization of 360° LC filter-type phase shifters will be discussed in more detail using an iterative design method and HFSS simulations.

The shortage in available frequency spectrum for wireless communications and the requirement for more functionality in smaller volumes has increased the demand for reconfigurable components. LC based devices are considered one of the main categories of these reconfigurable components. High and continuous tunability, low/moderate dielectric loss, high linearity and cost efficiency are advantages of LCs which make it a promising tunable material for microwave and mm-Wave applications [24]. However, they often suffer from limited thermal (temperature) stability [25]. LCs will be the key elements for future reconfigurable RF devices; especially optimized LC mixtures which offer high performance at microwave frequencies with low loss tangent. The use of LC-filled waveguides to realize variable and electrical command-control phase shifters has highlighted the potentiality of these materials for tunable applications.

2.2 Basic Physics of Liquid Crystals for RF Applications

Liquid Crystals are classified as three main types: Thermotropics, Polymerics and Lyotropics. Thermotropics LCs exhibit a mesophase behavior between the solid crystalline and isotropic liquid phase [26], as depicted in Figure 2.1. Based on the degree of orientational

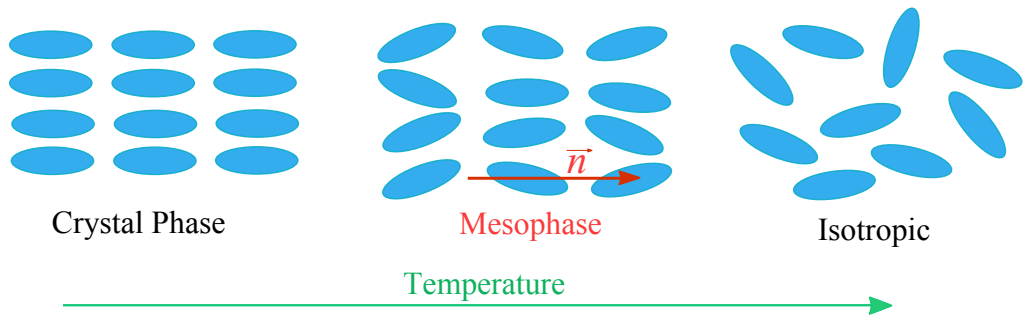

Figure 2.1: Mesophase behavior of LC molecules with temperature

or positional order, the mesophases can be classifeid as [27]:

- Nematic
- Cholesteric
- Smectic (A,B or C order)

The typical LC molecule in nematic phase has a rod-like shape as shown in Figure 2.1. The length of the molecules are typically few nanometers. In a Nematic LC there is a long range orientational order of anisotropic molecules. This anisotropy in shape causes anisotropy in terms of the dielectric constant. Measurements of the frequency dependence of this anisotropy usually show two relaxation frequencies below 400 MHz, which can be assigned to rotations along the long and short axis of the molecules. Above 400 MHz no relaxation appears in the investigated frequency range, implying the usability in microwave frequency. These anisotropic LC molecules can be oriented by means of an electrostatic or magneto-static field.

Inverted Micro-Strip Line (IMSL) configuration is commonly used in LC based structures for tuning. In order to understand the concept of LC's tunability, a cross section of an LC IMSL is shown in Figure 2.2.

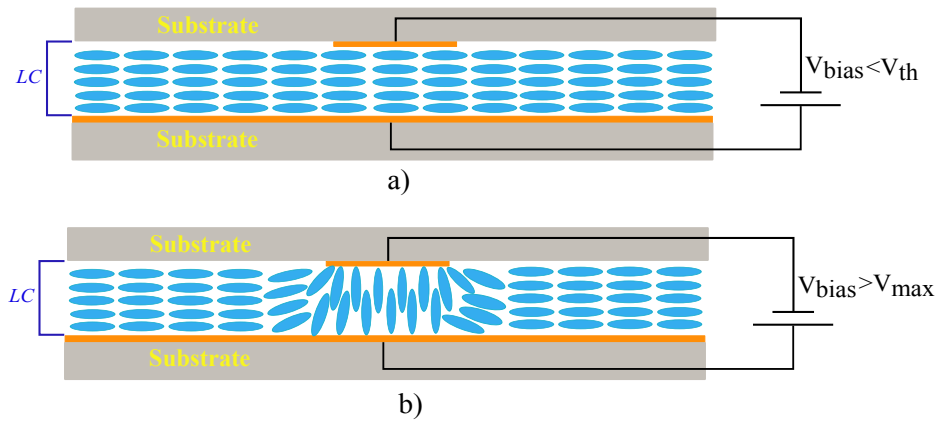

Figure 2.2: An inverted microstrip line a)$\varepsilon_{r\perp}$ b) $\varepsilon_{r\|}$

In this structure the microstrip line and ground electrodes are located on the top and bottom substrates, respectively. LC fills the space between the two substrates which forms the dielectric of IMSL. Since the material is liquid, the molecules feature only a weak molecular adhesion and thus their orientation in the bulk can be changed. Owing to the rod-like shape, the molecules in a bulk tend to orient themselves in parallel order. In LCs the direction of the long axis of the molecules is defined by the vector $\vec{n}$. The surface of LCs are coated by a thin polyamide film which is an a alignment layer that orients the LC molecules in parallel to the surface initially. In this case, the relative permittivity and loss tangent are denoted by $\varepsilon_{r\perp}$ and $\tan\delta_\perp$. Molecules will keep their orientation until the applied bias voltage is smaller than the threshold voltage V_{th} (Figure 2.2a). If the applied voltage exceeds V_{max}, all molecules are aligned parallel to this bias electric field (Figure 2.2b) and $\varepsilon_{r\|}$ and $\tan\delta_\|$ are effective.

By adjusting the strength of the bias field, all states in between are feasible and therefore continuous tuning of the effective permittivity of the substrate is possible (Analog phase shifter). Most of the LCs have the positive anisotropy, i.e. $\Delta\epsilon_r = \epsilon_{r\|} - \epsilon_{r\perp} > 0$ and so the relationship $\tan\delta_\perp > \tan\delta_\|$ is also true. Figure 2.3 shows continuous tuning of dielectric permittivity and loss tangent versus bias voltage for a typical LC layer.

The relative tunability τ is defined as the ratio of the tuning range of the permittivity to the maximum permittivity:

$$\tau = \frac{\varepsilon_{r\|} - \varepsilon_{r\perp}}{\varepsilon_{r\|}} \tag{2.1}$$

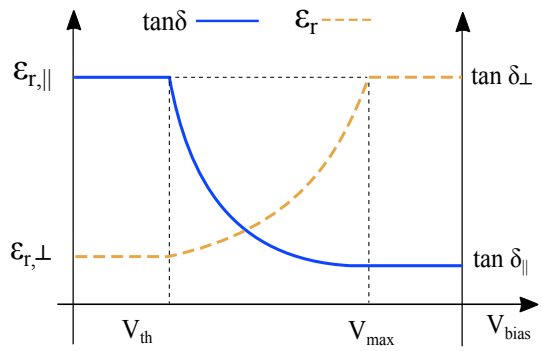

Figure 2.3: Typical continuous tuning of ε_r and $\tan\delta$ versus bias voltage [28].

The permeability is approximately non-varying ($\mu_r \approx 1$) [29]. Due to the anchoring of molecules at the surfaces (polymide film), when the voltage is released again, the LC molecules orient back to their initial states. The switching times for this mechanism are defined as follows [30]:

- switch-on time (τ_{on}), defined by the delay time from 10% to 90% for a rising tuning voltage.

$$\tau_{on} \propto \frac{\gamma^* h^2}{K_{eff}} \cdot \frac{1}{(\frac{U_0}{U_{th}})^2} \tag{2.2}$$

- switch-off time (τ_{off}),defined by the delay time from 90% to 10% when the voltage drops to zero.

$$\tau_{off} \propto \frac{\gamma^* h^2}{K_{eff}} \cdot \frac{1}{\pi^2} \tag{2.3}$$

Where γ^* is the effective rotational viscosity, K_{eff} is the effective elastic constant, h is the height of the LC layer, and U_0 and U_{th} are the tuning voltage and the threshold voltage, respectively. As observed in equations (2.2), (2.3) both switching times have a quadratic dependency on the height of the LC layer(h).

It is important to define the figure of merits for phase shifters. The figure of merits for phase shifters is defined as the maximum phase shift per $1dB$ insertion loss of phase shifter

in its operation frequency band.

$$FoM = \eta_{PS} = \frac{Max(\Delta\phi)}{Insertion\ Loss(dB)} \tag{2.4}$$

Some of the commercially available LCs and/or optimized LC mixture for microwave and mm-Wave application is listed in Table 2.1.

Table 2.1: Commercially available liquid crystals and/or optimized LC mixture at 30 GHz and 25 C°

Material	$\varepsilon_{r\perp}$	$\varepsilon_{r\parallel}$	$\tan\delta_{\perp}$	$\tan\delta_{\parallel}$
K15	2.55	2.84	0.03	0.01
E7	2.52	2.96	0.026	0.0094
BL006	2.62	3.04	0.025	0.011
BMW10 mixture	2.49	3.18	0.017	0.004

The method which is usually used to measure the parameter for LC materials is cavity perturbation theory [31]. Recently, various generations of LC mixtures have been characterized with high anisotropy and low loss tangent. The progress of these new mixtures against conventional mixtures, both in terms of tunability (increased) and $\tan\delta$ (decreased), is clearly seen in Figure 2.4.

2.3 Literature Review of LC based phase shifters

Tunable phase shifters may be built with high differential phase shift and low insertion loss [33]; however, the major problem of these structures is that they suffer from slow tuning time [33]. This problem can be overcome by using new material technologies [34]. Some of the structures used in the literature using LC for phase shifting will be discussed in the following section:

2.3.1 IMSL Liquid Crystal Phase Shifters

Figure 2.2 shows the IMSL structure filled with liquid crystal. In these structures, by changing the permittivity of LC (from $\varepsilon_{r\parallel}$ to $\varepsilon_{r\perp}$) in a finite length the propagation constant changes accordingly and a phase difference is created. Such structures are not usually able

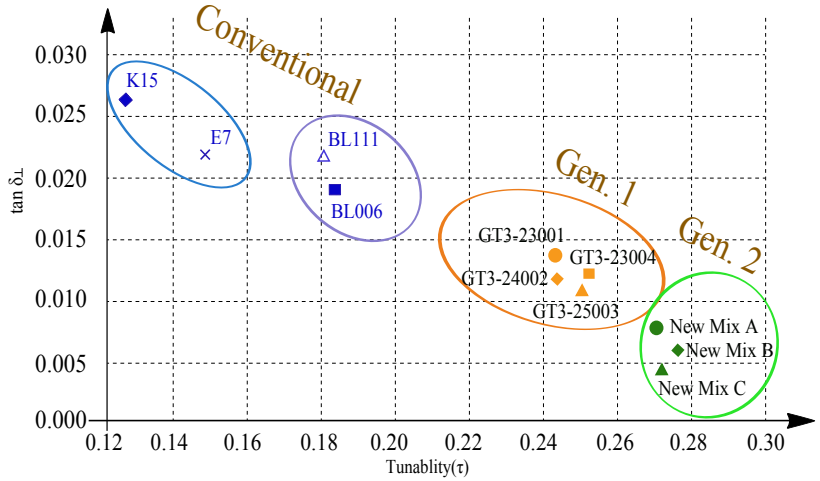

Figure 2.4: Performance diagram for various LC mixtures [32]

to create large phase shifts in a compact size. The differential phase shift behavior vs DC bias voltage for an inverted microstrip line phase shifter is presented in Figure 2.5 [35]. As it can be observed, there is threshold voltage (2V) for rising the differential phase shift and most of the variations occur between $2 - 6$V.

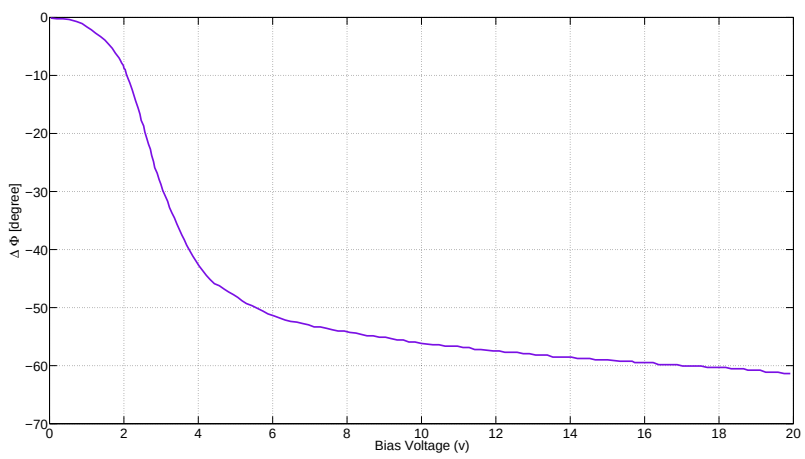

Figure 2.5: Phase shift versus DC voltage at 20GHz [35]

In IMSLs the differential phase shift can be written as [36]:

$$\Delta\phi = \frac{2\pi \cdot f \cdot \ell}{c_0} \cdot \Delta n_{eff} \tag{2.5}$$

$$\Delta n_{eff} = \sqrt{\varepsilon_{r\parallel}} - \sqrt{\varepsilon_{r\perp}}$$

Therefore

$$\Delta n_{eff} = \frac{\Delta\phi \cdot c_0}{2\pi \cdot f \cdot \ell} \tag{2.6}$$

One can also estimate the maximum available FoM of a simple IMSL as follows:

$$\alpha = Im\{\gamma\} = Im\{\frac{\omega}{c_0} \cdot \sqrt{\varepsilon_r}\sqrt{1 - j \cdot \tan\delta}\} \tag{2.7}$$

$$= \frac{\omega}{c_0} \cdot \sqrt{\varepsilon_r}\sqrt{1 + \tan^2\delta}.\sin(\frac{\tan\delta}{2}) \tag{2.8}$$

For $\tan\delta \ll 1$, the attenuation becomes

$$\alpha = Im\{\gamma\} = \frac{\omega}{c_0}.\sqrt{\varepsilon_r}\frac{\tan\delta}{2} \tag{2.9}$$

Therefore, by using equations (2.4),(2.5) and (2.9), the FoM is given by

$$FoM = \frac{\Delta\phi}{|S_{21}|} = \frac{\Delta\phi}{|20 \cdot loge^{-\alpha\ell}|} \tag{2.10}$$

$$= \frac{\Delta\phi}{8.686.\alpha\ell} = \frac{2\pi\sqrt{\varepsilon_{r\parallel}} - \sqrt{\varepsilon_{r\perp}}}{8.686 \cdot \pi\sqrt{\varepsilon_{r\parallel}}\ \tan\delta}\ [rad/dB] \tag{2.11}$$

In [36], two IMSL LC phase shifters at 20GHz have been reported; one filled with K15 with the length of $48mm$ (70° differential phase shift) and the other one filled with a novel mixture with higher tunability and the length of $50mm$ (more than 3 wavelength) with almost 250° phase shift. Generally, the achieved FoM value of phase shifters is smaller than what is calculated based on equation (2.11). The FoM-value for phase shifters in [36] is 75% and 65% respectively. This reduction is mainly due to partial pre-orientation of LC molecules by polymide film and/or the copper loss.

2.3.2 Periodically Loaded Transmission Line

LC phase shifters based on periodically loaded transmission line have been presented in [37] for operating at 20 GHz which have two sections, non-tunable and tunable; corresponding respectively to the periodic structure by a CPW line and an LC filled parallel plate capacitor. The structure consists of elements which are made up of transmission line with a certain length $l/2 = 0.561$mm and characteristic impedance of $Z_0 = 50\Omega$, a tunable load capacitor C_x and another $l/2$ line segment (Figure 2.6).

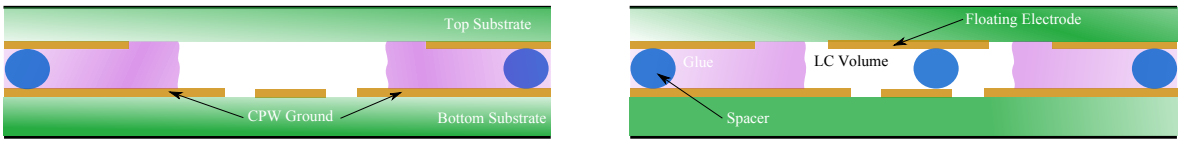

Figure 2.6: Cross section of CPW line segment (left) and loaded capacitor (right) [37]

The two substrates are made of fused silica ($\varepsilon_r = 3.8$, $\tan\delta = 10^{-4}$, thickness$= 300\mu m$.). The cross section of the CPW line segment and load capacitor is depicted in Figure 2.6. The bias voltage to orient the LC molecules is applied to the top floating electrode. The top view of the structure is shown in Figure 2.7. The total length of the phase shifter is $12.7mm$. The switching speed for this phase shifter is $\tau_{on} = 100ms$, $\tau_{off} = 340ms$ and the applied bias voltage varies from $0 - 40V$. Since the LC layer is negligibly thin, the propagation constant of the structure is mostly determined by fused silica substrates.

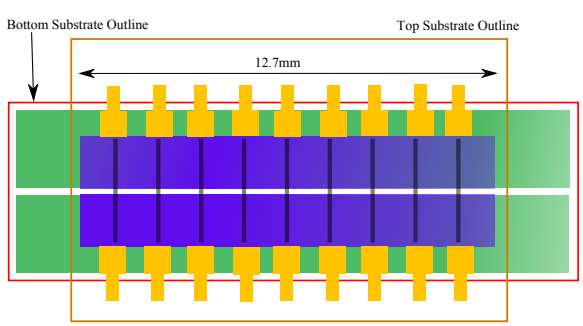

Figure 2.7: Top view of the structure [37]

The differential phase shift for this typical periodically loaded transmission line phase shifter is shown in Figure 2.8. The figure of merit $\eta_{PS} = 60°/dB$ has been reached in this kind of phase shifter.

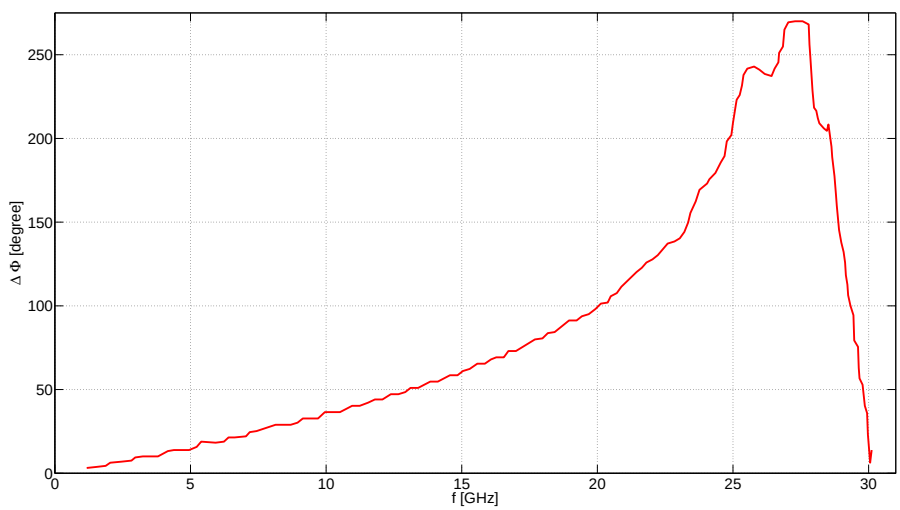

Figure 2.8: Extracted differential phase shift [37]

The periodic loaded phase shifter in [37] offers above 90° phase shift at 20 GHz. However, the estimated total length of the transmission line for creating 360° will be approximated as $50mm$ (more than three time of the wavelength at this frequency); therefore, this kind of LC based structures for phase shifting is not appropriate for our phased array, where the spacing between elements should be a fraction of wavelength.

Of the main advantage of LCs to other tunable materials is their low-loss behavior in microwave and mm-wave range of frequency. The insertion loss of the LC based phase shifters are not necessarily limited by the material loss of LC. Their insertion loss variations (the main problems in BST type phase shifters) is usually small and negligible. One of the disadvantages of LCs compared to the other tunable materials such as ferroelectric is the low dielectric constant and the small tunability. In most cases, LCs are used in RF structures along with other materials as the main substrate; thus, the tunability of the effective dielectric constant $\epsilon_{r,eff}$ of the structure will become even smaller. This means that in order to achieve 360° phase shift (using the structure presented in parts 2.3.1, 2.3.2) the length of the phase shifter should increase to multiple wavelengths. This increase in the length of the phase shifter results in the inability to fit the phase shifter in a fraction

of wavelength spacing between phased array antenna elements.

2.4 Liquid Crystal band-pass filter-type phase shifters

In section 2.3 it was deduced that the due to the small tunability of LC materials, the LC transmission line phase shifters are not capable of creating 360° in a small size package. Moreover, the phase shifting will happen not only in the frequency range that the phase shifter has been designed but also in the higher and lower frequency range.

In order to achieve first, a much higher phase shift in a more compact size and second, selectivity in the the frequency range, tunable (LC based) band-pass filter configurations will be presented as phase shifters in this section. If this kind of phase shifter is designed properly, the maximum phase shift will happen at the center frequency of the initially designed filter. The utilization of band-pass filters as phase shifters has been reported in [38, 39, 40, 41].

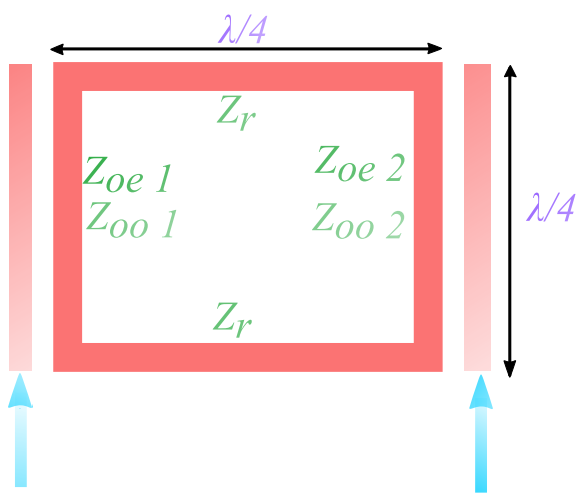

Figure 2.9: Dual Mode ring resonator side-coupled via open-circuited quarter wavelength lines [42]

2.4.1 Dual mode ring resonator side-coupled filter

An example of this kind of phase shifters has been designed based on a quarter-wavelength side-coupled dual-mode ring resonator using LC optimized mixture [43]. The design strat-

egy for this filter has been demonstrated in [42] (Figure 2.9).

In this filter configuration, owing to the odd and even impedance Z_{oe} and Z_{oo} of the parallel coupled microstrip, the dual mode operation of the ring resonator is excited. Thus, using one resonator, a compact phase shifter (in an area of $2 \times 2mm^2$) capable of creating approximately 120° at 35GHz is realized [43]. The phase shifter has been designed for $f_0 = 35$ GHz, $Z_r = 82\Omega$, $Z_{oe} = 132\Omega$, $Z_{oo} = 61\Omega$ and input and output of 50Ω. Table 2.2 shows the detailed results of simulation and measurement for this phase shifter [43].

Table 2.2: Measured and Simulated characteristics of realized phase shifter at 34.32 GHz

results	FoM_{av}	IL_{av}	IL_{max}	$\Delta\Phi$	ΔIL
measured	$30.6°/dB$	$3.82dB$	$4.03dB$	117.12°	$0.433dB$
simulated	$43.8°/dB$	$2.97dB$	$3.35dB$	130°	$0.67dB$

The compactness of this phase shifter is desirable since we need to utilize it in a large phased array with the constraint of minimum spacing between the the feed lines; however, in order to get 360° one needs to connect three of them in series which make the whole structure larger and not suitable for utilization in the phased array under consideration.

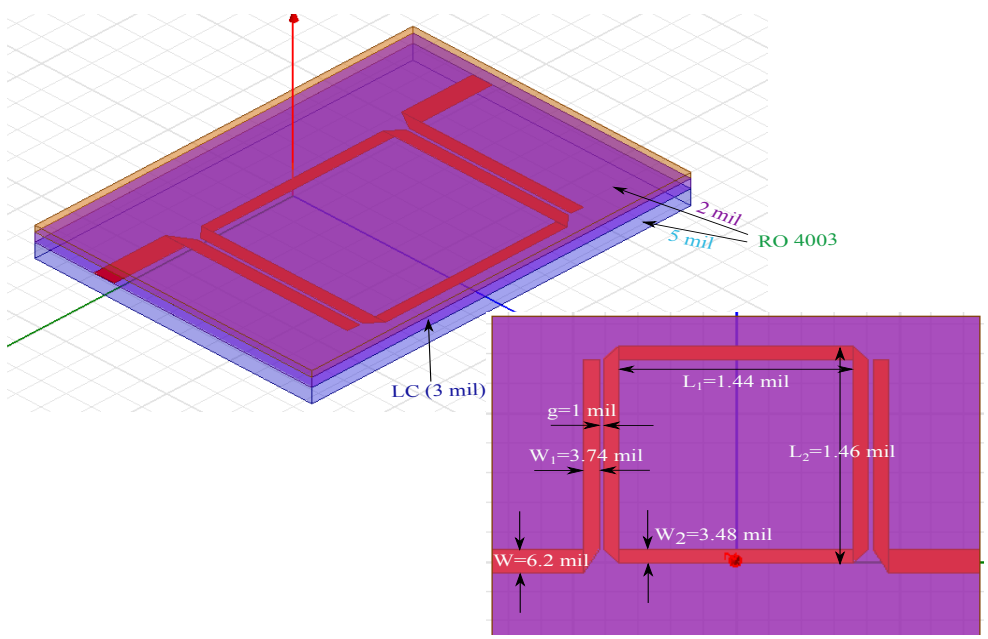

Figure 2.10: Layout of the designed ring resonator phase shifter

The other point that should be noted regarding this phase shifter is that the maximum phase shift in a moderate insertion loss is only reported for the single frequency, 34.32 GHz. Other frequencies in a small bandwidth around 34.32 GHz will not fall in the pass-band of the tuned filter and huge insertion loss in those frequencies will be observed. For most practical applications, especially satellite communications, the phase shifting process needs to be done in a range of frequencies as in our phased array (system bandwidth $= 29.5 - 30$ GHz) instead of a single center (or carrier) frequency.

In order to investigate the maximum phase shift of the ring resonator filter type phase shifter for our system bandwidth, simulations using Ansoft HFSS have been performed. The LC parameters for dielectric constant and $\tan\delta$ were extracted from [43]. The tuning range of LC (from 2.55 to 3) has been selected so that the system bandwidth (29.5−30 GHz) is always contained in all shifted pass-bands of the tuned filter. Layout of the designed phase shifter along with the dimensions and substrates which have been utilized for each layer of the strip line configuration are shown in Figure 2.10.

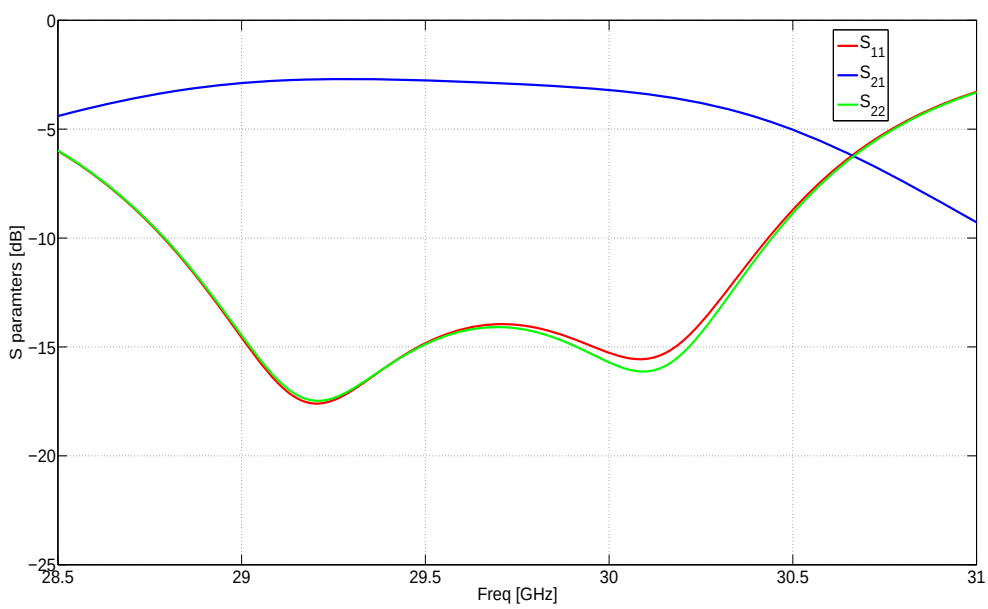

Figure 2.11: Simulated S-parameters of the designed ring resonator phase shifter shown in Figure 2.10

The maximum differential phase shift achieved using the configuration simulated and optimized depicted in Figure 2.10 is 90.4°. It is observed that in this case the maximum

tunability the of LC ($\epsilon_r = 2.4 - 3.2$) has not been utilized for the sake of providing the differential phase shift in the whole system bandwidth and not the single carrier frequency. That is why the maximum differential phase shift has been decreased to 90.4°.

The optimized scattering parameters for the structure shown in Figure 2.10 with the constraint of $S_{11} < -10$ dB are shown in Figure 2.11.

2.4.2 Analytical formulation and design methodology of band-pass filter-type LC based phase shifters

The phase shifting process basically depends on the particular design strategy used and the characteristics of the tuning mechanism applied in the Filter-Type phase shifters. In this section, a new and comprehensive methodology is proposed to determine the characteristics the filter needed to possess in order to achieve 360° differential phase shift assuming that the tuning mechanism is completely known. The methodology is general and can be applied to a wide range of filter-type response profiles and tuning devices, leading to an optimal design in terms of bandwidth and phase-frequency response linearity. The first step in the design of a filter-type phase shifter is modeling the tunable structure in which LC has been utilized. Here the same structure as used in Figure 2.10 has been applied . The schematic of the tunable structure analyzed in this section is presented in Figure 2.12.

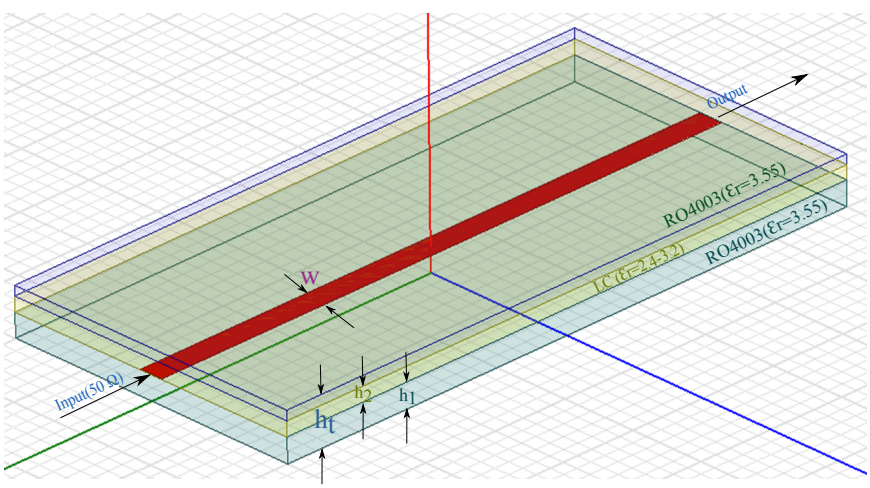

Figure 2.12: Schematic of the tunable structure in which liquid crystal is utilized

The dimensions of the parameters can be observed in Table 2.3.

Table 2.3: Dimension of the parameters shown in Figure 2.12

Dimensions	h_1	h_2	h_t	w
Value	5 mil	3 mil	10 mil	6.2 mil

By using HFSS simulations and Quasi-TEM approximation for the dominant mode of the configuration shown in Figure 2.12, the effective dielectric constants for maximum and minimum tunability of the LC are calculated as $\sqrt{\varepsilon_{r,eff\perp}} = 1.76$ and $\sqrt{\varepsilon_{r,eff\parallel}} = 1.855$. The average effective dielectric constant for which the filter design will be done is defined as: $\varepsilon_{r,eff\,av} = \sqrt{\varepsilon_{r,eff\perp}\varepsilon_{r,eff\parallel}} = 3.2648$. The other variables will be defined as follows:

$$x_{1,min} = \sqrt{\frac{\varepsilon_{r,eff\,av}}{\varepsilon_{r,eff\parallel}}} = 0.974$$
$$x_{2,max} = \sqrt{\frac{\varepsilon_{r,eff\,av}}{\varepsilon_{r,eff\perp}}} = 1.0267 \tag{2.12}$$

$x_{1,min}$ and $x_{2,max}$ are representations of the maximum possible variations in the center frequency of the designed filter (29.75 GHz for our case) by using the applied LC. Based on the definitions for $\varepsilon_{r,eff\,av}$ it is clearly observed that $x_{1,min} = \frac{1}{x_{2,max}}$.

$$x_{1,min} = \frac{f_{0,min}}{f_0}$$
$$x_{2,max} = \frac{f_{0,max}}{f_0} \tag{2.13}$$

where $f_{0,min}$ and $f_{0,max}$ are the center frequency of the tuned filter when $\varepsilon_{r_{LC}} = \varepsilon_{r\parallel} = 3.2$ and $\varepsilon_{r_{LC}} = \varepsilon_{r\perp} = 2.4$ respectively. The center frequencies of the tuned filters for the case $\varepsilon_{r_{LC}}$ is between 2.4 and 3.2 will be located between $f_{0,min}$ and $f_{0,max}$.

The second order ring resonator filter presented in Figure 2.10 was able to provides 90.4° differential phase shift. By increasing the order of the filter, more poles are added to the frequency response transfer function of the filter and the maximum differential phase shift is increased. Therefore the other important parameter for increasing the maximum phase shift will be the "*order of the filter*".

Different band-pass filters exhibit different frequency response (S parameters) behavior inside or out of their pass-band. Therefore in addition to order of the filter (number of

poles), the "*type of the filter*" (Maximally Flat, Chebyshev or Elliptical) plays a role in determining the maximum phase shift.

The effect of the loss in the filter due to the original structure or the loss occurring when the LC is tuned by the voltage should be brought into the consideration by defining the unloaded quality factor (Q_u) for the filter:

$$Q_u = \omega_0 \frac{W_T}{P_{loss}}, \qquad \frac{1}{Q_u} = \underbrace{\frac{1}{Q_c}}_{Copper} + \underbrace{\frac{1}{Q_d}}_{Dielectric}$$

$$Q_d = \omega_0 \frac{2W_e}{P_d} = \frac{\varepsilon'_{eff}}{\varepsilon''_{eff}} \tag{2.14}$$

For a $\ell = \lambda/2$ resonator strip line structure Q_u is calculated as:

$$Q_u = \frac{\pi}{2\alpha\ell} = \frac{\beta}{2\alpha}, \qquad \alpha = \alpha_c + \alpha_d \tag{2.15}$$

Although there are no accurate closed-form expression for α_c, α_d, they can be numerically calculated for each structure [44].

The other important criterion which determines the maximum allowable shift in the center frequency of the filter, and subsequently the maximum allowable phase shift of the filter-type phase shifter, is the "*filter band-width*" or the pass-band of the filter. The maximum center frequency shift should be adjusted in such a way that the system bandwidth ($29.5 - 30$ GHz) is contained in all shifted pass-bands; otherwise, the return loss will not be adequate for different phase shifting values. Therefore, it is essential that the minimum bandwidth of the filter should be greater than the system band-width (500 MHz in our case). Figure 2.13 illustrates the filter pass-bands for the lowest, middle, and highest center frequencies. Two band-edge frequencies of filters are calculated using the low-pass band-pass transformation [45]:

$$\frac{f_0}{BW}\left(\frac{f}{f_0} - \frac{f_0}{f}\right) = \pm 1 \rightarrow f^2 \mp B.W.\, f - {f_0}^2 = 0 \tag{2.16}$$

f_{high}^{filter} and f_{low}^{filter} are functions of the bandwidth of the filter ($f_{high}^{filter} - f_{low}^{filter} = BW$).

The f_{high}^{filter} is obtained using the $(+)$ sign equation and f_{low}^{filter} using the $(-)$ sign equation in equation (2.16). The maximum frequency shifts of the filter occur when the band-edge frequencies of two shifted pass-bands (f_{low}^{filter} and f_{high}^{filter}) approach the side frequencies of

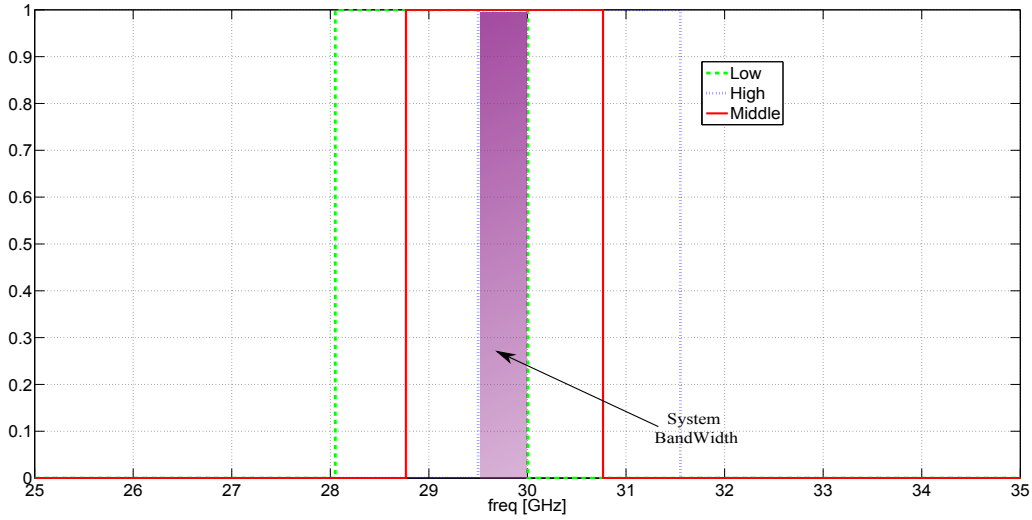

Figure 2.13: Filter pass-bands for the lowest, middle, and highest center frequencies

phased array system ($f_{low}^{system} = 29.5$ GHz and $f_{high}^{system} = 30$ GHz). Accordingly, the center frequencies of the shifted pass-bands, namely $f_{0\ shifted}^{high}$ and $f_{0\ shifted}^{low}$, are obtained as follows:

$$x_2 = \frac{f_{0\ shifted}^{high}}{f_0} = \frac{f_{low}^{system}}{f_{low}^{filter}}$$
$$x_1 = \frac{f_{0\ shifted}^{low}}{f_0} = \frac{f_{high}^{system}}{f_{high}^{filter}} \tag{2.17}$$

where f_0 is 29.75 GHz in our case. If $x_2 < x_{2,max}$ and $x_1 > x_{1,min}$ then the maximum phase shift of the designed filter is realizable by the LC. If $x_2 > x_{2,max}$ and $x_1 < x_{1,min}$, x_1 and x_2 should be restricted to $x_{1,min}$, $x_{2,max}$ which is the maximum tunability of the LC based structure. In summary, the maximum phase shift of a tunable band-pass filter is a function of the *order*, *band-width*, *insertion loss* (Q_u), *return loss* and the *type* of the filter. An iterative method can be used to determine the minimum order and the required bandwidth for different types of band-pass filter-type phase shifters knowing the Q_u for the structure and the desirable return loss. The block diagram of the iterative method for acquiring 360° phase shift is shown in Figure 2.14.

The phase response of the filter would be the phase of S_{21}. Depending on the type, return loss and the order of the filter, the coupling matrix $\mathbf{M}$ will be defined distinctively

[46]. The scattering parameters for an Nth order filter will be defined as [44]:

$$
\begin{aligned}
S_{21} &= -2i\sqrt{R_1\ R_N}[\lambda\mathbf{I} - i\mathbf{R} + \mathbf{M}]^{-1}_{N,1} \\
S_{11} &= 1 + 2iR_1[\lambda\mathbf{I} - i\mathbf{R} + \mathbf{M}]^{-1}_{1,1}
\end{aligned}
\tag{2.18}
$$

where $\lambda = s - j\delta = \frac{f_0}{BW}(\frac{f}{f_0} - \frac{f_0}{f}) - j\frac{f_0}{BW\,Q_u}$.

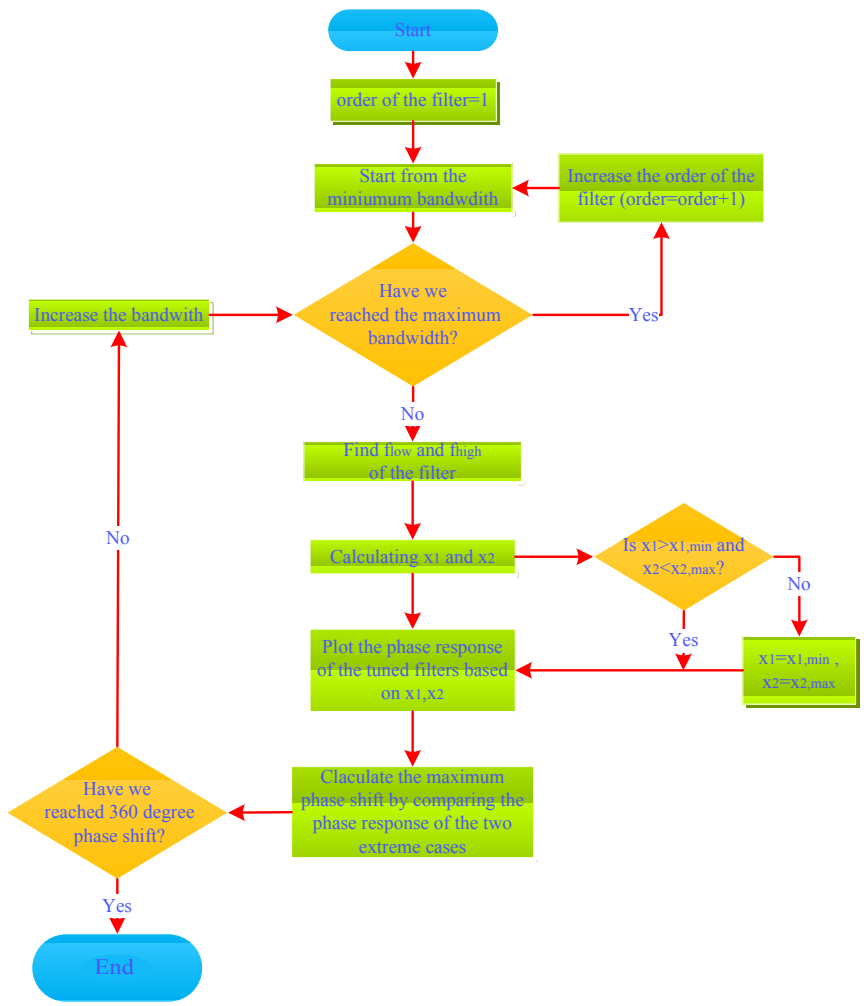

Figure 2.14: Block diagram of the iterative method for achieving 360° phase shift

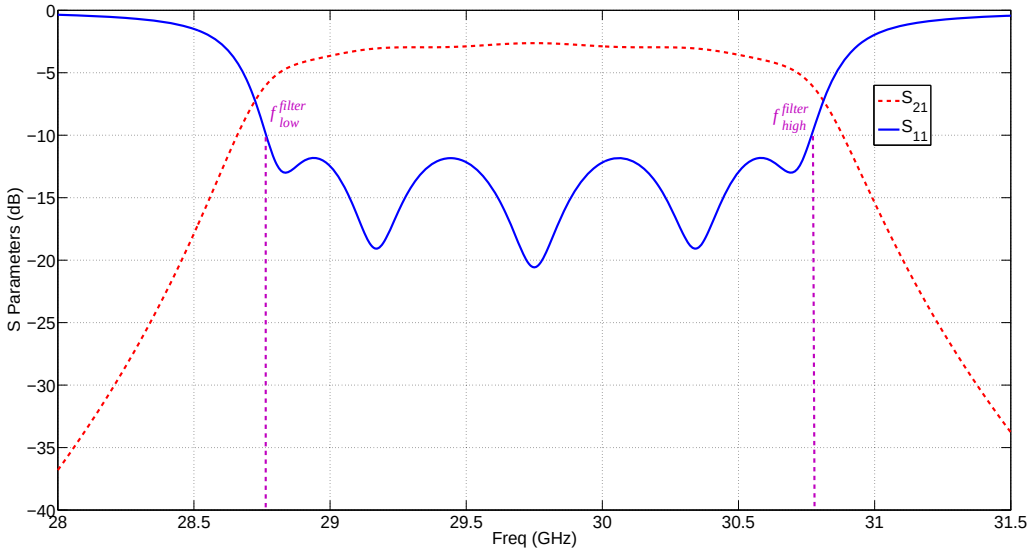

(a)

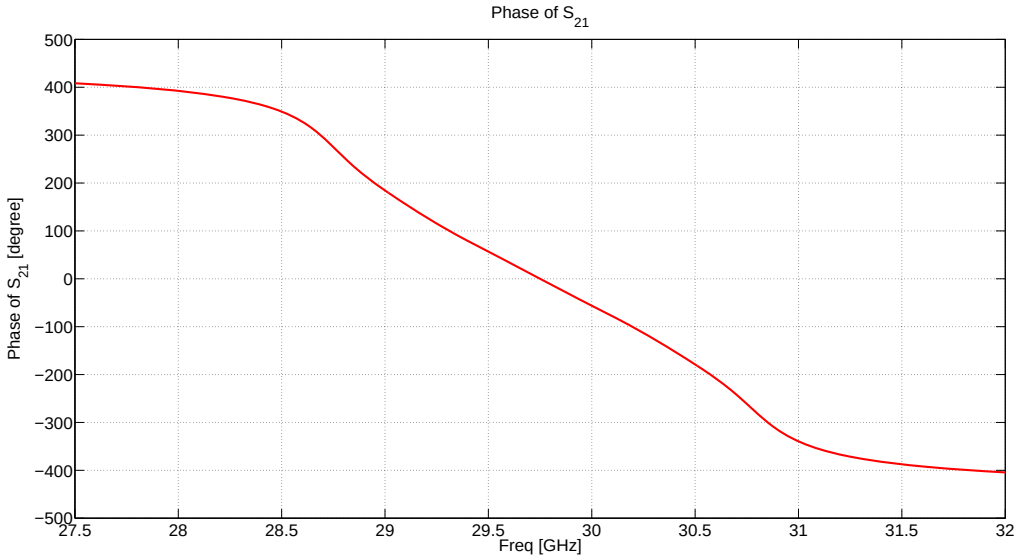

(b)

Figure 2.15: S parameters of the sample Chebyshev 2GHz 5 poles filter with 10dB return loss and $f_0 = 29.75$ GHz (a) magnitude (b) phase response

By using the iterative algorithm described in Figure 2.14, in the case of the Ka-band system under consideration, the minimum required order and bandwidth for a *Chebyshev band-pass filter* with -10 dB return loss, satisfying all mentioned criteria, is found to be 5 and 2GHz, respectively. Using equation (2.16), the band-edge frequencies of the filter are obtained as $f_{low}^{filter} = 28.767$ GHz and $f_{high}^{filter} = 30.767$ GHz. Figure 2.15 illustrates the S-parameters of this filter with a return loss of 10dB [45].

The propagation constant, β , and the characteristic impedance, Z_0, change with dielectric constant as well. Hence, the change in material constants not only shifts the center frequency of the filter, but also affects β and Z_0. The latter, however, may not be desirable.

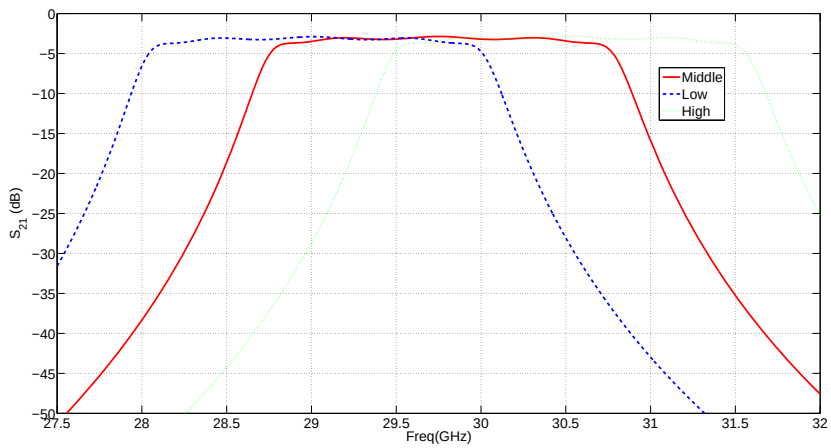

(a)

To achieve a more realistic model, β and Z_0 variations due to the pass-band shifting have been taken into consideration. Variations of the other parameters such as bandwidth and Q_u have also been accounted for in this model. It is noted that, in a filter made of transmission line segments, when the dielectric constant changes, β changes accordingly and the center frequency as well as the pass-band edges vary by the same ratio.

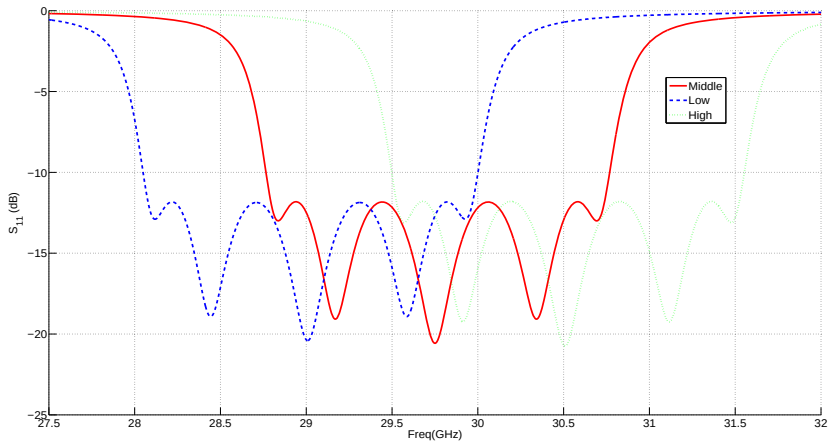

(b)

The total range of phase shift due to the center frequency shift of the band-pass filter is then calculated. Using equation (2.17) for the filter response shown in Figure 2.15, the optimal range of center frequencies is calculated as $f_{0\ shifted}^{high} = 30.508$ GHz and $f_{0\ shifted}^{low} = 29.008$ GHz. For these two shifted pass-band center frequencies, the S-parameters are plotted in Figure 2.16. As can be observed in Figure 2.16(a), the shifted filter responses provide a smooth pass-band for entire system bandwidth ($29.5 - 30$GHz).

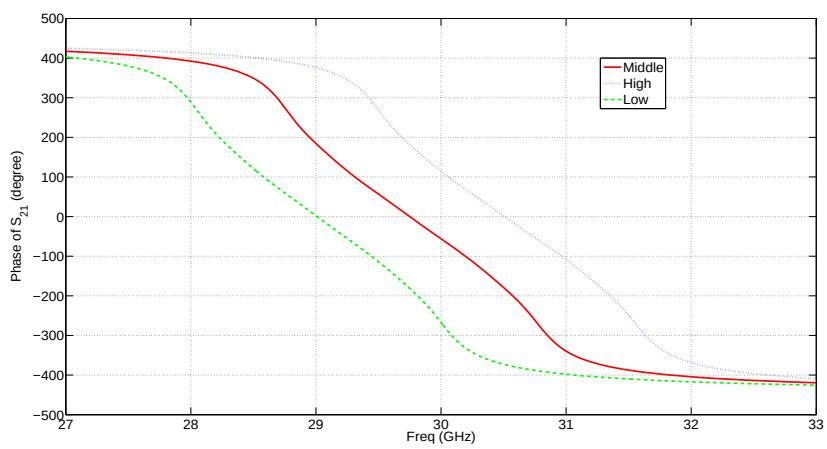

(c)

Figure 2.16: (a) magnitude of S_{21}, (b) magnitude of S_{11}, and (c) phase response S_{21} for the shifted filter at shifted center frequencies f_0,$f_{0\ shifted}^{high}$, $f_{0\ shifted}^{low}$

Note that the smooth pass-band is attributed to the fact that the ripple of the filter is largely reduced by the finite Q_u of the filter resonators at Ka-band frequencies. Having such a smooth pass-band is one of the other advantages of Filter-Type phase shifters compared to other types. Also, note that the phase shifting process is performed in the linear part of phase response, which has been shown in Figure 2.15(b). Hence, the wide-band filters with wider linear phase region are preferred.

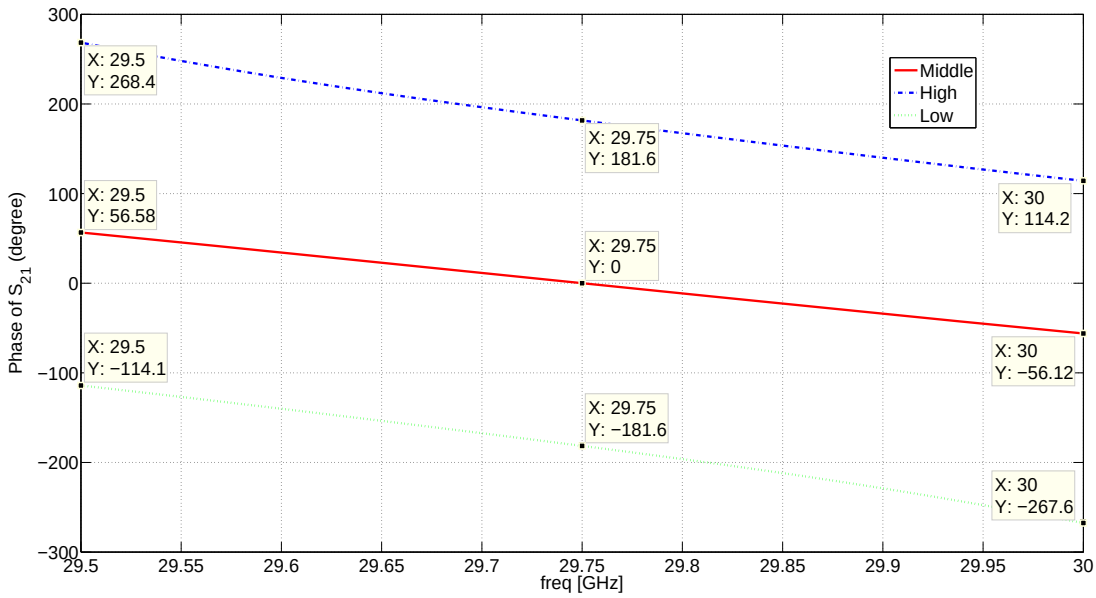

Figure 2.17: Phase response of filters in shifted center frequencies f_0,$f^{high}_{0\ shifted}$, $f^{low}_{0\ shifted}$.

Although the difference between phase-frequency plots corresponding to various phase shift states is reasonably constant near the center frequency, certain variations are observed as band-edges are approached. The effect of these variations on the phased array performance is discussed in Appendix A.

The same procedure done in this section can be applied to any other type of band-pass filter including Elliptical or Maximally Flat filters with required amplitude/phase characteristics.

2.4.3 Analysis of the effect of different parameters on the maximum phase shift

The effect of different parameters such as band-width, return loss, Q_u, order and type of the filter will be investigated in this section. Figure 2.18 shows the effect of the order of Chebyshev filter on the maximum phase shift when the bandwidth is fixed at 2 GHz and $Q_u = 200$. It should be mentioned that for the zero-order filter the maximum phase shift per wavelength of a transmission line structure as depicted in Figure 2.12, which has been derived to be 20° by simulation, has been inserted.

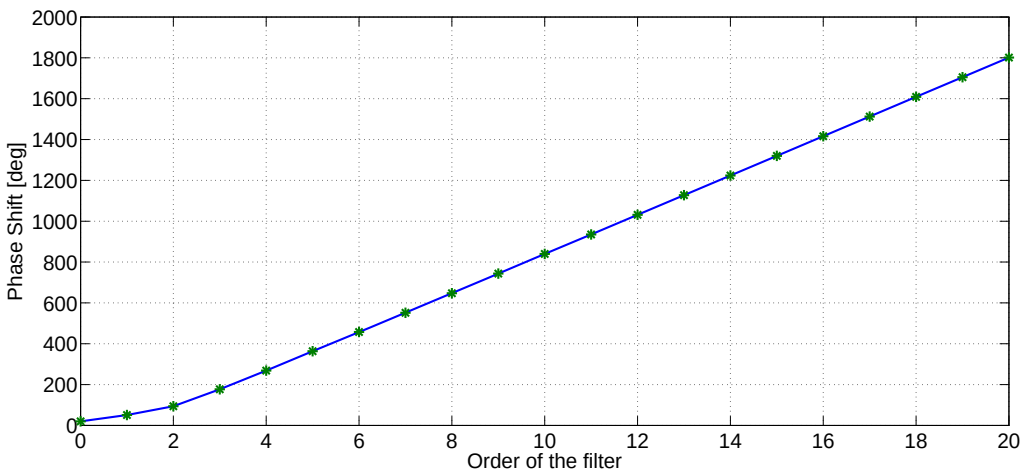

Figure 2.18: Maximum phase shift vs. the order of the Chebyshev filter with $BW = 2$GHz, $Q_u = 200$ and return loss (R.L.)$= -10$dB

Figure 2.19 shows the maximum phase shift per wavelength for different orders of Chebyshev filter with different values of bandwidth and $Q_u = 200$. According to 2.19, increasing the filter order while the order of the filter is still low will have higher impact on the maximum phase shift per wavelength with respect to the condition that the order of the filter is large.

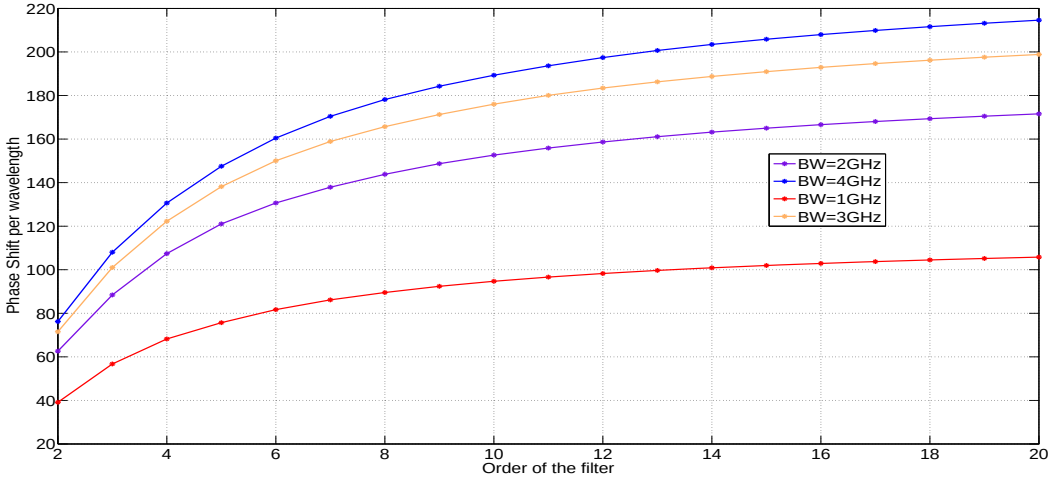

Figure 2.19: Maximum phase shift per wavelength vs. the order of the Chebyshev filter for $Q_u = 200$ and return loss (R.L.)$= -10$dB

This principle means that increasing the order of filter from 2 to 3 will have greater benefit in terms of the phase shift per space (or length) than increasing the order of filter from 5 to 6.

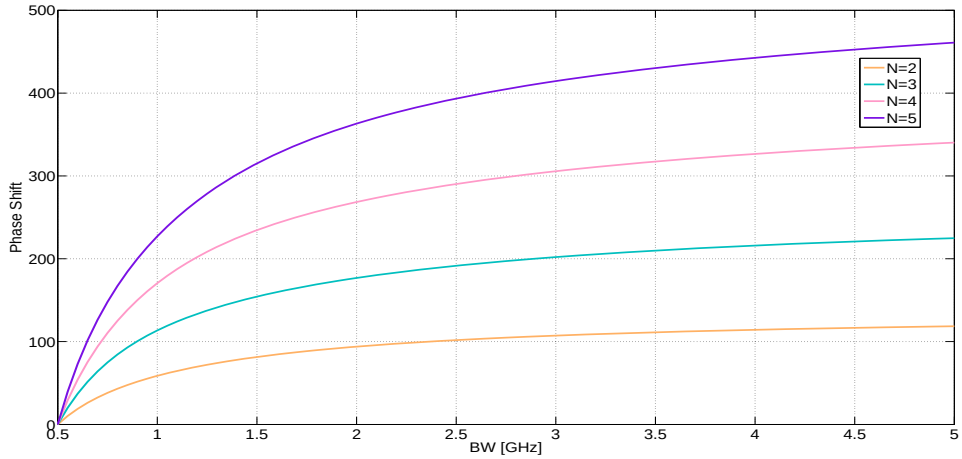

Figure 2.20: Maximum Phase-Shift for different order of Chebyshev filters vs. bandwidth when no restriction exist on tunability ($Q_u = 200$ R.L.$= -10$dB)

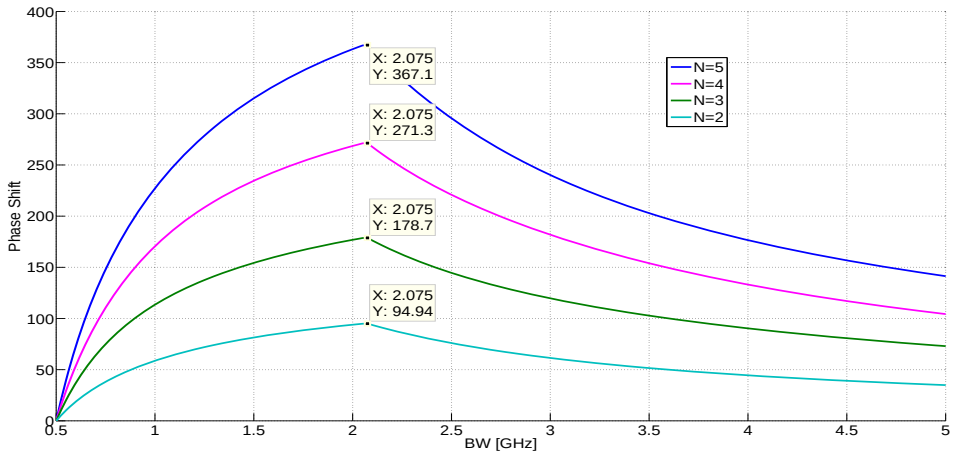

Figure 2.21: Maximum Phase-Shift for different order of Chebyshev filters vs. bandwidth by applying the restriction on the maximum tunability ($Q_u = 200$ R.L.$= -10$dB)

Supposing that there is no restriction on the tunability of our LC medium, Figure 2.20 exhibits the effect of increasing the bandwidth on the maximum phase for different order of Chebysheve filters. If the restrictions on the tunability of LCs is applied by inserting the value of x_1, x_2 based on equation (2.12) into the equation (2.17), the maximum phase shift vs. the bandwidth of Chebyshev filter can be demonstrated as Figure 2.21.

It is observed from Figure 2.21 that the restriction on the maximum tunability of LC limits the maximum phase shift that a high bandwidth filter can possess. In other words, limited tunability for high bandwidth filters results in not using the whole bandwidth of the filter efficiently. Therefore, the optimal point for designing the bandwidth of the structure is actually determined by the tunable media (2.075 GHz in this case). When there is no restrictions on the tunability of the structure, it is better to design the filter as high bandwidth as possible.

The effect of loss (Q_u) of the LC on the maximum phase shift can also be investigated. Figure 2.22 shows the effect of the loss (Q_u) on the maximum phase shift for different order of Chebyshev filters when $BW = 2$ GHz.

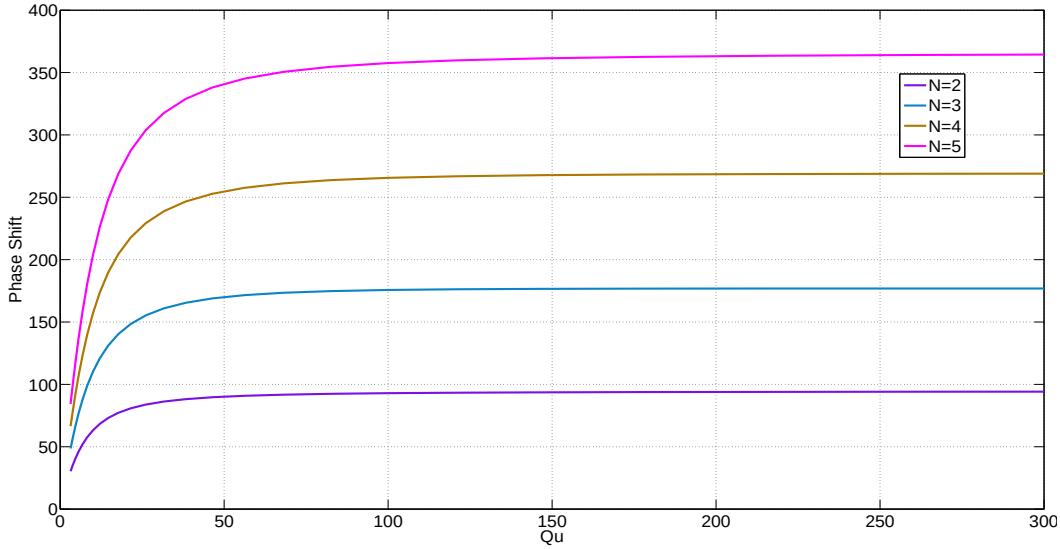

Figure 2.22: Maximum Phase-Shift for different order of Chebyshev filters vs. Q_u (BW= 2 GHz R.L.= -10dB)

As it can be seen in Figure 2.22 when Q_u is higher than 120, we have almost constant phase shift. For the structure presented in Figure 2.12 the Q_u varies between 86.4 to 99.7 for $\varepsilon_{r,eff_\perp}$ and $\varepsilon_{r,eff_\parallel}$, and due to the loss originating from other materials, such as copper loss, dielectric loss of $RO4003$. It is worth mentioning that based on values of $\tan\delta$ for LC, its Q_u will be greater than 150. Therefore, although the LC is not the main source of lowering Q_u, the variation in the overall Q_u of the structure under consideration needs to be investigated for determining the accurate value for the maximum phase shift. According to Figure 2.22 for smaller values of Q_u, the variation of the phase shift is increasing by the order of the filter.

In the same manner, Figure 2.23 shows the effect of the loss (Q_u) on the maximum phase shift of the 5th order Chebyshev filter for different values of bandwidth.

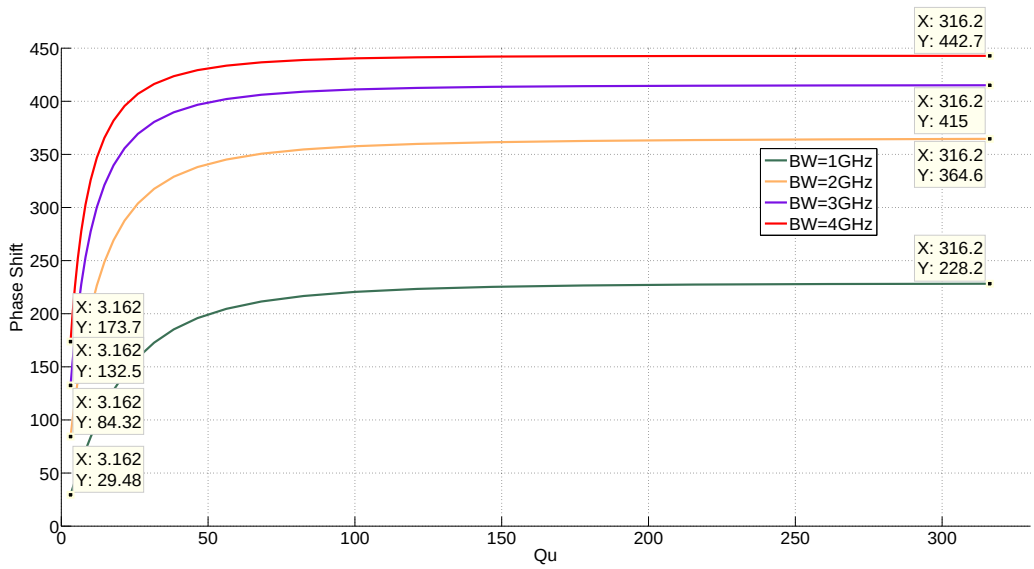

Figure 2.23: maximum phase shift vs. Q_u for different values of bandwidth (N= 5 GHz R.L.= -10dB)

According to Figure 2.23, the effect of loss on the maximum phase shift for higher bandwidth filters will be more intensive.

In all of the previous figures it was assumed that the return loss of filters has been set to -10dB. Figure 2.24 shows the effect of changing the return loss on the maximum phase of different order of Chebyshev filters.

The poles of the Nth order Chebyshev filter are:

$$\begin{aligned} P_n(k) &= -a\, sin(\frac{(2k-1)\pi}{2n}) + j\, b\, cos(\frac{(2k-1)\pi}{2n}) \\ a &= sinh(\frac{1}{n} sinh^{-1}(\frac{1}{\varepsilon})),\ a = cosh(\frac{1}{n} cosh^{-1}(\frac{1}{\varepsilon})) \\ \varepsilon^2 &= \frac{1}{1-10^{(\frac{RL}{10})}} - 1,\ RL = returnloss \end{aligned} \tag{2.19}$$

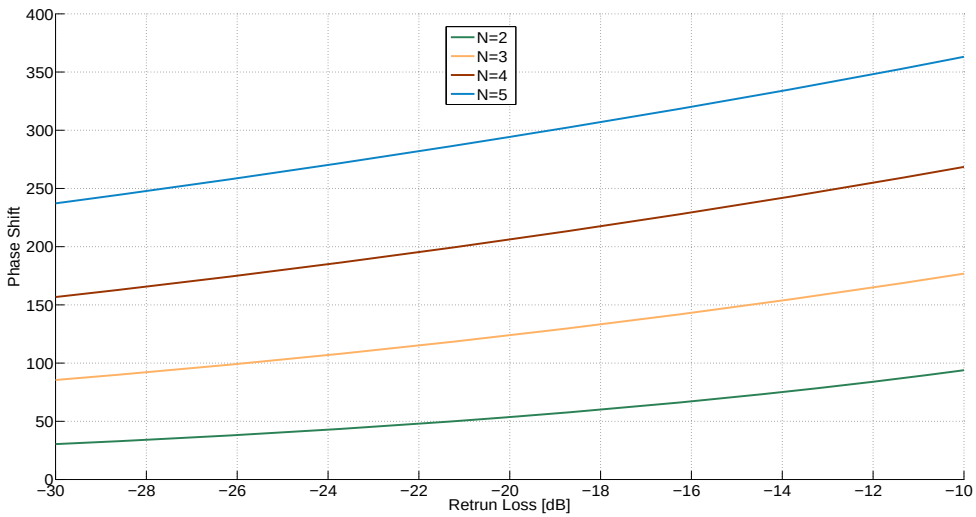

Figure 2.24: maximum phase shift vs return loss for different order of filter (BW=2 GHz $Q_u = 200$)

According to Figure 2.24, there is trade-off between return loss and the maximum phase shift of a filter. The reason is that return loss is a function of ε of the filter. The smaller ε, the smaller the return loss will be; as ε becomes smaller the poles are going to be farther from the imaginary axis (ω axis) and the $\tan^{-1}(x)$ function is going to be expanded and the phase shift in our desired frequency will decrease.

The same analysis can be performed on other types of filters (Maximally flat or Elliptical) leading to more or less similar results.

Chapter 3

BST Phase Shifters

3.1 Introduction

In this chapter, an investigation on BST phase shifters will be done. Furthermore, the characteristics of BST materials, the two main phases (ferroelectric, para-electric) along with the applications of thin and/or thick film BSTs will be discussed. A literature review on different proposed structures for BST phase shifter will be presented afterward; pros and cons of each structure will be detailed. Our proposed structure and simulation results including the maximum phase shift, using BST parameters will be demonstrated. The realization of BST phase shifters in the form of all-pass networks and the analytical formulation and design strategy will be the final topic of this chapter.

For many steerable antenna systems, it is highly preferable to replace the mechanical part of the motion with electronic scanning for a faster tracking of mobile communication users. A typical phased array antenna may require thousands of element to ensure enough gain for reception and transmission of data. A typical Transmission-Reception module consists of [47]

- Phase shifters (PS)
- Power Amplifiers (PA)
- Low Noise Amplifiers (LNA)

Tunable phase shifters are considered the most important component and directly decide the cost and performance of a Phased-Array Antenna system [48]. In the case of arrays

with a large number of elements, the cost, drive power consumption and the size of phase shifters are critical issues. Depending on the device requirement, there are different possible solutions for Tunable Phase-Shifters like PIN, varactor and Schottky diodes, Micro-Electro-Mechanical Systems (MEMS) [49], ferrites, liquid crystals (discussed in Chapter 2) or tunable dielectrics. Barium-Strontium-Titanates (BSTs) are good candidates for voltage-controlled devices at microwave frequency and millimeter wave applications [50] since they offer the possibility of lowering the total cost of phased arrays.

The utilization of BSTs for microwave application had been limited in the past due to the high losses of these materials $\tan(\delta) \geq 0.3$ and the high electric field necessary for biasing voltage in order to provide the substantial dielectric constant change. New fabrication techniques and the possibility of depositing thin layer BST on substrates paved the way to commercialize the BST type tunable devices for microwave and millimeter wave applications. New fabrication methods such as sol-gel techniques [51, 52, 53], combined with use of thin ceramics greatly reduces the insertion loss and the bias voltage with almost no power consumption [54]. The major advantage of ferroelectric based phase shifters compared to other types such as ferromagnetic phase shifters are the faster phase-shift capability, the smaller and lighter structure and higher power handling.

3.2 Basic Physics of BST

Tunable Dielectric refers to a material whose permittivity can be changed through the application of an external DC voltage. Tunable dielectric, when used in the place of an ordinary dielectric capacitor, adds flexibility and functionality to communication electronics. At the present, the known tunable dielectrics can be categorized into materials with or without ferroelectric instabilities [55]. The first category will be discussed here and includes Barium-Strontium-Titanates (BST). It includes both materials which undergo a ferroelectric transition (barium titanate) and those whose ferroelectric transition is suppressed by quantum fluctuations (strontium titanate). The second category of tunable dielectrics (non-ferroelectric) is comprised of materials whose tunability results form the rearrangement of off-center ion (like bismuth zinc niobate [56, 57, 58, 59]).

Bulk barium titanate is ferroelectric with a T_c of 393 K. Above T_c, in the para-electric phase, the structure is cubic, as illustrated in Figure 3.1(left). Below T_c, the positive ions (cations) in the unit cell shift, resulting in a net dipole moment, as shown in Figure 3.1(right). BST $Ba_xSr_{1-x}TiO_3$ is a solid solution of $BaTiO_3$ and $SrTiO_3$ with $(x : 1-x)$ ratio. At room temperature, bulk strontium titanate is para-electric. The nominal thin film BSTs are $Ba_{0.5}Sr_{0.5}TiO_3$ and $Ba_{0.3}Sr_{0.7}TiO_3$ which are para-electric at room temperature

with ferroelectric transitions just below room temperature. This close proximity to the ferroelectric transition results in a high tunability.

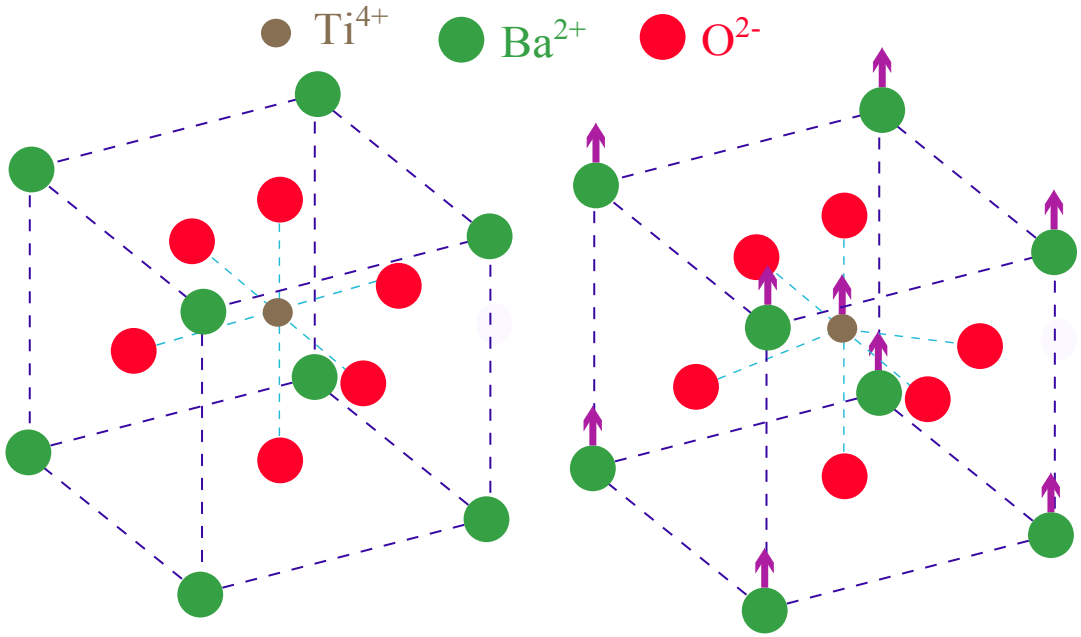

Figure 3.1: Unit cell of barium titanate in its para-electric phase (left) ferroelectric phase (right)

Generally, when Ba/Sr ratio is less than 7/3 the BST material is in the para-electric phase at room temperature(above the Curie Temperature T_c [1]), like $x = 0.5$, however, $Ba_{0.6}Sr_{0.4}TiO_3$ thin films present the ferroelectric hysteresis loop in the capacitance vs. voltage $(C - V)$ curve. This small hysteresis effect can be observed in Figure 3.2. Some of the thick films of $Ba_{0.6}Sr_{0.4}TiO_3$ operate in para-electric phase at room temperature and are free of hysteresis, in both phases BST is used fpr phase shifting applications.

[1] The temperature where a material's permanent electric moment changes to induced electric moments

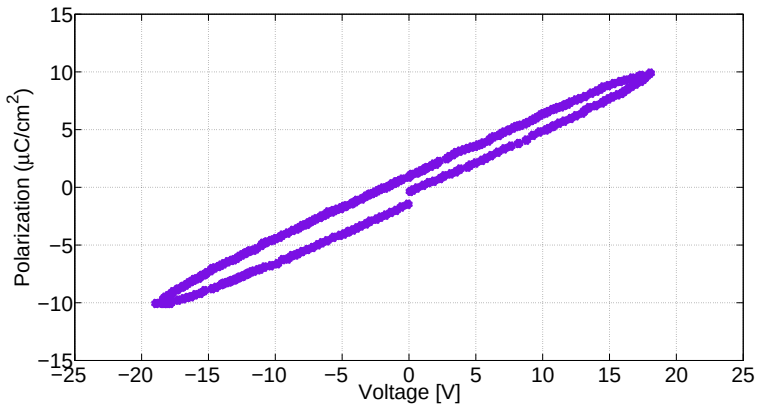

Figure 3.2: Hysteresis loop for BST thin film [47]

It has been investigated in [60] that by adding $MgTiO_3$ or MgO to $BaTiO_3$ and $SrTiO_3$ one can achieve a lower loss material at higher frequencies.

When the applied electric field is perpendicular to the direction of propagation, the dielectric constant of the material can be modulated under the effect of the dielectric bias as shown Figure 3.3.

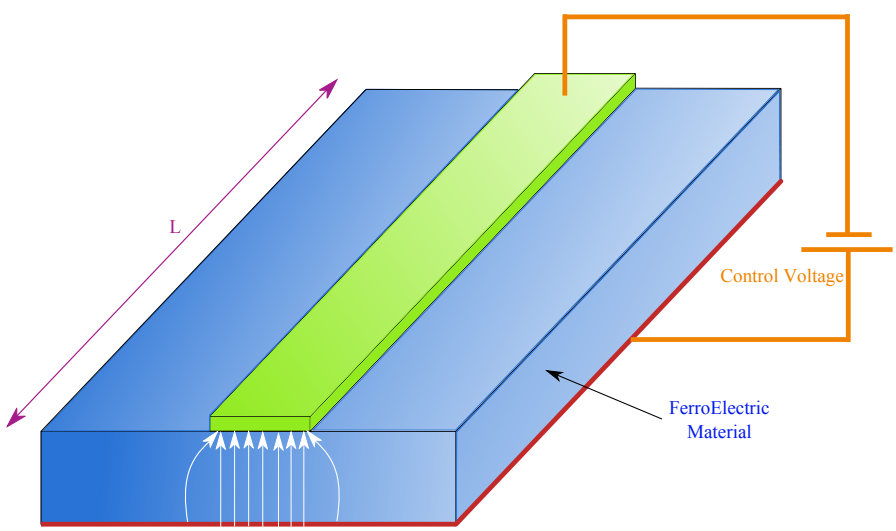

Figure 3.3: The structure of ferroelectric microstrip phase shifter [54]

In phase shifter circuits the ferroelectric material (BST) either forms the entire microwave substrate [54] on which the conductor is deposited or a fraction of the substrate with thin BST films sandwiched between the main substrate and the conductors ([61, 62, 63, 63]).

In general, the principle of BST circuits is based on the idea that by passing a part or all of the wave through the ferroelectric layer the phase velocity of wave propagating on these structures can be altered by changing the permittivity of the ferroelectric layer. In other words, the propagation constant β will depend on the bias field since $\beta = 2\pi\sqrt{\varepsilon_r}/\lambda_0$ and $\varepsilon_r = \varepsilon_{r(V_{bias})}$. The total wave delay will become a function of the bias field, and will produce a phase shift of $\Delta\varphi = \Delta\beta\ell$, where ℓ is the length of the line (Figure 3.3). BSTs have much faster switching time (usually in order of nanoseconds (ns)) compared to LCs, where the switching time is around tens of milliseconds (ms).

The basic definitions related to the phase shift and/or tunability of ferroelectric materials (BST) are the same as what defined in chapter 2 for relative tunability, τ, and figure of merit, FoM [2]. The additional definitions used here are as following:

1. α: is defined as the ratio of the zero-bias capacitance and the minimum capacitance.

2. Loading factor x: is defined as the ratio per unit length between unbiased IDC (inter-digital capacitance), generally the measured capacitor in the structure or the distributed capacitor in transmission line.

[2]Different definitions has been proposed for figure of merit but the most conventional one is what defined in chapter 2

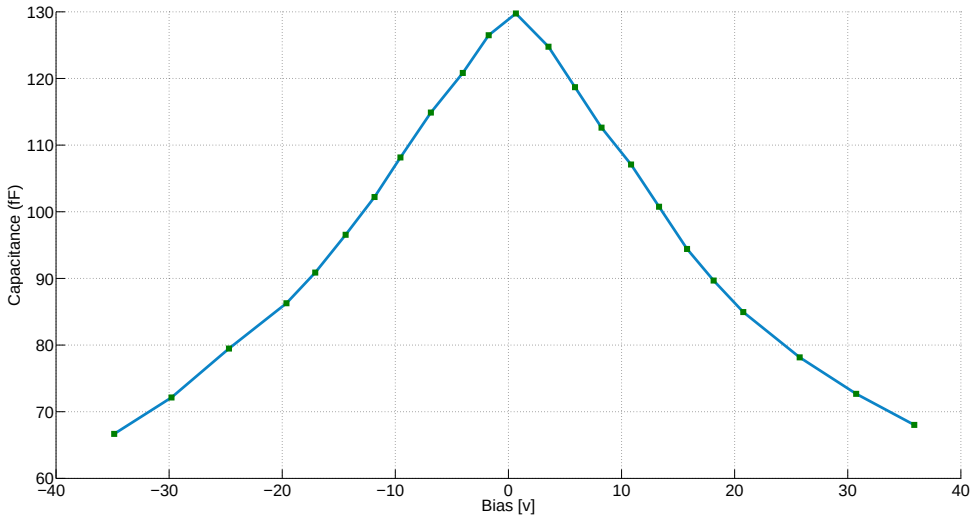

Figure 3.4: Capacitor Voltage characteristics measured at 22GHz [64]

Based on the above definitions τ is written as $\tau = \frac{\alpha-1}{\alpha}$. An example for the variation of the tunable capacitance measured at $22GHz$ is shown in Figure 3.4.

3.3 Literature Review of BST based phase shifters

Different implementation of phase shifters using BST exist in the literature for Ka-band frequency applications such as reflection type phase shifters, traveling wave structures and filter type phase shifters. The traveling wave structures are widely used such as CPW line phase shifters [65], which can be utilized as Periodically Loaded Transmission (delay) Line. The other traveling wave structure which can be used is the Tunable Left Handed (LH) transmission line. The tunable components are created by Inter digital Capacitors(IDCs) or metal-insulator-metal (MIM).

3.3.1 Periodically Loaded Transmission Line phase shifters

By using a coplanar waveguide structure it is possible to provide the loaded capacitance between the signal and ground more easily. Therefore, many periodically loaded transmis-

sion line phoase shifters are based on the CPW structures. Applications of these types of structures as phase shifters have been reported in [47, 66, 67, 68, 64].

Introduction to Periodically Loaded Transmission Line phase shifters

In this class of phase shifters, tunable loaded capacitance is added in addition to the capacitance (F/m) of the line. The equivalent circuit model of the unit cell with a series inductance and shunt capacitance along with the loaded capacitance is shown in Figure 3.5.

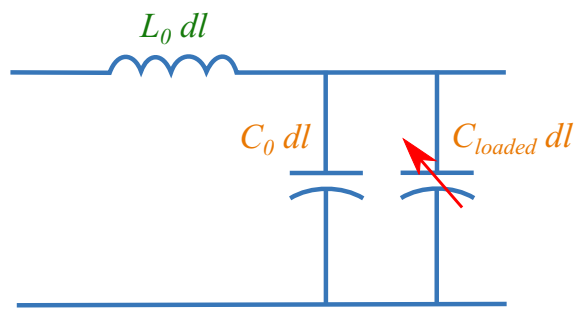

Figure 3.5: Equivalent circuit of a loaded transmission line unit cell with L_0 and C_0 as the inductance and capacitance per meter and C_{loaded} as the loaded tunable capacitor [68]

In the ideal case without any loading the characteristic impedance and phase velocity will be

$$Z_0 = \sqrt{\frac{L_0}{C_o}} \qquad V_p = \frac{1}{\sqrt{L_0 C_0}} \tag{3.1}$$

After adding the loading capacitance the characteristic impedance and phase velocity will become

$$Z_0 = \sqrt{\frac{L_0}{C_0 + C_{loaded}}} \qquad V_p = \frac{1}{\sqrt{L_0(C_0 + C_{loaded})}} \tag{3.2}$$

So the change in the variable capacitance (C_{loaded}) leads to changing the phase velocity and consequently the propagation constant. Furthermore, the characteristic impedance of the transmission line also varies, which may be an undesired effect. Therefore, it is

necessary that the intrinsic characteristic impedance of transmission line be larger than the characteristic impedance of the tuned transmission line in order to achive an impedance match. To get a compact full range phase shifter, a high contribution of the phase shifting is expected from each unit cell of the periodically loaded line. Thus, the number of the unit cells can be reduced leading to a reduction in the toal length. On the other hand, high phase shift is obtained if the tunable capacitance is large compared to the non-tunable capacitance C_0. This is for the sake of reducing the line characteristic impedance; so in order to compensate the mismatch imposed, one should increase the inductance of the transmission line. In the case of a CPW line, this can be done by either changing the signal line or the ground one.

The other aspect which should be noticed regarding the design of these loaded transmission lines is their periodic nature [69]. The discontinuities created by adding the shunt elements results in reflections from each element as the signal propagates through the line. As the frequency of the signal is increasing the phases of incident and reflected waves interfere destructively with each other, prohibiting the signal from forward propagation; the insertion loss increases and the signal is reflected back toward the source. The frequency at which the signal is totally prevented from forward propagation is called the Bragg frequency:

$$f_{Bragg} = \frac{1}{\pi \Delta l \sqrt{L_0(C_0 + C_{loaded})}} \tag{3.3}$$

In order to model the differential phase shift of a periodically loaded tranmission line mathematical modeling can be utilized. Assuming that $\delta L_0 = L_0 \Delta l$ and $\delta C_0 = C_0 \Delta l$, the initial phase constant will be:

$$\beta_0 = 2\pi f \sqrt{L_0 C_0} = \frac{2\pi f}{\Delta l} \sqrt{\delta L_0 \delta C_0} \tag{3.4}$$

By calculating the initial phase and the phase corresponding to applied voltage V, the phase difference will be obtained as:

$$\begin{aligned} \varphi(0) &= 2\pi f \sqrt{\delta L_0 [\delta C_0 + C(0)]} \\ \varphi(V) &= 2\pi f \sqrt{\delta L_0 [\delta C_0 + C(V)]} \\ \Delta\varphi = \varphi(V) - \varphi(0) &= \beta_0 \Delta l [\sqrt{1+x} - \sqrt{1+\alpha x}] \end{aligned} \tag{3.5}$$

where $\alpha = C(V)/C(0)$ and $x = C(0)/\delta C_0$ (loading factor). Using equation (3.3), the differential phase shift can be written as:

$$\Delta\varphi = 2\pi f \Delta l \sqrt{L_0}(\sqrt{C_0 + C(V)} - \sqrt{C_0 + C(0)}) = \frac{2f}{f_B}[1 - \sqrt{\frac{1 + x\alpha}{1 + x}}] \tag{3.6}$$

Δl is the parameter which can be adjusted to change the Bragg frequency independent of the transmission line parameters. In order to avoid the insertion loss due to the Bragg frequency, the highest operating frequency of the phase shifter should be significantly smaller than f_{Bragg}. By increasing Δl, the Bragg frequency will become closer to the operating frequency. However, the number of sections needed to achieve the desired phase shift will be reduced. Comparison between the experimental values and the analytical model are shown in Figure 3.6

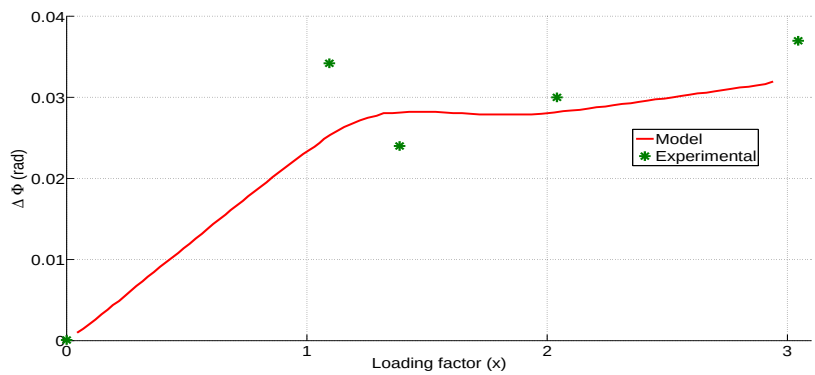

(a)

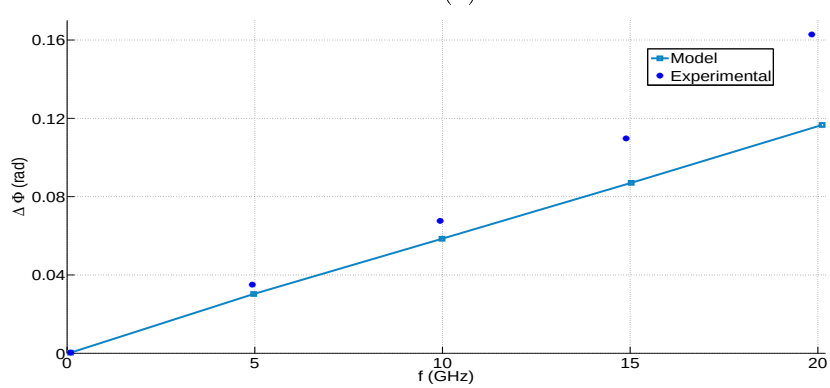

(b)

Figure 3.6: a) The maximum phase shift vs loading factor calculated by the model in comparison with the experiment b) frequency variation of $\Delta\Phi_{max}$ when $x = 1.4$ [64]

Instances of Periodically Loaded Transmission Line phase shifters

An example of Periodically Loaded Transmission Line phase shifters is presented in [66] where a CPW line (with characteristic impedance of 100Ω and $150nm$ tickness) is fabricated on high resistive silicon ($40K\Omega - cm$) wafer. The CPW was periodically loaded with BST capacitors with zero bias capacitance of $96fF$. Platinum was used at the top and bottom electrodes for BST capacitors. The length of the unit cell (spacing between capacitors) was chosen to be $340\mu m$ resulting in a much higher Bragg frequency. In order to get a phase shift of 160° (at 30 GHz) 9 identical cells were connected in series, resulting in a total length of $3.06mm$. The CPW center conductor and Gap dimensions are $15\mu m$ and $150\mu m$ respectively. The loaded capacitors were implemented using two devices of $48fF$ each (active area $3\mu m^2$), connected in parallel from the CPW signal line to either ground conductor.

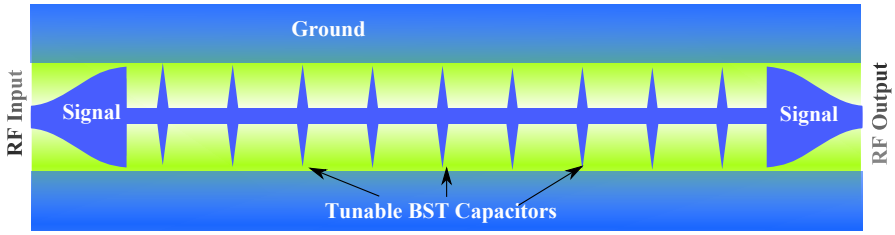

Figure 3.7: Layout of the fabricated phase shifter [66]

In the structure shown in Figure 3.7 the capacitance will decrease by a factor of 2.2 when a 20V bias voltage is applied. The quality factor of capacitance is estimated to be 10. The insertion loss of the phase shifter shown in Figure 3.7 is increasing due to an increase in the frequency and decreasing due to an increase in the bias voltage. This is because of low quality factor of the BST and the fact that the BST layer consists of the whole structure. Another issue that BSTs usually suffer from is not the high insertion loss, but the variation of insertion loss for different phase shift values. Further improvement in characterization of BST technology leads to advent of phase shifters with better performance in terms of insertion loss.

Similar structure to Figure 3.7 has been shown in [47] for center frequency of 28GHz, silicon substrate with thickness of $500\mu m$ and BST film with zero bias dielectric constant $\varepsilon_r = 300$ and thickness of $0.5\mu m$. The authors have used the area of the structure more effectively in order to increase the length of phase shifter to achieve maximum phase shift of 170° by applying 20V bias voltage.

The other example of this kind [68] uses a $Ba_{0.6}Sr_{0.4}TiO_3$ thick film with an untuned dielectric constant of 365 and tunability of $\tau = 38\%$ ($\varepsilon_{low} = 225$). The material loss has been measured [70] to be $\tan(\delta) = 0.06$ at 10 GHz. The BST thick film with thickness of $3.7\mu m$ has been fabricated on a Al_2O_3 substrate with a height of $650\mu m$ and $\varepsilon_r = 10.1$. The layout of the phase shifter is shown in Figure 3.8. The phase shifter was able to produce a 127° phase shift with an insertion loss of less than 4.3dB and $FoM = 30°/dB$ at 10 GHz with the bias voltage varying from 0-140V.

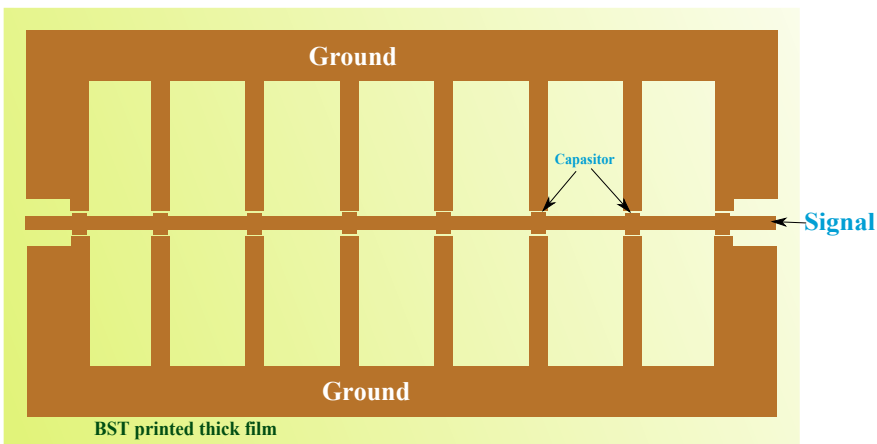

Figure 3.8: Layout of periodically loaded transmission line phase shifter consisting of 8 unit cells [68]

Utilization of BST based inter-digital capacitors(IDCs) with bias voltage varying $0-40$V is presented in [67, 64]. It is reported achieving a 360° phase shift at 30 GHz with 40V and at 40 GHz with 17V bias voltage. It has been also shown in [67] that the phase shifter in para-electric phase ($Ba_{0.5}Sr_{0.5}TiO_3$) shows better characteristics in terms of loss and maximum phase shift compared to the ferroelectric one($Ba_{0.8}Sr_{0.2}TiO_3$). In phase shifters with IDC, in order to have an efficient performance in terms of phase shift and insertion loss, it is imperative to take into the account the following parameters [64]:

1. Number of IDCs per unit length
2. The relevant dimensions of the IDCs
3. The location of IDCs

The loading factor is an important parameter in the design of this kind of phase shifters. Generally, the higher the loading factor, the stronger the expected effect of insertion loss. Commonly, the value of $x < 1.5$, consistent with [71], is used in the design of phase shifters. The frequency dependence on the phase of S_{21} with two bias voltages (0 and 40 V) is shown in Figure 3.9. As can be observed in Figure 3.9, the insertion loss is reducing by increasing the the bias voltage to 40V. A rapid roll-off in magnitude of S_{21} is observed which can be explained by the fact that the working frequency is approaching the Bragg frequency (f_{Bragg}) above 30GHz.

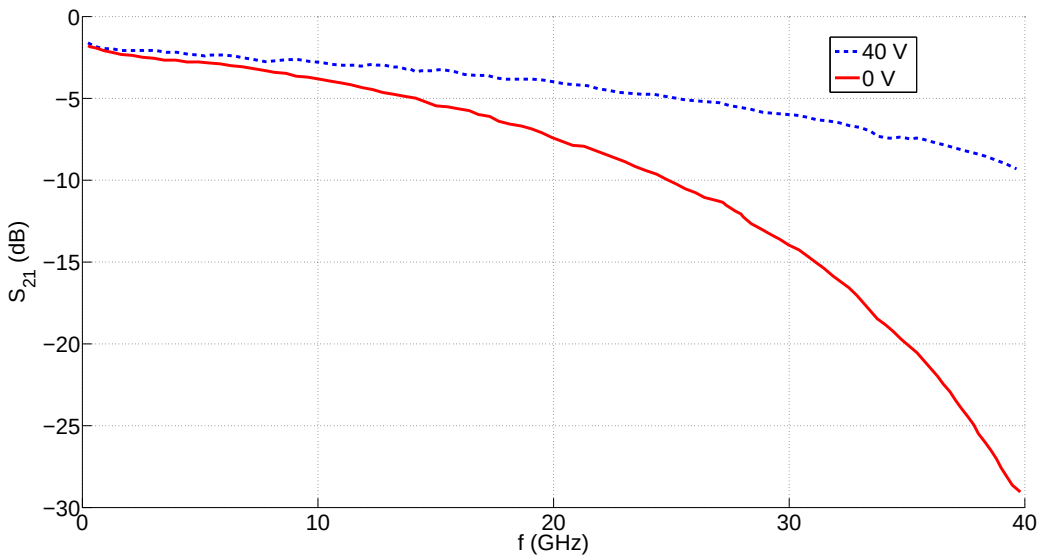

Figure 3.9: The magnitude of S_{21} as a function of frequency [64]

There are two reasons for this behavior of insertion loss. First, the characteristic impedance of the periodic loaded transmission line is not 50Ω and by applying the 40V bias voltage it becomes closer to 50Ω. Second, the dielectric loss of BST is usually smaller when 40 V is applied with respect to the case where no bias voltage is applied.

Simulation of a Periodically Loaded TL phase shifter

In this section, a periodically loaded transmission line phase shifter has been designed and optimized using Ansoft HFSS. The permittivity of BST used in this phase shifter is

considered to vary from $260 - 350$ with a dielectric loss tangent of $0.3 - 0.4$. The total length of the designed phase shifter is less than $1mm$ and a phase shift of $90°$ is obtained. The phase shifter is shown in Figure 3.10. The length of each period has been designed in such a way as to keep the Bragg frequency much higher than the working frequency, 30 GHz.

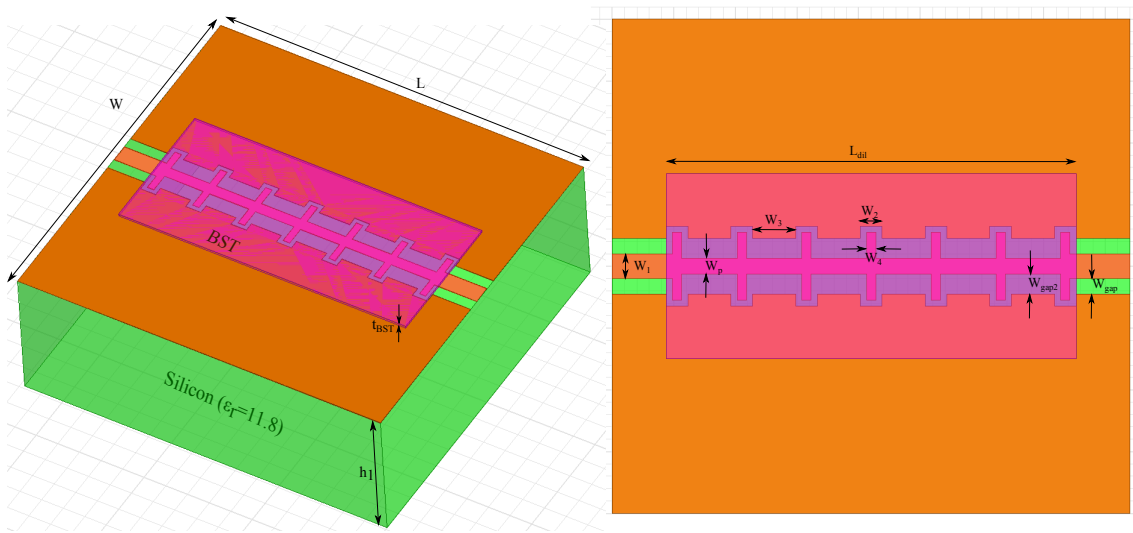

Figure 3.10: Simulated phases shifter in HFSS with dimensions

The designed parameters for the phase shifter shown in Figure 3.10 plus their corresponding values are presented in Table 3.1. The structure consist of 8 stubs, which act as load capacitors. The thickness of metal deposited on high resistive silicon is $1\mu m$. By applying the voltage the dielectric constant of the BST located on top of the substrate changes, resulting in a change in the effective dielectric constant of the structure and the propagation constant β.

Table 3.1: Design Parameters of the phase shifter shown in Figure 3.10

Parameters	L	W	W_p	W_1	W_2	W_3	W_4	W_{gap}	W_{gap2}	h_1	t_{BST}
Value (mm)	0.84	0.8	0.025	0.04	0.035	0.07	0.015	0.03	0.0375	0.3	0.005

A part of the substrate's area is in touch with the BST, having a high permittivity. Being in contact with high permittivity, the characteristic impedance of the line under

the BST is decreased by an inverse square root function of the effective permittivity; it was calculated to decrease to 23Ω. In order to compensate this effect two solution can be applied. First, increasing W_{gap} to W_{gap2} and second reducing the width of the signal line from W_1 to W_p. Using this technique in the vicinity of the high dielectric BST, the mismatch in the input was effectively eliminated. The structure has been optimized for acceptable insertion loss and return loss in addition to obtaining the maximum phase shift at 30 GHz. The result of simulations for the scattering parameters and phase shift are shown in Figure 3.11.

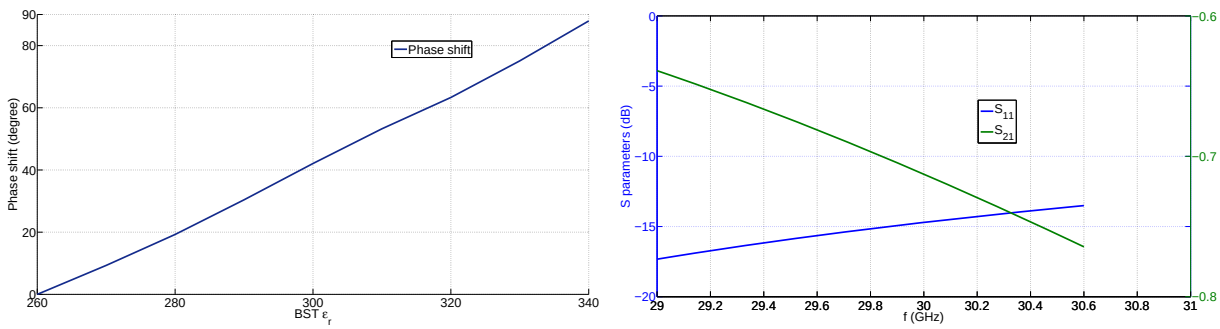

(a) (b)

Figure 3.11: a) Phase of the structure (degree) vs dielectric constant of BST material b) S parameters of the simulated structure in the frequency range of $29 - 30.5$ GHz for $\varepsilon_{r,BST} = 300$

Although the S parameter results, reported in Figure 3.11, are for $\varepsilon_{r,BST} = 300$, the fact that the return loss value in all phase shifting steps is lower than -10dB was of prime concern in this design. The total length of the designed phase shifter shown in Figure 3.10 is 0.84mm and is capable of creating an 87° phase shift. By repeating the periods of transmission line phase shifter and increasing the length to $3mm$ it is expected to achieve more than 270° of differential phase shift.

3.3.2 Tunable left-handed (LH) Transmission Line

Introduction to left-handed (LH) Transmission Line phase shifters

Left handed transmission lines are the other class of BST based phase shifters. They are very compact and therefore well suited for phased array antennas. Left-Handed (LH)

transmission lines can be physically shorter than the conventional transmission lines while having the same electrical length; this is because of their larger absolute value for the phase constant. In other words, the propagation constant of a LH line has higher sensitivity to the value of the capacitance than the RH lines [72].The equivalent circuit for LH lines consists of a series capacitor and shunt inductor. In comparison with right-handed transmission lines, the positions of the elements L_0 and C_0 in LH lines are swapped into series capacitance and shunt inductance. This results in an inverse propagation constant for the transmission line [73]:

$$\gamma_{RH} = j\omega\sqrt{L_0 C_0} \qquad \gamma_{LH} = \frac{-j}{\omega}\sqrt{\frac{1}{L_0 C_0}} \tag{3.7}$$

The characteristic impedance for both types of transmission lines is written as:

$$Z_{RH} = Z_{LH} = \sqrt{\frac{L_0}{C_0}} \tag{3.8}$$

By using tunable capacitors, the propagation constant changes, and thus a differential phase shift is achieved.

An example of LH Transmission Line phase shifters

A very compact LH transmission line phase shifter based on CPW structure for measurement is presented in [74] achieving $FoM = 52°/dB$. Using this phase shifter, a fully integrated phased array was designed in [75].

It is worth mentioning that most reported phase shifter designs are unbalanced [68], since they are based on a single-ended transmission lines such as microstrip or CPW lines. In terms of design efficiency, balanced phase shifters are desirable for RF front-ends and phased arrays, because they can be connected to differential amplifiers or differential antennas, such as dipoles, without any need for baluns. Furthermore, the additional performance limitation and bandwidth reduction caused by baluns is also avoided and the structure is kept more compact. Two balanced (differential) left-handed coplanar strip (LH CPS) phase shifters are presented in [68]. The phase shifter designs performed in [68] is depicted in Figure 3.12. The two designs were capable of creating more than 360° phase shift at 10 GHz by applying $0 - 160$V bias voltage [68].

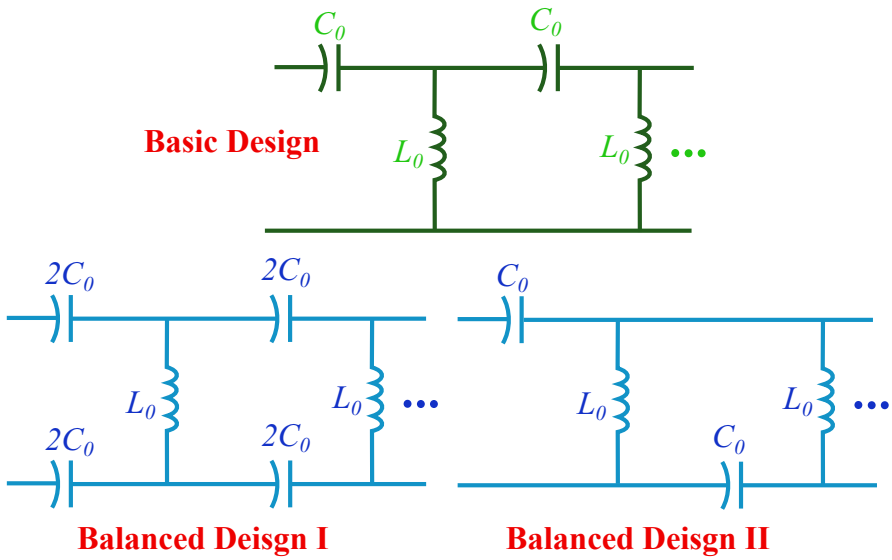

Figure 3.12: The equivalent circuit for Left-handed transmission line, basic (unbalanced) and balanced designs [68]

3.4 Filter-type BST based phase shifters

The utilization of liquid crystal based band-pass filter as phase shifters was discussed rigorously in section 2.4. The realization of BST based band-pass phase shifter are also observed in [38, 39]. Due to the fact that BSTs usually have higher tunability compared to liquid crystal materials, they can be utilized in wide-band filters to perform phase shifting. All-Pass filters (networks) theoretically provide an infinite bandwidth. Although all-pass filters practically provide a finite bandwidth, the available bandwidth is still large enough to eliminate any concern about containing the system bandwidth inside the pass band of the filter. In the structures described earlier in section 3.3, the Bragg frequency is the source of problems, leading to a large increase in insertion loss and limiting the achievable phase shift of each unit cell. All-pass networks usually counteract this increase in loss due to their bridging element, if designed properly leading to a flat response over all frequencies [76].

The transfer function of an all-pass network is defined as

$$S_{21}(p) = \frac{D(-p)}{D(p)} \tag{3.9}$$

where $p = \sigma + j\omega$ is the complex variable and $D(p)$ is a Hurwitz polynomial[3]. Clearly, $|S_{21}|^2 = 1$. The roots of $D(p)$ which are the poles of the filter are denoted as $p_k = \sigma_k + j\omega_k$, where $\sigma_k < 0$. All-pass filters are usually divided into two classes. If all poles and zeros of an all-pass network are located along the real axis, such a network is referred to as a *C-type all-pass network*. On the other hand, if the poles and zeros are all complex with symmetry about the origin of the complex plane, the filter is referred to as a *D-type all-pass network* [77]. C-type and D-type All-Pass networks can be also named as 1st order and/or 2nd order All-Pass networks respectively. The transfer function for the 1st and 2nd order all-pass network can be written as:

$$\begin{aligned} &1^{st}\,order\,allpass\,network \quad H(s) = \frac{s-\sigma_a}{s+\sigma_a} \\ &2^{nd}\,order\,allpass\,network \quad H(s) = \frac{s^2+2\sigma_b s+s_b^2}{s^2-2\sigma_b s+s_b^2}, \quad s_b^2 = \sigma_b^2+\omega_b^2 \end{aligned} \tag{3.10}$$

All-pass networks can be utilized as phase shifters [78, 79] in different topologies like the bridged-Tee [80, 81] lattice filter or they can even be realized using active components [82].

Since all-pass filters have flat amplitude response for all frequencies, the linearity of the phase response is used as a *criterion* for the phase shifter bandwidth to be applied in the proposed iterative method presented in Figure 2.14. In other words, the iterative method presented in section 2.4.2 can be extended to this class of networks by defining a bandwidth in phase-frequency response domain. As a linearity criterion, the variation of the phase response slope is considered to be as small as possible.

The zeros and poles are located symmetrically with respect to the imaginary axis. Hence, it is expected that with the same variation and the same pole locations as in Chebyshev filter, the phase shift obtained from the 2nd order all-pass network will be double.

The linearity of the phase response is dependent on the position of the poles and zeros of the filter ($-\sigma_b \pm j\omega_b$, $\sigma_b \pm j\omega_b$) in the complex plane. σ_b, should be optimized based on the required phase-frequency response linearity and the maximum required phase shift. It

[3]Hurwitz polynomial is a polynomial whose coefficients are positive real numbers and whose roots are located in the left half-plane of the complex plane

should be noted that the linear phase response bandwidth can be increased by reducing ω_b and increasing σ_b. For the phased array system under consideration, the designed values are $\sigma_b = 24$ and $s_b = 26$. To perform phase shifting, BST parameters are used to change the center designed frequency of the all-pass filter which leads to a shifting of the phase-frequency response. As indicated also in section 2.4.2, the extreme cases where maximum shifting occurs are limited by the obtained linearity bandwidth and the maximum tunability of the BST material. Figure 3.13 shows the phase response of the 2nd order all-pass network with the chosen parameters for two extremes and the middle phase shift states.

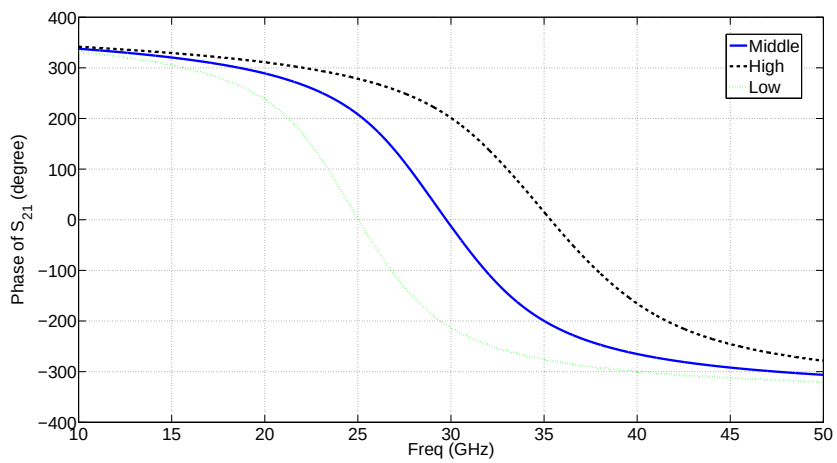

(a)

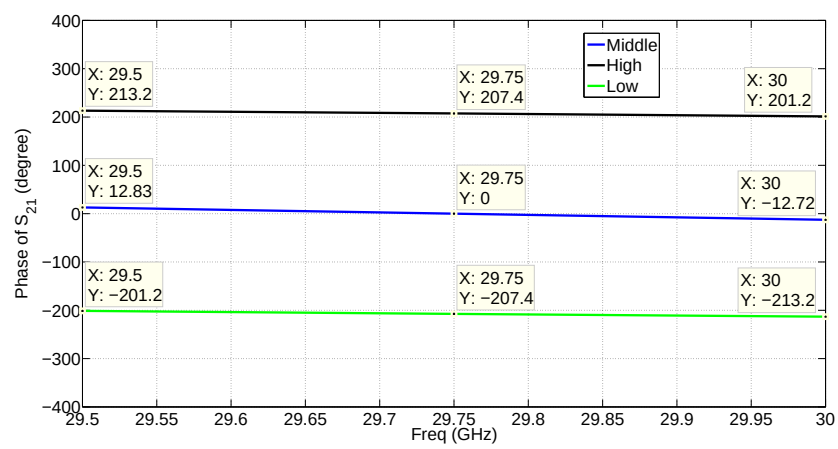

(b)

Figure 3.13: Phase response of the designed 2nd order all-pass filter

As can be observed in Figure 3.13, more than 360° phase shift is obtained from the designed 2nd order all-pass network. Although the phase shift values in the two edge frequency of the system band-width (29.5 and 30 GHz) are the same as the center frequency (29.75 GHz), a small non-linearity in phase frequency response exists in this kind of phase shifter. The effect of this small phase-frequency non-linearity on the phased array performance will be discussed in Appendix A.

Chapter 4

High Dielectric Material Phase Shifters

4.1 Introduction

In this chapter, a study on high dielectric ceramic (HDC) phase shifters will be performed. An introduction to this kind of phase shifters including a literature review will be illustrated afterward. Pros and cons of this type of phase shifters with respect to others will be discussed. Two other proposed phase shifters using high dielectric will be introduced and simulation results for obtaining the propagation constant of these structures along with the maximum phase shift values will be presented.

Being miniaturized and having low and stable insertion loss are considered to be the important characteristics of phase shifters for large Ka-Band phase array antenna systems. There has been a large amount of research into high dielectric constant, low loss ceramics suitable for microwave and mm-wave applications [83, 23]. Development of technology in this class of materials has paved the way for the realization of Ka-band phase shifters with the mentioned constraints. BST is one of the *tunable* ceramics which was discussed in detail in chapter 3.

4.2 Short literature review of HDC phase shifters

Utilization of high dielectric constant ceramics in phase shifters has been observed in the literature [84, 85]. $BaLn_2Ti_4O_{12}$ (BLT), where $Ln = La, Nd$ or Sm, is one of the ceramics having high dielectric constant with small loss tangent [86]. In [84], a 200° phase shift

has been reported using BLT ceramics with $\varepsilon_r = 85$ and 10mm length at 10 GHz. A rectangular metallic waveguide which has been partially filled with the dielectric was used for phase shifting. The height of the air gap varies from $0 - 30\mu m$ using a piezoelectric actuator by applying voltage from 150V down to -30V. The side view of the phase shifter is shown in Figure 4.1.

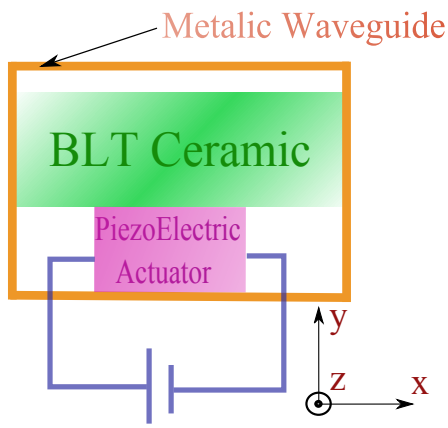

Figure 4.1: Side view of the waveguide used as phase shifter, loaded with an air-dielectric sandwich structure [84]

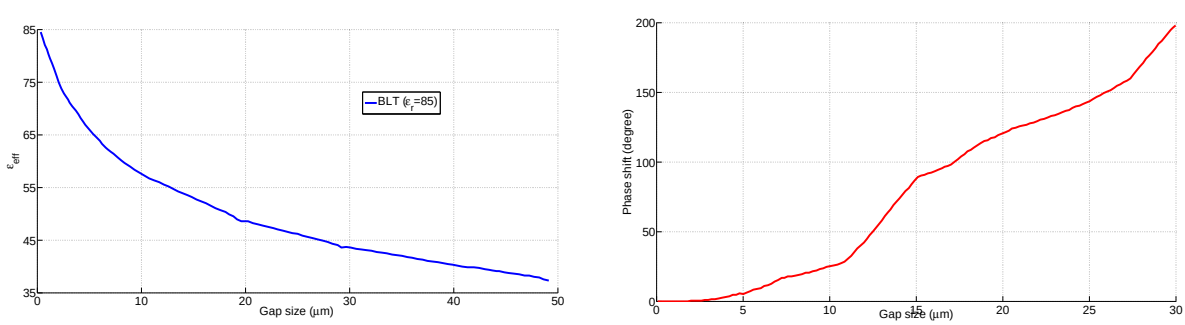

(a) (b)

Figure 4.2: a) Effective dielectric constant and b) the relative phase shift versus air gap for the air-dielectric sandwich structure for BLT $\varepsilon_r = 85$ [84]

The phase shift as a function of voltage and the effective dielectric constant of the structure is shown in Figure 4.2. For the structure shown in Figure 4.1, instead of the pure

TE^z or TM^z mode, the hybrid mode of LSM^y[1] is the dominant mode [87]. Therefore, using modal analysis the equation for finding the propagation constant of the structure will be

$$\frac{\beta_{y,air}}{\varepsilon_0}\tan(\beta_{y,air}\Delta) + \frac{\beta_{y,dil}}{\varepsilon_{dil}\varepsilon_0}\tan(\beta_{y,dil}(b-\Delta)) = 0 \tag{4.1}$$
$$\beta_{y,air} = \sqrt{\omega^2\varepsilon_0\mu_0 - \gamma^2 - \beta_x^2}, \quad \beta_{y,dil} = \sqrt{\omega^2\varepsilon_d\varepsilon_0\mu_0 - \gamma^2 - \beta_x^2}$$

where Δ ,b are the heights of air-gap and the waveguide respectively. γ is the propagation constant in z-direction.

4.3 Proposed HDC phase shifters

In this section two phase shifter structures using the high-dielectric materials with the idea similar to what has been shown in Figure 4.1 will be presented.

4.3.1 Air, High Dielectric, Air-Gap, Metal phase shifter

The first proposed phase shifter is similar to what is shown in Figure 4.1, but without bounding it in the x-direction. Therefore, the variation in x-direction is neglected. Furthermore, the top metal does not exist. The structure is shown in Figure 4.3

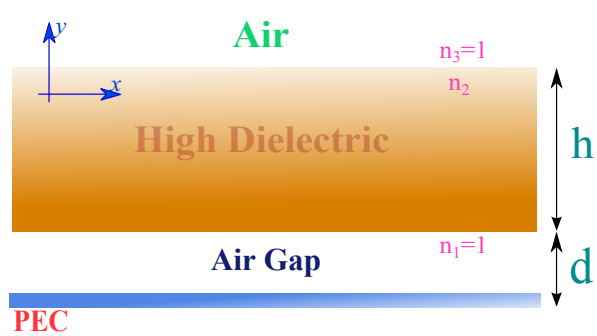

Figure 4.3: Proposed air, dielectric, air-gap, metal phase shifter

[1]Longitudinal Section Magnetic

The modal analysis needs to be done in order to derive the equations for finding the propagation constant β and all the components of electromagnetic fields inside the structure. It is assumed that the fields are exponentially decaying in region 1 and 3 (α_i is the decaying constant) and sinusoidal in region 2 (k_{y2} is the sinusoidal constant). For TM modes, the field components are E_z, E_y, H_x. According to the Helmholtz equation:

$$\left\{ \begin{array}{cc} I) & \alpha_1^2 - \beta^2 + k_0^2 n_1^2 = 0 \\ II) & -k_{y2}^2 - \beta^2 + k_0^2 n_2^2 = 0 \end{array} \right\} \rightarrow k_{y2}^2 + \alpha_1^2 = k_0^2(n_2^2 - n_1^2) = v^2 \tag{4.2}$$

The boundary conditions for dielectric-air interfaces are the continuity of E_z and H_x. E_z should be zero at $y = 0$ as well. Therefore, H_x can be written as:

$$H_x = \left\{ \begin{array}{cc} H_0 \frac{\cosh(\alpha_1 y)}{\cosh(\alpha_1 d)} e^{-j\beta z} & 0 < y < d \\ H_0 \frac{\sin(k_{y2} y) + B\ \cos(k_{y2} y)}{\sin(k_{y2} d) + B\ \cos(k_{y2} d)} e^{-j\beta z} & d < y < d + h \\ H_0 \frac{\sin(k_{y2}(d+h)) + B\ \cos(k_{y2}(d+h))}{\sin(k_{y2} d) + B\ \cos(k_{y2} d)} e^{-\alpha_1 (x-(d+h))} e^{-j\beta z} & y > d + h \end{array} \right\} \tag{4.3}$$

According to the Maxwell Equation:

$$\nabla \times H = j\omega\varepsilon E \rightarrow -\frac{\partial H_x}{\partial y} = j\omega\varepsilon E_z \tag{4.4}$$

and E_z can be written as:

$$E_z = \frac{-1}{j\omega\varepsilon_0} \left\{ \begin{array}{cc} H_0 \frac{\alpha_1}{n_1^2} \frac{\sinh(\alpha_1 y)}{\cosh(\alpha_1 d)} e^{-j\beta z} & 0 < y < d \\ H_0 \frac{k_{y2}}{n_2^2} \frac{\cos(k_{y2} y) - B\ \sin(k_{y2} y)}{\sin(k_{y2} d) + B\ \cos(k_{y2} d)} e^{-j\beta z} & d < y < d + h \\ H_0 \frac{-\alpha_1}{n_1^2} \frac{\sin(k_{y2}(d+h)) + B \cos(k_{y2}(d+h))}{\sin(k_{y2} d) + B\ \cos(k_{y2} d)} e^{-\alpha_1 (x-(d+h))} e^{-j\beta z} & y > d + h \end{array} \right\} \tag{4.5}$$

Applying the continuity of E_z on interfaces $y = d, d + h$ in Figure 4.3:

$$\frac{\alpha_1}{n_1^2} \tanh(\alpha_1 d) = \frac{k_{y2}}{n_2^2} \frac{\cos(k_{y2} d) - B\ \sin(k_{y2} d)}{\sin(k_{y2} d) + B\ \cos(k_{y2} d)} \tag{4.6}$$

$$\frac{-\alpha_1}{n_1^2} \left(\sin(k_{y2}(d+h)) + B \cos(k_{y2}(d+h))\right) = \frac{k_{y2}}{n_2^2} \left(\cos(k_{y2}(d+h)) - B\ \sin(k_{y2}(d+h))\right)$$

The equation (4.6) can be simplified into equation (4.7) by defining $B = tan(\gamma) \quad \gamma = (-\frac{\pi}{2}, \frac{\pi}{2})$:

$$\begin{aligned} \frac{\alpha_1}{n_1^2} \tanh(\alpha_1 d) &= \frac{k_{y2}}{n_2^2} \cot(\gamma + k_{y2} d) \\ \frac{-\alpha_1}{n_1^2} &= \frac{k_{y2}}{n_2^2} \cot(\gamma + k_{y2}(d+h)) \end{aligned} \tag{4.7}$$

Using what was derived in equation (4.2) and the equality

$$\cot(a-b) = \frac{\cot(a) - \cot(b) + 1}{\cot(b) - \cot(a)}$$

the characteristic equation for finding α_1 is obtained as:

$$\sqrt{v^2 - \alpha_1^2}\cot(\sqrt{v^2 - \alpha_1^2}h)n_2^2\alpha_1 n_1^2(1 + \tanh(\alpha_1 d)) + \alpha_1^2(n_1^4 + n_2^4\tanh(\alpha_1 d)) - v^2 n_1^4 = 0 \tag{4.8}$$

By solving the non-linear equation (4.8) (finding the zeros) and obtaining the values for α_1, the propagation constant β can be found from equation (4.2). After that, one can investigate the effect of the variation in d on the propagation constant β and the created phase shift.

Similar steps can be applied for the TE^z case, by starting from E_x, finding H_z and satisfying the boundary conditions to reach the characteristics equation for finding β:

$$(1 + \coth(\alpha_1 d))\alpha_1(\sqrt{v^2 - \alpha_1^2}\cot(\sqrt{v^2 - \alpha_1^2}h) + \alpha_1) - v^2 = 0 \tag{4.9}$$

Solving the characteristic equations (4.8) for $\varepsilon_r = 100$, $h = 300\mu m$ and d varying from $0 - 50\mu m$ at 30 GHz, real values for β for the TM mode are obtained. The proposed phase shifter has been also simulated in COMSOL Multi-Physics to verify the the obtained results for the propagation constant and the maximum phase shift. The field distribution of the simulated structure in COMSOL is shown in Figure 4.4

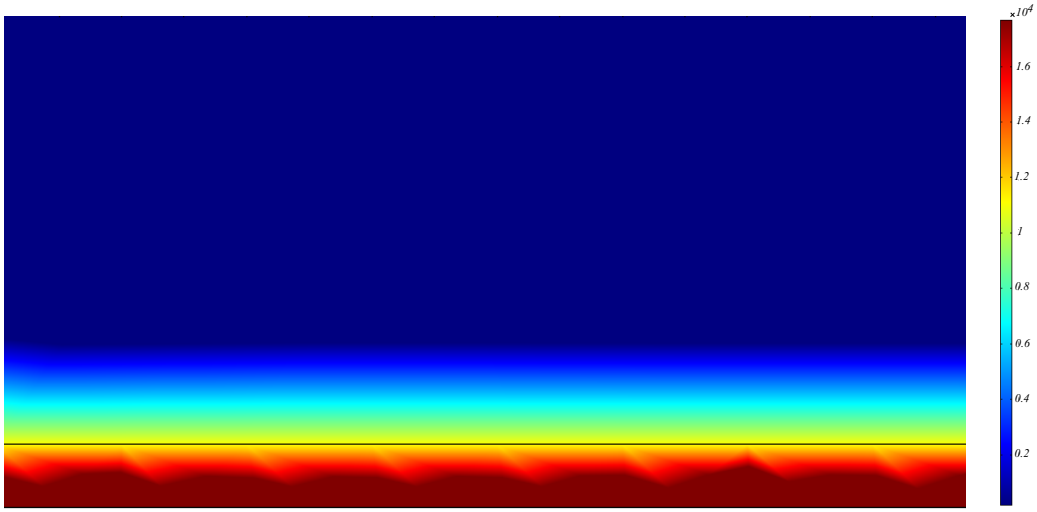

Figure 4.4: Norm of electric field for the simulated phase shifter structure in COMSOL software with $5\mu m$ air-gap

The result of COMSOL simulation with multi-step for air-gap size and analytical modal analysis is shown in Figure 4.5

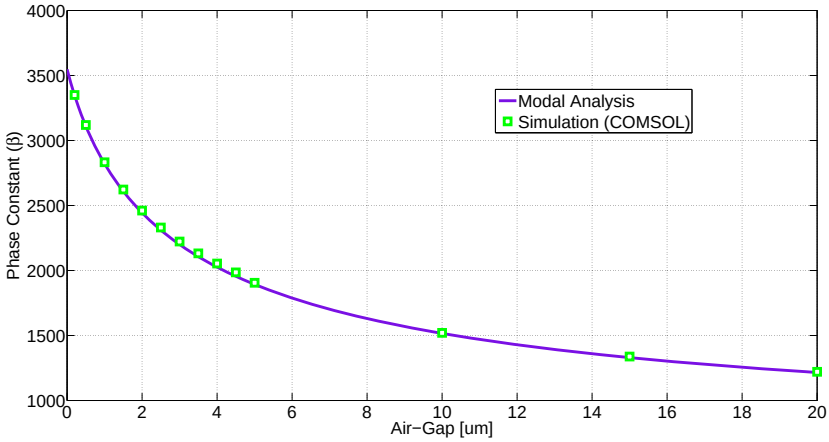

Figure 4.5: Modal analysis and simulation result of the propagation constant variation versus the air-gap size

As can be observed, the simulation results matches reasonably well with the modal analysis. In order to obtain the phase shift, the results need to be converted to phase by multiplying by the the length of the phase shifter ($3mm$ here) $\Delta\phi = \Delta\beta.\ell$.

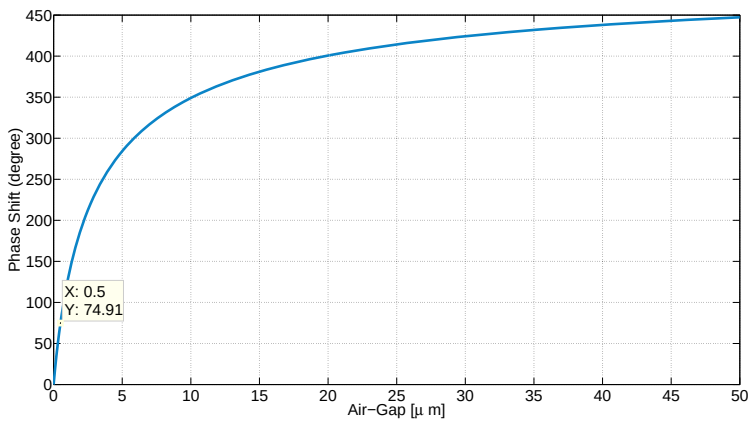

Figure 4.6: Phase shift versus the air-gap size for the proposed phase shifter shown in Figure 4.3

It is observed in Figure 4.6 that more than 400° phase shift can be created when the gap size varies from $0 - 50\mu m$. However, from a practical point of view, the smallest possible air-gap size is larger than $0.5\mu m$ limiting the maximum total phase shift to almost 375°.

In the TE^z mode, the variation of the propagation constant by changing the air-gap and subsequently the total phase shift is much smaller than that of the TM^z mode. This is because, in TM^z modes, the field is highly confined to the air-gap as shown in Figure 4.4, which is not true in TE^z case. Therefore, it is important to excite the TM^z mode to get the maximum phase shift. Another issue about the TE mode is that the variation of the propagation constant highly depends on the frequency and it may differ in a certain bandwidth, leading to phase-frequency error.

4.3.2 High Dielectric loaded CPW line phase shifter

The second proposed phase shifter is a CPW line on a high resistive silicon substrate loaded by a High dielectric constant ceramic. The air-gap between the CPW line and the high dielectric is varied to create the phase shift. This variation can be performed using PiezoElectric or MEMS. The proposed phase shifter is shown in Figure 4.7

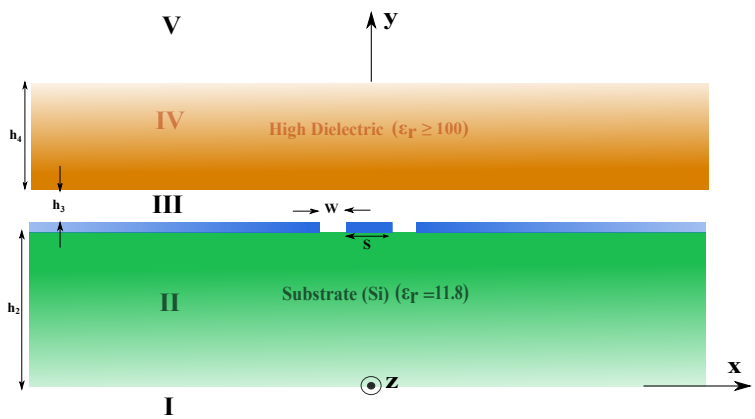

Figure 4.7: The proposed high dielectric loaded CPW line phase shifter

The dimensions in Figure 4.7 are listed in Table 4.1

Table 4.1: The parameters for the phase shifter shown in Figure 4.7

Parameters	S	W	h_4	h_2	h_3	$\varepsilon_{r,sub}$	$\varepsilon_{r,dil}$
Value (mm)	0.05	0.035	0.3	0.5	$0-50\mu m$	11.8	100

By changing the air-gap between the CPW line and the high dielectric, the $\varepsilon_{r,eff}$ of the structure will vary, resulting in the change in the propagation constant β and creating the phase shift. Analyzing the effect of variation in the gap is not as simple as that of the proposed structure in Figure 4.3, since the propagation mode in CPW line structure is generally the hybrid of TE and TM modes.

Two general analytical methods are used for analyzing the propagation constant and its variation for a multi-layer CPW line structure as illustrated in Figure 4.7: Spectral domain modal analysis and/or the conformal mapping technique. Here, these two methods will be utilized to determine the phase shift for the structure shown in Figure 4.7.

Spectral Domain Modal Analysis

In spectral domain modal analysis, the fields are transformed in the spectral domain of x (α) to an infinite sum of the plane waves propagating in the x direction as in

$$\phi(\alpha) = \int_{-\infty}^{+\infty} \phi(x) e^{i\alpha x} dx \tag{4.10}$$

In this analysis it is assumed that the thickness of metal is negligible with respect to other layers' thicknesses. Decomposition of the fields into TE^y and TM^y expressions by assuming that $\tilde{\psi}^h$ and $\tilde{\psi}^e$ are the spectral domain scalar potentials for TE^y and TM^y modes, respectively, results in the following expression for the fields [88].

$$\begin{array}{ll} \tilde{E}_x = \frac{-\alpha}{\omega\varepsilon}\frac{\partial\tilde{\psi}^e}{\partial y} - j\beta\tilde{\psi}^h & \tilde{H}_x = j\beta\tilde{\psi}^e - \frac{\alpha}{\omega\mu}\frac{\partial\tilde{\psi}^h}{\partial y} \\ \tilde{E}_y = \frac{1}{j\omega\varepsilon}\left(\frac{\partial^2}{\partial y^2} + k^2\right)\tilde{\psi}^e & \tilde{H}_y = \frac{1}{j\omega\mu}\left(\frac{\partial^2}{\partial y^2} + k^2\right)\tilde{\psi}^h \\ \tilde{E}_z = \frac{-\beta}{\omega\varepsilon}\frac{\partial\tilde{\psi}^e}{\partial y} - j\alpha\tilde{\psi}^h & \tilde{H}_z = -j\alpha\tilde{\psi}^e - \frac{\beta}{\omega\mu}\frac{\partial\tilde{\psi}^h}{\partial y} \end{array} \tag{4.11}$$

where $k^{=}\omega^2\mu\varepsilon$ and ε and μ are the permittivity and permeability in each medium. The scalar potentials satisfy in the spectral domain Helmholtz equation:

$$\left(k^2 - \alpha^2 - \beta^2 + \frac{\partial^2}{\partial y^2}\right)\tilde{\psi} = 0 \tag{4.12}$$

By writing the general solution for the Helmholtz equation in regions I-V, the following equations will be obtained:

$$I) \begin{array}{ll} \tilde{\psi}_I^e = & A_{1e}e^{\gamma_1 y} \\ \tilde{\psi}_I^h = & A_{1h}e^{\gamma_1 y} \end{array} \tag{4.13}$$

$$II) \begin{array}{ll} \tilde{\psi}_{II}^e = & A_{2e}\sinh(\gamma_2 y) + B_{2e}\cosh(\gamma_2 y) \\ \tilde{\psi}_{II}^h = & A_{2h}\sinh(\gamma_2 y) + B_{2h}\cosh(\gamma_2 y) \end{array} \tag{4.14}$$

$$III) \begin{array}{ll} \tilde{\psi}_{III}^e = & A_{3e}\sinh(\gamma_3 y) + B_{3e}\cosh(\gamma_3 y) \\ \tilde{\psi}_{III}^h = & A_{3h}\sinh(\gamma_3 y) + B_{3h}\cosh(\gamma_3 y) \end{array} \tag{4.15}$$

$$IV) \begin{array}{ll} \tilde{\psi}_{IV}^e = & A_{4e}\sinh(\gamma_4 y) + B_{4e}\cosh(\gamma_4 y) \\ \tilde{\psi}_{IV}^h = & A_{4h}\sinh(\gamma_4 y) + B_{4h}\cosh(\gamma_4 y) \end{array} \tag{4.16}$$

$$V) \begin{array}{ll} \tilde{\psi}_V^e = & A_{5e}e^{-\gamma_5(y-h_2-h_3-h_4)} \\ \tilde{\psi}_V^h = & A_{5h}e^{-\gamma_5(y-h_2-h_3-h_4)} \end{array} \tag{4.17}$$

where $\gamma_i^2 = \alpha^2 + \beta^2 - k_i^2$. In order to find the 16 unknown coefficients in equation (4.13), the boundary conditions, which are the continuity of tangential electric and magnetic fields, should be satisfied. For the interfaces $(I - II)$, $(III - IV)$ and $(IV - V)$ in Figure 4.7 the boundary conditions are:

$$\begin{aligned} \tilde{E}_{x,i} &= \tilde{E}_{x,i+1} \qquad & \tilde{H}_{x,i} &= \tilde{H}_{x,i+1} \\ \tilde{E}_{z,i} &= \tilde{E}_{z,i+1} \qquad & \tilde{H}_{z,i} &= \tilde{H}_{z,i+1} \end{aligned} \tag{4.18}$$

For the interface $(II - III)$, the boundary conditions can be written as:

$$\begin{aligned} \tilde{E}_{x,2} &= \tilde{E}_{x,3} \qquad & \tilde{H}_{x,3} - \tilde{H}_{x,2} &= \tilde{J}_z \\ \tilde{E}_{z,2} &= \tilde{E}_{z,3} \qquad & \tilde{H}_{z,3} - \tilde{H}_{z,2} &= \tilde{J}_x \end{aligned} \tag{4.19}$$

where $\tilde{J}_x$ and $\tilde{J}_z$ are the surface current on the CPW line. By possessing 18 unknowns and 16 equations from (4.18), (4.19) for the boundary conditions, the unknowns can be derived in terms of $\tilde{J}_x$ and $\tilde{J}_z$. Using equation (4.11), $\tilde{E}_x$, $\tilde{E}_z$ are written as:

$$\begin{bmatrix} \tilde{E}_z \\ \tilde{E}_x \end{bmatrix} = \begin{bmatrix} Z_{zz} & Z_{zx} \\ Z_{xz} & Z_{xx} \end{bmatrix} \begin{bmatrix} \tilde{J}_z \\ \tilde{J}_x \end{bmatrix} \tag{4.20}$$

or

$$\begin{bmatrix} Y_{zz} & Y_{zx} \\ Y_{xz} & Y_{xx} \end{bmatrix} \begin{bmatrix} \tilde{E}_z \\ \tilde{E}_x \end{bmatrix} = \begin{bmatrix} \tilde{J}_z \\ \tilde{J}_x \end{bmatrix} \tag{4.21}$$

where elements of the Y matrix are functions of α, β, the heights and dielectric values of the layers. The Galerkin's method is applied to find the propagation constant [89]. The first step is to expand $\tilde{E}_x$ and $\tilde{E}_z$ in terms of the known basis functions which approximate the field distribution in the slots and satisfy the edge conditions for the CPW line in the x-domain.

$$\begin{aligned} \tilde{E}_x(\alpha) &= \sum_{m=1}^{N_x} c_m \tilde{e}_{xm}(\alpha) \\ \tilde{E}_z(\alpha) &= \sum_{m=1}^{N_z} d_m \tilde{e}_{zm}(\alpha) \end{aligned} \tag{4.22}$$

Taking the inner product from both sides of the equation, (4.21) leads to:

$$\int_\alpha \begin{bmatrix} \tilde{e}_{zk} Y_{zz} \sum_{m=1}^{N_z} \tilde{e}_{zm} & \tilde{e}_{zk} Y_{zx} \sum_{m=1}^{N_z} \tilde{e}_{xm} \\ \tilde{e}_{xk} Y_{xz} \sum_{m=1}^{N_z} \tilde{e}_{zm} & \tilde{e}_{xk} Y_{xx} \sum_{m=1}^{N_z} \tilde{e}_{xm} \end{bmatrix} \begin{bmatrix} d_m \\ c_m \end{bmatrix} = \int_\alpha \begin{bmatrix} \tilde{e}_{zk} \tilde{J}_z \\ \tilde{e}_{xk} \tilde{J}_x \end{bmatrix} = 0 \tag{4.23}$$

The right hand side of (4.23) is zero due to the Perceval's theorem:

$$\int_{-\infty}^{+\infty} \tilde{e}_{xk}\tilde{J}_x d\alpha = 2\pi \int_{-\infty}^{+\infty} e_{xk}J_x dx = 0 \tag{4.24}$$

because on the strips the tangential field e_{xk} or e_{zk} are zero and on the slots tangential current is zero. In order to have a non-trivial solution for the system of equations, the determinant of the matrix on the left-hand side of equation (4.23) should be zero, and therefore β can be found.

For integration in the α domain there may be some poles (singularities) in the determinant expression that should be handled. The integration is extended to the complex domain to avoid meeting these poles as shown in Figure 4.8

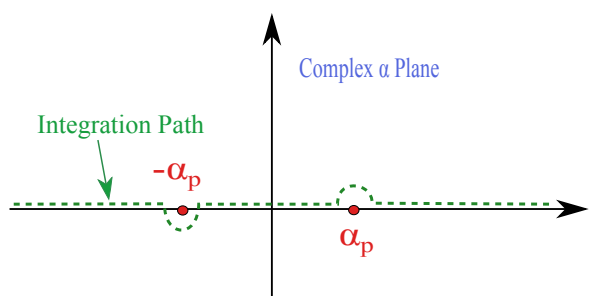

Figure 4.8: Integration path in the complex α plane

Conformal Mapping Technique

The other method which can be used to calculate the propagation constant in multilayer CPW line structures is the conformal mapping technique. In this method, the dominant mode of the structure is assumed to be Quasi-TEM and β is obtained by finding the effective dielectric constant for the structure. In order to find ε_{eff}, the total capacitance of CPW line is found.

$$\beta = k_0\sqrt{\varepsilon_{eff}}, \qquad \varepsilon_{eff} = \frac{C_{cpw}}{C_{air}} \tag{4.25}$$

In order to obtain C_{cpw} , the capacitance of different layers should be taken into consideration. Finally the total capacitance will be the sum of the all layer's capacitance since

they are parallel to each other. In the case of the structure shown in Figure 4.7:

$$C_{cpw} = C_{01} + C_2 + C_{03} + C_4 + C_{05} \tag{4.26}$$

$$C_{air} = C_{01} + C_{03} + C_{05} \tag{4.27}$$

where C_{0i} is the capacitance of the air regions. Calculation of C_{0i}s and C_2, C_4 requires specific transformations to convert them into parallel plate capacitance in another domain [90]. These transformations initially map each separated domain in the $x - y$ plane into the upper half space in $t - r$ plane (using R Transform) and subsequently map the upper half space in $t - r$ plane to a rectangular parallel plate capacitor in $u - v$ plane (using Christoffel-Schwartz transform, w)

$$R \leftarrow \cosh^2(\frac{\pi z_j}{2h_j}), \qquad z_j = x_j + jy_j \tag{4.28}$$

$$w \leftarrow F(\varphi, k) = \int_0^{\varphi} \frac{d\theta}{\sqrt{1 - k^2 \sin^2(\theta)}} \tag{4.29}$$

where h_j is the height of each layer. Through these transformations the CPW line capacitance will be converted into multiple rectangular parallel plate capacitors. The equation for calculating the capacitance in each region is:

$$C_j = \varepsilon_0 \varepsilon_r \frac{S_j}{G_j} \tag{4.30}$$

where S_j, G_j are the length and the gap between two plates transformed in the $u - v$ plane separately for each domain. The mapping performed for region II is shown in Figure 4.9

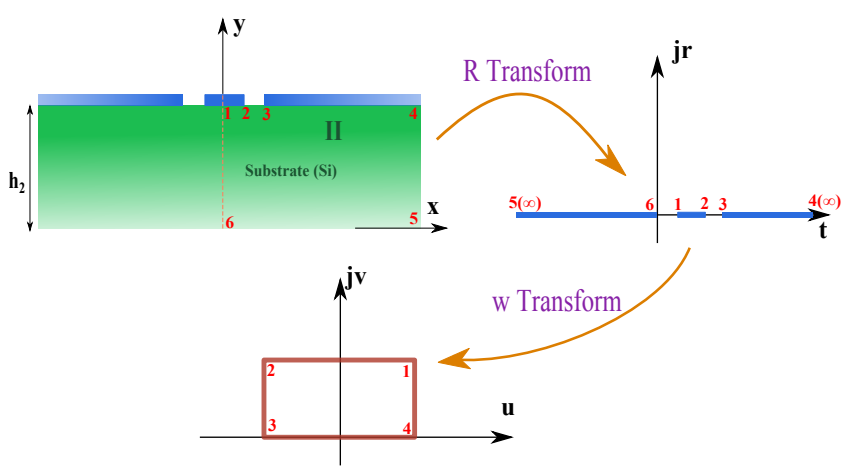

Figure 4.9: The mapping which has been performed for region II

Investigation of phase shift

Using the two techniques described in parts 4.3.2 and 4.3.2, the effect of the variations of h_3 on the propagation constant and subsequently the phase shift of the multilayer structure shown in Figure 4.7 will be discussed here. For the case of the phase shifter under consideration, the design parameters are shown in Table 4.1. h_1 , h_5 are assumed to be infinity and h_3 varies from $0 - 100\mu m$. The thickness of metals is ignored in this investigation.

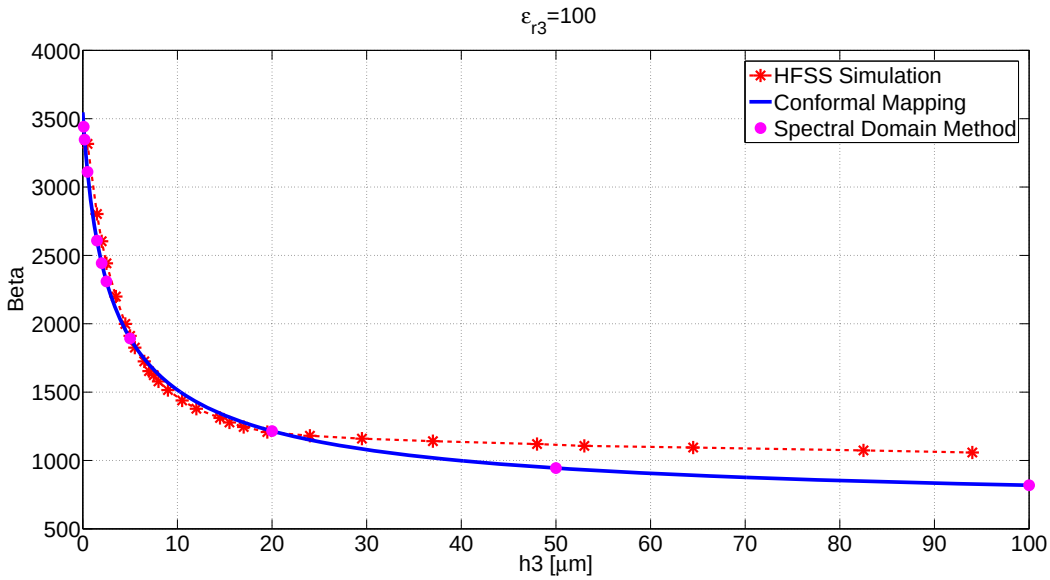

Figure 4.10: Propagation Constant versus h_3 calculated using the two methods at 30 GHz

Figure 4.10 shows the variation of the phase constant for the structure shown in Figure 4.7 using the dimensions listed in Table 4.1. As can be observed in Figure 4.10, the results obtained from the two analytical methods agree very well with each other. The final result has been also compared with HFSS simulation for the structure using the parametric sweep of h_3. It is observed that when the gap is not so large, there is a good agreement between the results obtained from the analytical methods and those acquired from a FEM solver like HFSS. For large values of h_3 there is a difference between the numerical and analytical results, which may have been originated from the numerical error. It is worth mentioning that the average computational time using the conformal mapping technique is 6 seconds while the HFSS full wave simulation average time for the same structure is 35 minutes on the same machine (Intel Core $i5$ and 8GB).

In practice, the air-gap between the high-dielectric and CPW line cannot be smaller than $1 - 3\mu m$ in the attached case. The maximum phase shift (phase difference between the attached case and no-loading condition) as ε_{r4} is varying from 50 to 200 is plotted in Figure 4.11

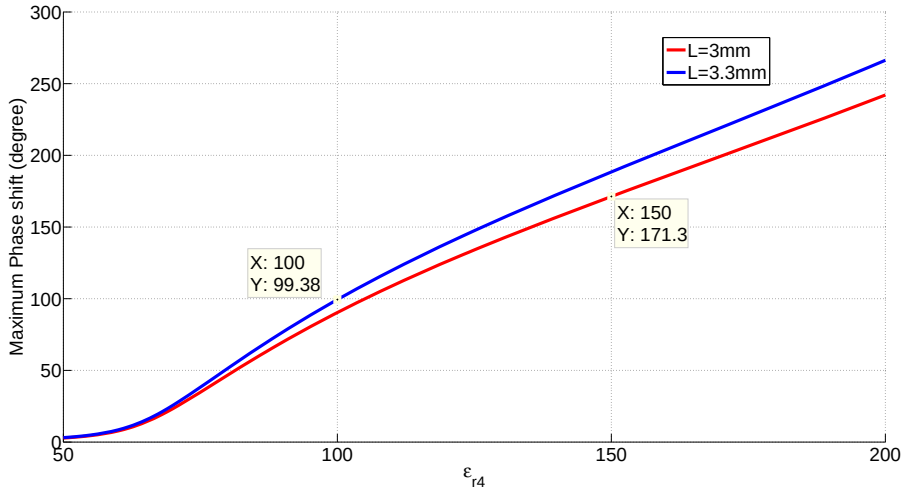

Figure 4.11: Maximum phase shift versus the dielectric constant at 30GHz, for the phase shifter shown in Figure 4.7

The device shown in Figure 4.7 has been fabricated and tested in [91]. Table 4.2 shows the results of measurements done in [91]

Table 4.2: Summary of Measurments at 30 GHz in [91]

Sample	ε_r	L_{dil}	Maximum Phase Shift	Insertion Loss
1	100	3.3mm	100°	0.7 dB
2	150	3mm	170°	1.1 dB

It is observed that the analytical modeling perfectly matches with the experimental results. One of the important advantage of this class of phase shifters with respect to others, as can been observed in Table 4.2, is the low and stable insertion loss throughout the frequency range. Although the calibration process is still an issue in the passive phase shifters, this kind of phase shifters can be considered as a candidate for passive phase shifters.

Chapter 5

Concluding Remarks

5.1 Summary

In this thesis, a comprehensive study on various types of miniaturized ka-band phase shifters in order to be utilized in a large commercial phased array antenna system has been presented. The advancement of tunable materials whose characteristics can be tuned by the applied voltage leads to the creation of a new class of microwave and mm-wave phase shifters.

The application of "Liquid Crystal", the tunable material which has found its usage in the industry for many years, has been investigated in chapter 2. It has been observed that, although these materials have low insertion loss in this range of frequency to be used in Ka-band phase shifter, they suffer from low tunability and low dielectric constant, which makes the transmission line phase shifters much larger than the wavelength. To overcome this issue, higher order Liquid crystal Filter-Type phase shifters have been proposed along with an analytical formulation to design them.

Ka-band phase shifters based on BST material, the other tunable material possessing larger dielectric constant and higher tunability compared to liquid crystals, have been studied in chapter 3. What BST films usually suffer from is the relatively high loss tangent which leads to a considerable amount of insertion loss. Conventional BST films also need high bias voltage to create sufficient tunability. Nevertheless, new fabrication techniques to process new compositions of BSTs combined with the utilization of thin BST layers have greatly reduced their insertion loss and the required bias voltage. All-pass BST based networks have been introduced and formulated in the final section of chapter 3 as compact lumped element phase shifters.

It has been investigated that the tangent loss of the mentioned tunable materials (LC and BST) depends heavily on the applied voltage. In order to have a low, and at the same time stable insertion loss, ka-band phase shifters based on high dielectric materials have been proposed in chapter 4. In this class of phase shifters, it has been tried to confine the electric fields in an air-gap between the high dielectric ceramic and the metal in the transmission line which results in smaller insertion loss. The analytic formulation for high dielectric constant phase shifters compared with simulation and measurement results have also been demonstrated in chapter 4.

5.2 Future Works

What was exhibited in this thesis was just a small portion among the various aspects of research in Ka-band phase shifters for satellite communications. In section 2.4.2 of chapter 2, the design methodology for the realization of a higher order filter-type phase shifter has been presented. Physical design of a compact high- order filter type phase shifter can be performed as a further step. The proof of concept for the phase shifter (simplified version shown in Figure 4.3) has been proposed in chapter 4. The actual physical realization (design, fabrication and measurement) of this phase shifter is another possible area of future research. Other configurations using high-dielectric low loss ceramics can investigated as phase shifters.

APPENDICES

Appendix A

The effect of filter-type phase shifters on phased array performance

The effects of filter-type phase shifters on phased array system performance will be discussed in this appendix. For a realistic evaluation of the effects of phase shifter's non-linear frequency response on the phased-array antenna systems, a particular Ka-band array system with optimal excitations, designed by the Taylor synthesis/optimization method [92], is chosen. The synthesized current excitations of the planar array are illustrated in Figure A.1a for 80×80 antenna elements with spacing of almost 0.5λ at 29.75 GHz [92]. In order to obtain practical excitation coefficients, the calculated coefficients have been quantized in 0.5 dB steps and the antenna elements with excitation coefficients values less than -10 dB have been removed as shown in Figure A.1b. Figure A.1b illustrates the corresponding gain pattern of the Tx planar array with a panel size of 40 cm $\times$40 cm in $\phi = 0°$ and $\phi = 90°$ planes [92].

Figure A.2 shows the gain patterns of the designed array, when the beam direction is electronically steered and positioned at 30°. As can be observed, the gain radiation patterns meet the standard side-lobe envelope. However, as expected, the peak gain decreases by 2 dB due to the element factor degradation and effective aperture area reduction at various beam positions. The resultant gain degradation causes the main beam broadening of 0.4° for 30° beam scanning angle.

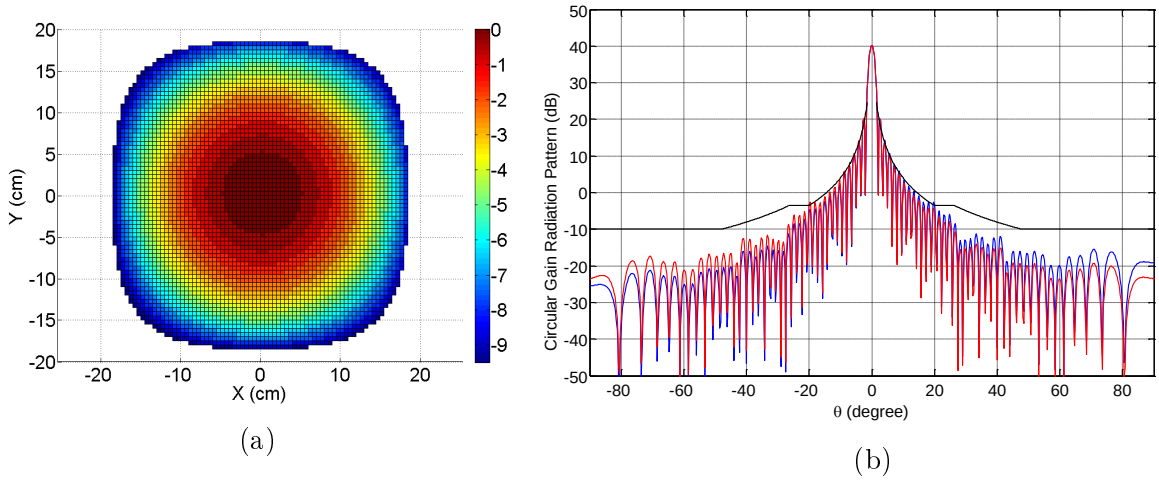

(a) (b)

Figure A.1: a) Quantized current coefficients of antenna elements, b) gain radiation pattern of Tx planar array [92]

For the beam steering angle of 30° shown in Figure A.2, analog phase shifters have been used. Consequently, it is possible to adjust the required phase shifting for each antenna element. The insertion loss variations of phase shifters can significantly affect the antenna gain and radiation pattern. However, it has been compensated for by using variable gain amplifiers (VGA) integrated with each phase shifter. As mentioned, the amplitude and

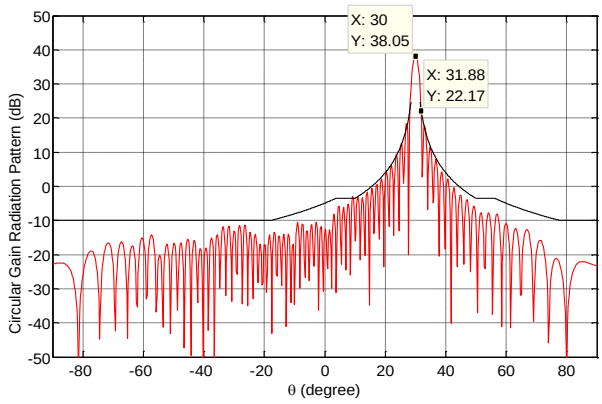

Figure A.2: Gain radiation patterns of the Tx phased array for beam position 30°

phase required for each antenna element have been adjusted to obtain the radiation pattern

satisfying the FCC mask [93]. However, the amplitude and phase adjustments are often performed only for the center frequency, without accurate examination of the phase-shift variation over the entire range of frequencies.

In Figure A.3, the phase shifter models outlined in figures 2.15 to 2.17 and Figure 3.13, plus the elliptical filter have been extended and detailed. Each curve corresponds to a particular voltage applied to the phase shifter structure. The relative phase shifts are plotted with respect to the phase response of the middle state:

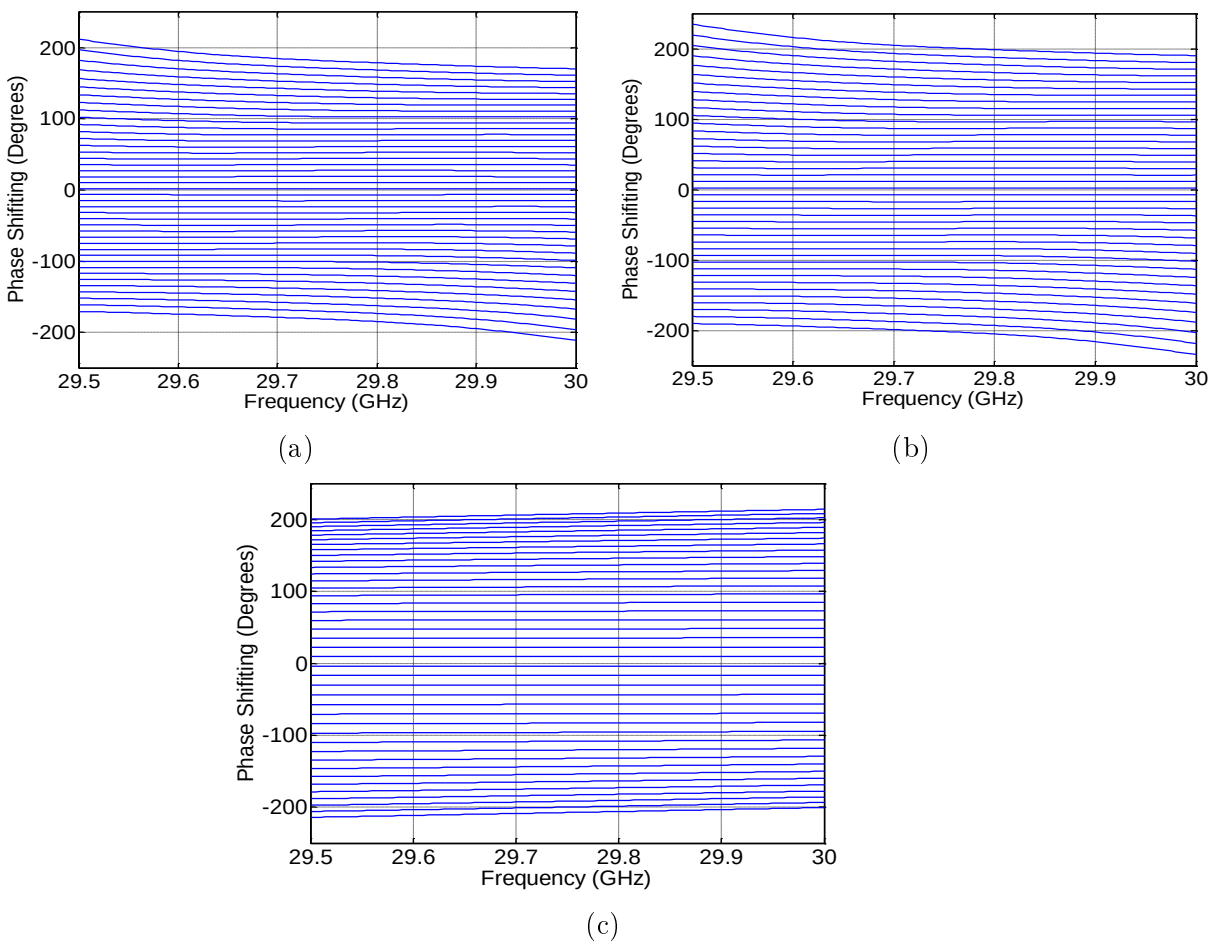

Figure A.3: The phase shifts of the three types of phase shifters versus frequency, a) Chebyshev, order= 5,$R.L$ = 10 dB, BW = 2GHz, and Q_u = 200, b) Elliptical, order= 6,$R.L$ = 10 dB, BW = 2GHz, and Q_u = 200, and c) 2nd order All-Pass filter $\sigma_b = 24$,$s_b = 26$

For a particular beam direction, the phase shift required for each antenna element is calculated and the corresponding voltage commands can be applied to each phase shifters to realize the phase shift at the center frequency. This will result in the same radiation patterns illustrated in Figure A.2 at 29.75 GHz. However, in reality the applied voltages provide the calculated (desired) phase shifts only at 29.75 GHz, and the phase shift at other frequencies is deviated from those of the ideal case at the center frequency.

As can be observed in Figure A.3, the maximum phase shift error occurs at the lowest and highest frequencies (29.5GHz and 30GHz). The gain radiation patterns at 29.5GHz, 29.75GHz, and 30GHz are obtained and presented in Figure A.4 , using the modeling presented and shown in Figure A.3.

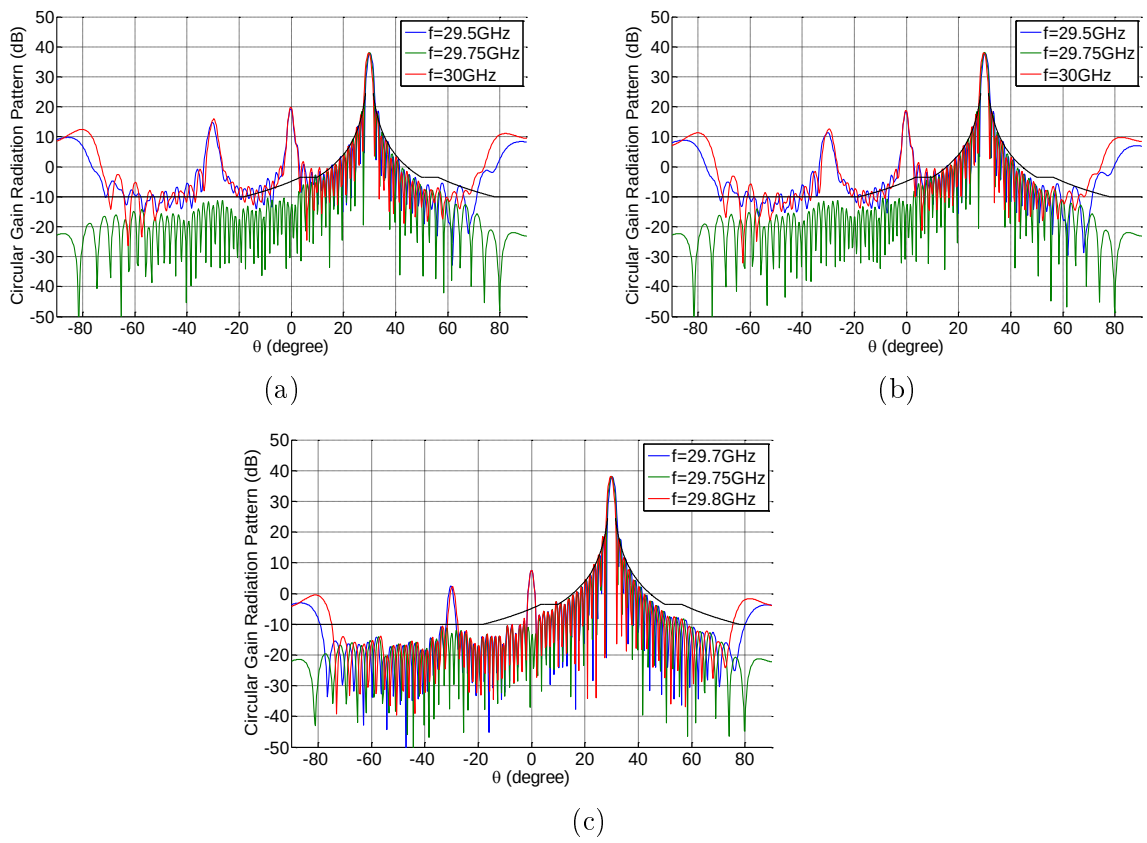

Figure A.4: Gain radiation pattern at $f = 29.5$, 29.75, and 30GHz for a) Chebyshev b) Elliptical C) All-Pass phase shifter when the scanning angle is 30°

Figure A.4 shows that the phase-frequency response non-linearity can significantly affect

the side lobes and cause critical violation of the radiation mask. Hence, once the applied voltages are adjusted for the center frequency, the relative phase shift errors at other frequencies have led to mask violation.

Comparing the radiation patterns due to different types of phase shifters, one can conclude that the mask violation is less critical in the case of 2nd order All-Pass phase shifters. This is due to the fact that All-Pass phase shifters can provide a linear phase-frequency response over a wider range of frequencies than band-pass networks.

A.1 Distortion due to the phase-frequency non-linearity of filter-type phase shifters

In addition to the mask violation, the phase-frequency non-linearity will result in the beam positioning errors. In Figure A.5, the angular region close to the main beam maximum of Figure A.4b has been expanded. As shown, the main beam deviates from 30°. This deviation angle is also frequency-dependent. Figure A.6 depicts the phased array gain versus frequency for various phase shifter types and different desired scanning angles.

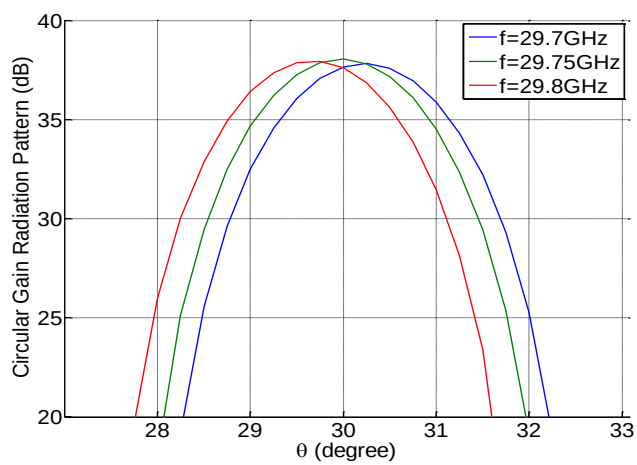

Figure A.5: Beam positioning error at f= 29.5, 29.75, and 30 GHz for the case of Elliptical phase shifter when the scanning angle is 30°

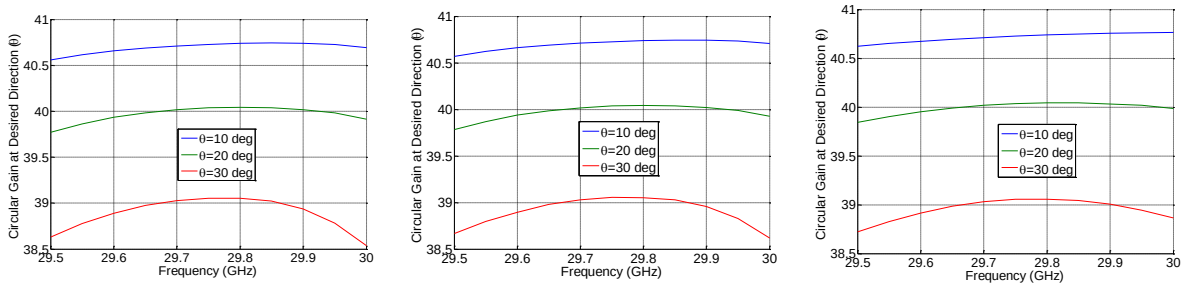

(a) (b) (c)

Figure A.6: Maximum Gain versus frequency for beam scanning angles of 10°, 20°, and 30° when using a) Chebyshev, b) Elliptical, and c) All-Pass phase shifters

As expected, the gain variations over the frequency band increases for larger scanning angles. Table A.1 presents the maximum gain variations for various filter types and different beam scanning angles.

Table A.1: Maximum gain variation over the frequency for Chebyshev, Elliptical, and All-Pass phase shifters for various beam scanning angles

Scanning Angle	Chebyshev	Elliptical	All-Pass
10°	0.18 dB	0.17dB	0.14 dB
20°	0.27 dB	0.26dB	0.20 dB
30°	0.51 dB	0.43dB	0.34 dB

References

[1] Constantine A Balanis. *Antenna theory: analysis and design.* John Wiley & Sons, 2012.

[2] Danial Ehyaie. *Novel Approaches to the Design of Phased Array Antennas.* PhD thesis, The University of Michigan, 2011.

[3] Eli Brookner. Phased-array radars: Past, astounding breakthroughs and future trends. *Microwave Journal*, 51(1), 2008.

[4] Joseph Michael. Phased array based radar system for vehicular collision avoidance, November 14 1995. US Patent 5,467,072.

[5] Martin Schneider. Automotive radar–status and trends. In *German microwave conference*, pages 144–147, 2005.

[6] Josef Wenger. Automotive radar-status and perspectives. In *Compound Semiconductor Integrated Circuit Symposium, 2005. CSIC'05. IEEE*, pages 4–pp. IEEE, 2005.

[7] Willie D Jones. Keeping cars from crashing. *Spectrum, IEEE*, 38(9):40–45, 2001.

[8] Theodore S Rappaport, James N Murdock, and Felix Gutierrez. State of the art in 60-ghz integrated circuits and systems for wireless communications. *Proceedings of the IEEE*, 99(8):1390–1436, 2011.

[9] Emanuel Cohen, Mark Ruberto, Moshik Cohen, Ofir Degani, Shmuel Ravid, and Dan Ritter. A cmos bidirectional 32-element phased-array transceiver at 60ghz with ltcc antenna. In *Radio Frequency Integrated Circuits Symposium (RFIC), 2012 IEEE*, pages 439–442. IEEE, 2012.

[10] Arun Natarajan, Scott K Reynolds, Ming-Da Tsai, Sean T Nicolson, J-HC Zhan, Dong Gun Kam, Duixian Liu, Y-LO Huang, Alberto Valdes-Garcia, and Brian A Floyd. A fully-integrated 16-element phased-array receiver in sige bicmos for 60-ghz communications. *Solid-State Circuits, IEEE Journal of*, 46(5):1059–1075, 2011.

[11] Alberto Valdes-Garcia, Sean Nicolson, Jie-Wei Lai, Arun Natarajan, Ping-Yu Chen, Scott Reynolds, J-HC Zhan, and Brian Floyd. A sige bicmos 16-element phased-array transmitter for 60ghz communications. In *Solid-State Circuits Conference Digest of Technical Papers (ISSCC), 2010 IEEE International*, pages 218–219. IEEE, 2010.

[12] Scott K Reynolds, Arun S Natarajan, Ming-Da Tsai, Sean Nicolson, J-HC Zhan, Duixian Liu, Dong G Kam, Oscar Huang, Alberto Valdes-Garcia, and Brian A Floyd. A 16-element phased-array receiver ic for 60-ghz communications in sige bicmos. In *Radio Frequency Integrated Circuits Symposium (RFIC), 2010 IEEE*, pages 461–464. IEEE, 2010.

[13] Evanguelos Xylinas, David R Yates, Raphaële Renard-Penna, Elise Seringe, Jean-Claude Bousquet, Eva Comperat, Marc-Olivier Bitker, Philippe Grenier, and Morgan Rouprêt. Role of pelvic phased array magnetic resonance imaging in staging of prostate cancer specifically in patients diagnosed with clinically locally advanced tumours by digital rectal examination. *World journal of urology*, 31(4):881–886, 2013.

[14] Hernan I Vargas, William C Dooley, Robert A Gardner, Katherine D Gonzalez, Rose Venegas, Sylvia H Heywang-Kobrunner, and Alan J Fenn. Focused microwave phased array thermotherapy for ablation of early-stage breast cancer: results of thermal dose escalation. *Annals of surgical oncology*, 11(2):139–146, 2004.

[15] Arnauld Villers, Philippe Puech, Damien Mouton, Xavier Leroy, Charles Ballereau, and Laurent Lemaitre. Dynamic contrast enhanced, pelvic phased array magnetic resonance imaging of localized prostate cancer for predicting tumor volume: correlation with radical prostatectomy findings. *The Journal of urology*, 176(6):2432–2437, 2006.

[16] J.M. Howell. Limited scan antennas. In *Antennas and Propagation Society International Symposium, 1974*, volume 12, pages 117–120, Jun 1974.

[17] Abbas Abbaspour-Tamijani and Kamal Sarabandi. An affordable millimeter-wave beam-steerable antenna using interleaved planar subarrays. *Antennas and Propagation, IEEE Transactions on*, 51(9):2193–2202, 2003.

[18] F Reggia and EG Spencer. A new technique in ferrite phase shifting for beam scanning of microwave antennas. *Proceedings of the IRE*, 45(11):1510–1517, 1957.

[19] Shiban K Koul and Bharathi Bhat. *Microwave and millimeter wave phase shifters: dielectric and ferrite phase shifters*. Artech House, 1991.

[20] William WG Hui, Jodie M Bell, Magdy F Iskander, and JJ Lee. Low-cost microstrip-line-based ferrite phase shifter design for phased array antenna applications. *Antennas and Wireless Propagation Letters, IEEE*, 6:86–89, 2007.

[21] AB Ustinov, G Srinivasan, and BA Kalinikos. Ferrite-ferroelectric hybrid wave phase shifters. *Applied physics letters*, 90(3):031913, 2007.

[22] Paul B Ruffin, James C Holt, James H Mullins, Tracy Hudson, and Janice Rock. Mems-based phased arrays for army applications. In *The 14th International Symposium on: Smart Structures and Materials & Nondestructive Evaluation and Health Monitoring*, pages 652802–652802. International Society for Optics and Photonics, 2007.

[23] EA Nenasheva and NF Kartenko. High dielectric constant microwave ceramics. *Journal of the European Ceramic Society*, 21(15):2697–2701, 2001.

[24] Onur Hamza Karabey, Felix Goelden, Alexander Gaebler, and Rolf Jakoby. Precise broadband microwave material characterization of liquids. In *Microwave Conference (EuMC), 2010 European*, pages 1591–1594. IEEE, 2010.

[25] Harry J Coles and Mikhail N Pivnenko. Liquid crystal âĂŸblue phasesâĂŹ with a wide temperature range. *Nature*, 436(7053):997–1000, 2005.

[26] Shin-Tson Wu and Deng-Ke Yang. *Fundamentals of liquid crystal devices*. John Wiley & Sons, 2006.

[27] Peter J Wojtowicz, Ping Sheng, and EB Priestley. *Introduction to liquid crystals*. Springer, 1975.

[28] Onur Hamza Karabey, Saygin Bildik, Carsten Fritzsch, Sebastian Strunck, Alexander Gaebler, Rolf Jakoby, and Atsutaka Manabe. Liquid crystal based rekonfigurable antenna arrays. In *Proceedings of the 32nd ESA Antenna workshop*, 2010.

[29] Stefan Mueller, Andreas Penirschke, Christian Damm, Patrick Scheele, Michael Wittek, Carsten Weil, and Rolf Jakoby. Broad-band microwave characterization of liquid crystals using a temperature-controlled coaxial transmission line. *Microwave Theory and Techniques, IEEE Transactions on*, 53(6):1937–1945, 2005.

[30] Kazuaki Tarumi, Ulrich Finkenzeller, and Brigitte Schuler. Dynamic behaviour of twisted nematic liquid crystals. *Japanese journal of applied physics*, 31(part 1):2829–2836, 1992.

[31] Andreas Penirschke, Stefan Muller, Patrick Scheele, Carsten Weil, Michael Wittek, Christian Hock, and Rolf Jakoby. Cavity perturbation method for characterization of liquid crystals up to 35 ghz. In *Microwave Conference, 2004. 34th European*, volume 2, pages 545–548. IEEE, 2004.

[32] Atsutaka Manabe. Liquid crystals for microwave applications. In *SPIE OPTO*, pages 86420S–86420S. International Society for Optics and Photonics, 2013.

[33] Stefan Mueller, Christoph Felber, Patrick Scheele, Michael Wittek, Christian Hock, and Rolf Jakoby. Passive tunable liquid crystal finline phase shifter for millimeter waves. In *Microwave Conference, 2005 European*, volume 1, pages 4–pp. IEEE, 2005.

[34] F Goelden, A Gaebler, S Mueller, A Lapanik, W Haase, and R Jakoby. Liquid-crystal varactors with fast switching times for microwave applications. *Electronics letters*, 44(7):480–481, 2008.

[35] Noham Martin, Paul Laurent, Gaetan Prigent, Philippe Gelin, and Fabrice Huret. Improvement of an inverted microstrip line-based microwave tunable phase-shifter using liquid crystal. In *Microwave Conference, 2003. 33rd European*, pages 1417–1420. IEEE, 2003.

[36] Stefan Muller, Patrick Scheele, Carsten Weil, Michael Wittek, Christian Hock, and Rolf Jakoby. Tunable passive phase shifter for microwave applications using highly anisotropic liquid crystals. In *Microwave Symposium Digest, 2004 IEEE MTT-S International*, volume 2, pages 1153–1156. IEEE, 2004.

[37] F Goelden, A Gaebler, M Goebel, A Manabe, S Mueller, and R Jakoby. Tunable liquid crystal phase shifter for microwave frequencies. *Electronics letters*, 45(13):686–687, 2009.

[38] S Abadei, A Deleniv, and S Gevorgian. Filter-phase shifters based on thin film ferroelectric varactors. In *Microwave Conference, 2004. 34th European*, volume 3, pages 1493–1496. IEEE, 2004.

[39] A Deleniv, S Abadei, and S Gevorgian. Tunable ferroelectric filter-phase shifter. In *Microwave Symposium Digest, 2003 IEEE MTT-S International*, volume 2, pages 1267–1270. IEEE, 2003.

[40] Daisuke Morikawa, Hiroyuki Deguchi, Mikio Tsuji, and Hiroshi Shigesawa. A microstrip-line phase shifter constructed by a tunable filter. *Electronics and Communications in Japan (Part II: Electronics)*, 90(2):25–32, 2007.

[41] Mani Yazdanpanahi and Dariush Mirshekar-Syahkal. Millimeter-wave liquid-crystal-based tunable bandpass filter. In *Radio and Wireless Symposium (RWS), 2012 IEEE*, pages 139–142. IEEE, 2012.

[42] MK Mohd Salleh, Gaëtan Prigent, Olivier Pigaglio, and Raymond Crampagne. Quarter-wavelength side-coupled ring resonator for bandpass filters. *Microwave Theory and Techniques, IEEE transactions on*, 56(1):156–162, 2008.

[43] Alexander Moessinger, Carsten Fritzsch, Saygin Bildik, and Rolf Jakoby. Compact tunable ka-band phase shifter based on liquid crystals. In *Microwave Symposium Digest (MTT), 2010 IEEE MTT-S International*, pages 1020–1023. IEEE, 2010.

[44] Richard J Cameron, Chandra M Kudsia, and Raafat R Mansour. *Microwave filters for communication systems*. Wiley-Interscience, 2007.

[45] George L Matthaei, Leo Young, and EMT Jones. *Microwave filters, impedance-matching networks, and coupling structures*, volume 5. McGraw-Hill New York, 1964.

[46] Theodore S Saad, Robert C Hansen, and Gershon J Wheeler. *Microwave engineers' handbook*, volume 1. Artech House, 1971.

[47] Chunlin Fu, Wei Cai, Hongwei Chen, Shucheng Feng, Fusheng Pan, and Chuanren Yang. Voltage tunable ba0.6sr0.4tio3 thin films and coplanar phase shifters. *Thin Solid Films*, 516(16):5258–5261, 2008.

[48] Don Parker and David C Zimmermann. Phased arrays-part i: Theory and architectures. *IEEE transactions on microwave theory and techniques*, 50(3):678–687, 2002.

[49] Gabriel M Rebeiz, Guan-Leng Tan, and Joseph S Hayden. Rf mems phase shifters: design and applications. *Microwave Magazine, IEEE*, 3(2):72–81, 2002.

[50] Antonio Feteira, Derek C Sinclair, Ian M Reaney, Yoshitaka Somiya, and Michael T Lanagan. Batio3-based ceramics for tunable microwave applications. *Journal of the American Ceramic Society*, 87(6):1082–1087, 2004.

[51] LN Gao, SN Song, JW Zhai, and X Yao. Improvement of dielectric properties of graded co-doped (ba0. 7sr0. 3) tio3 thin films fabricated by sol–gel method. *Ferroelectrics*, 357(1):142–147, 2007.

[52] Jiangying Wang, Jingji Zhang, and Xi Yao. Dielectric properties of mg-doped ba0.6sr0.4tio3 ceramics prepared by using sol–gel derived powders. *Journal of Alloys and Compounds*, 505(2):783–786, 2010.

[53] G Vélu, JC Carru, E Cattan, D Remiens, X Melique, and D Lippens. Deposition of ferroelectric bst thin films by sol gel route in view of electronic applications. *Ferroelectrics*, 288(1):59–69, 2003.

[54] Franco De Flaviis, NG Alexopoulos, and Oscar M Stafsudd. Planar microwave integrated phase-shifter design with high purity ferroelectric material. *Microwave Theory and Techniques, IEEE Transactions on*, 45(6):963–969, 1997.

[55] Nadia K Pervez. *Investigation of loss mechanisms in thin film barium strontium titanate capacitors*. PhD thesis, UNIVERSITY OF CALIFORNIA, 2006.

[56] Jiwei Lu and Susanne Stemmer. Low-loss, tunable bismuth zinc niobate films deposited by rf magnetron sputtering. *Applied Physics Letters*, 83(12):2411–2413, 2003.

[57] Wei Ren, Susan Trolier-McKinstry, Clive A Randall, and Thomas R Shrout. Bismuth zinc niobate pyrochlore dielectric thin films for capacitive applications. *Journal of applied physics*, 89(1):767–774, 2001.

[58] Young Pyo Hong, Seok Ha, Ha Yong Lee, Young Cheol Lee, Kyung Hyun Ko, Dong-Wan Kim, Hee Bum Hong, and Kug Sun Hong. Voltage tunable dielectric properties of rf sputtered bi2o3-zno-nb2o5 pyrochlore thin films. *Thin Solid Films*, 419(1):183–188, 2002.

[59] Alexander K Tagantsev, Jiwei Lu, and Susanne Stemmer. Temperature dependence of the dielectric tunability of pyrochlore bismuth zinc niobate thin films. *Applied Physics Letters*, 86(3):032901, 2005.

[60] EA Nenasheva, NF Kartenko, IM Gaidamaka, ON Trubitsyna, SS Redozubov, AI Dedyk, and AD Kanareykin. Low loss microwave ferroelectric ceramics for high power tunable devices. *Journal of the European Ceramic Society*, 30(2):395–400, 2010.

[61] Spartak S Gevorgian, EF Carlsson, S Rudner, U Helmersson, EL Kollberg, E Wikborg, and OG Vendik. Hts/ferroelectric devices for microwave applications. *Applied Superconductivity, IEEE Transactions on*, 7(2):2458–2461, 1997.

[62] A Kozyrev, A Ivanov, V Keis, M Khazov, V Osadchy, T Samoilova, O Soldatenkov, A Pavlov, G Koepf, C Mueller, et al. Ferroelectric films: Nonlinear properties and

applications in microwave devices. In *Microwave Symposium Digest, 1998 IEEE MTT-S International*, volume 2, pages 985–988. IEEE, 1998.

[63] FW Van Keuls, RR Romanofsky, ND Varaljay, FA Miranda, CL Canedy, S Aggarwal, T Venkatesan, and R Ramesh. A ku-band gold/baxsr1-xtio3/laalo3 conductor/thin-film ferroelectric microstrip line phase shifter for room-temperature communications applications. *Microwave and Optical Technology Letters*, 20(1):53–56, 1999.

[64] Gabriel Velu, Karine Blary, Ludovic Burgnies, Aurélien Marteau, Grégory Houzet, Didier Lippens, and J-C Carru. A 360 bst phase shifter with moderate bias voltage at 30 ghz. *Microwave Theory and Techniques, IEEE Transactions on*, 55(2):438–444, 2007.

[65] Ki-Byoung Kim, Tae-Soon Yun, Hyun-Suk Kim, Il-Doo Kim, Ho-Gi Kim, and Jong-Chul Lee. Coplanar ferroelectric phase shifter on silicon substrate with tio 2 buffer layer. In *Microwave Conference, 2005 European*, volume 1, pages 4–pp. IEEE, 2005.

[66] Erich G Erker, Amit S Nagra, Yu Liu, Padmini Periaswamy, Troy R Taylor, James Speck, and Robert A York. Monolithic ka-band phase shifter using voltage tunable basrtio 3 parallel plate capacitors. *Microwave and Guided Wave Letters, IEEE*, 10(1):10–12, 2000.

[67] G Vélu, K Blary, L Burgnies, JC Carru, E Delos, A Marteau, and Didier Lippens. A 310/3.6-db k-band phaseshifter using paraelectric bst thin films. *IEEE microwave and wireless components letters*, 16(2):87–89, 2006.

[68] Mohsen Sazegar, Arshad Mehmood, Yuliang Zheng, Holger Maune, Xianghui Zhou, Joachim Binder, and Rolf Jakoby. Compact tunable loaded line phase shifter based on screen printed bst thick film. In *Microwave Conference (GeMIC), 2011 German*, pages 1–4. IEEE, 2011.

[69] J.L. Serraiocco. *Compact Phase Shifter Design Using Barium Strontium Titanate Thin-film Varactors*. University of California, Santa Barbara, 2003.

[70] Andre Giere, Patrick Scheele, Yuliang Zheng, and Rolf Jakoby. Characterization of the field-dependent permittivity of nonlinear ferroelectric films using tunable coplanar lines. *Microwave and Wireless Components Letters, IEEE*, 17(6):442–444, 2007.

[71] Amit S Nagra and Robert A York. Distributed analog phase shifters with low insertion loss. *Microwave Theory and Techniques, IEEE Transactions on*, 47(9):1705–1711, 1999.

[72] Christian Damm, M Schussler, Marius Oertel, and Rolf Jakoby. Compact tunable periodically lc loaded microstrip line for phase shifting applications. In *Microwave Symposium Digest, 2005 IEEE MTT-S International*, pages 4–pp. IEEE, 2005.

[73] George V Eleftheriades and Keith G Balmain. *Negative-refraction metamaterials: fundamental principles and applications*. John Wiley & Sons, 2005.

[74] Mohsen Sazegar, Yuliang Zheng, Holger Maune, Xianghui Zhou, Christian Damm, and Rolf Jakoby. Compact artificial line phase shifter on ferroelectric thick-film ceramics. In *Microwave Symposium Digest (MTT), 2010 IEEE MTT-S International*, pages 860–863. IEEE, 2010.

[75] Mohsen Sazegar, Yuliang Zheng, Holger Maune, Christian Damm, Xianghui Zhou, Joachim Binder, and Rolf Jakoby. Low-cost phased-array antenna using compact tunable phase shifters based on ferroelectric ceramics. *Microwave Theory and Techniques, IEEE Transactions on*, 59(5):1265–1273, 2011.

[76] B York. Tunable dielectrics for rf circuits. *Multifunctional adaptive microwave circuits and systems*, pages 159–207, 2009.

[77] Jia-Shen G Hong and Michael J Lancaster. *Microstrip filters for RF/microwave applications*, volume 167. John Wiley & Sons, 2004.

[78] Dongsu Kim, Yoonsu Choi, Minsik Ahn, Mark G Allen, J Stevenson Kenney, and Pat Marry. 2.4 ghz continuously variable ferroelectric phase shifters using all-pass networks. *Microwave and Wireless Components Letters, IEEE*, 13(10):434–436, 2003.

[79] Dongsu Kim, Sang-Soo Je, J Stevenson Kenney, and P Marry. Design of ferroelectric phase shifters for minimum performance variation over temperature. In *Microwave Symposium Digest, 2004 IEEE MTT-S International*, volume 1, pages 257–260. IEEE, 2004.

[80] L-YV Chen, Roger Forse, Albert H Cardona, TC Watson, and R York. Compact analog phase shifters using thin-film (ba, sr) tio3 varactors. In *Microwave Symposium, 2007. IEEE/MTT-S International*, pages 667–670. IEEE, 2007.

[81] Nan Ni and Albert Humirang Cardona. Ku-band analog phase shifters using individually designed all-pass networks with bst tunable capacitors. In *Radio and Wireless Symposium (RWS), 2011 IEEE*, pages 126–129. IEEE, 2011.

[82] David Viveiros Jr, Denise Consonni, and Adam K Jastrzebski. A tunable all-pass mmic active phase shifter. *Microwave Theory and Techniques, IEEE Transactions on*, 50(8):1885–1889, 2002.

[83] RJ Cava. Dielectric materials for applications in microwave communicationsbasis of a presentation given at materials discussion no. 3, 26–29 september, 2000, university of cambridge, uk. *Journal of Materials Chemistry*, 11(1):54–62, 2001.

[84] Minki Jeong, Victor Kazmirenko, Yuriy Poplavko, Beomjin Kim, and Sunggi Baik. Electrically tunable phase shifters with air-dielectric sandwich structure. In *MATERIALS RESEARCH SOCIETY SYMPOSIUM PROCEEDINGS*, volume 720, pages 91–96. Cambridge Univ Press, 2002.

[85] Yuriy Poplavko, Victor Kazmirenko, Yuriy Prokopenko, Moongi Jeong, and Sunggi Baik. Low loss phase shifter based on piezo-controlled layered dielectric structure. In *Microwave Symposium Digest, 2003 IEEE MTT-S International*, volume 1, pages 437–440. IEEE, 2003.

[86] EA Nenasheva, ON Trubitsyna, NF Kartenko, and OA Usov. Ceramic materials for use in microwave electronics. *Physics of the Solid State*, 41(5):799–801, 1999.

[87] Constantine A Balanis and John Wiley. *Advanced engineering electromagnetics*, volume 111. Wiley Online Library, 2012.

[88] Roger F Harrington. Time-harmonic electromagnetic fields. *IEEE*, 1961.

[89] Tatsuo Itoh. *Numerical techniques for microwave and millimeter-wave passive structures*. Wiley New York, 1989.

[90] Spartak Gevorgian, Peter LJ Linner, and Erik L Kollberg. Cad models for shielded multilayered cpw. *IEEE Transactions on Microwave Theory Techniques*, 43:772–779, 1995.

[91] M Abdellatif, N Ranjkesh, M Fahimnia, A Taeb, and S Safavi-Naeini. Low insertion loss variable phase shifter for emerging millimter-wave communication systems. *MTT*, 2014.

[92] M. Mohajer, G.Z. Rafi, and S. Safavi-Naeini. A taylor synthesis/optimization method for 2d minimum size transmitting phased array antenna. In *Antennas and Propagation Society International Symposium (APSURSI), 2013 IEEE*, pages 292–293. IEEE, 2013.

[93] Federal Communications Commission et al. Fcc part 25-satellite communications. sec. 25.209 antenna performance standards,revised, 2012.